HIGH THROUGHPUT ASSAYS FOR EXPLORING MATERIALS SPACE FOR ADDITIVE MANUFACTURING

A Dissertation
Presented to
The Academic Faculty

by

Xinyi Gong

In Partial Fulfillment
of the Requirements for the Degree
Doctor of Philosophy in the
School of Materials Science and Engineering

Georgia Institute of Technology
May 2019

HIGH THROUGHPUT ASSAYS FOR EXPLORING MATERIALS SPACE FOR ADDITIVE MANUFACTURING

Approved by:

Dr. Surya R. Kalidindi, Advisor
School of Materials Science and Engineering
Georgia Institute of Technology

Dr. Hamid Garmestani
School of Materials Science and Engineering
Georgia Institute of Technology

Dr. David McDowell
School of Materials Science and Engineering
Georgia Institute of Technology

Dr. Richard W. Neu
George W. Woodruff School of Mechanical Engineering
Georgia Institute of Technology

Dr. Preet M. Singh
School of Materials Science and Engineering
Georgia Institute of Technology

Date Approved: October 3, 2018

ACKNOWLEDGEMENTS

I would like to express my special thanks to my advisor, Surya R. Kalidindi, who provided great support to many tangible and intangible aspects during my PhD study. In particular, he has provided his technique knowledge and invaluable wisdom for being successful. I want to acknowledge the financial support of the National Science Foundation through the award 1435237 ("DMREF/Collaborative Research: Collaboration to Accelerate the Discovery of New Alloys for Additive Manufacturing"). I also wish to thank Soumya Mohan for the personal and academic support through our many conversations. I am greatly indebted to the members of my research group who have provided training, inspiration, entertainment, and their perspectives on all sorts of subject matter. Lastly, I would like to thank my family and friends for their unconditional support through some of the toughest moments in PhD study.

TABLE OF CONTENTS

LIST OF TABLES

LIST OF FIGURES

SUMMARY

Recent advances in additive manufacturing (AM) offer exciting opportunities to build materials with novel internal structures combined with intricate part geometries that cannot be achieved by traditional manufacturing approaches. The large space of potential material chemistries combined with process parameters in AM presents a significant challenge for a systematic exploration of the materials' microstructures along with their final properties. In order to form a "design allowable" property data package, the current experimental assays require major investments of either time and effort on highly customized samples or of cost on large sample volumes.

The goal of this work is to establish practically useful high throughput (HT) experimental assays that match characteristics of AM, deliver abundant and reliable dataset on microstructure and mechanical properties and create meaningful process-structure-property (P-S-P) linkages with relatively small sample volumes. Spherical indentation protocols are extended for HT assays, taking advantage of its flexibility on sample shapes and small sample volumes. Various microstructure characterization techniques including SEM (BSE), EDS and EBSD are introduced to the assays along with quantification methods for microstructure statistics (e.g., phase volume fractions, chord length distributions). AM Titanium alloys are chosen because of their potential to display novel microstructure/mechanical properties that cannot be achieved by conventional case/wrought approaches. In collaboration with external partners, laser engineered net shaping (LENS) and electron beam melting (EBM) were selected to represent two different types of AM (direct energy deposition (DED) and powder bed

fusion (PBF)). Due to LENS's capability of changing powder composition and the post build heating requirement on its final parts, it was employed to explore the effect of chemical composition and post build heat treatment on Ti-Ni and Ti-Mn alloys. A second case study explored the thermal history induced within build variance on Ti64 manufactured by EBM. The results of HT screening and systematic study of material chemistry and process space will be presented and discussed along with a demonstration of extracting practically useful S-P/P-S-P linkages to build materials knowledges for accelerating alloy development.

CHAPTER 1. INTRODUCTION

1.1 Additive Manufacturing (AM) for Metals

Metal additive manufacturing (AM) processes today provide a unique pathway for generating novel components with intricate geometry as well as with novel material internal microstructures that could be customized at different sample locations for desired performance [1]. The process consists of printing successive layers of materials that are formed on top of each other. This technology has been developed by Charles Hull in 1986 in a process known as stereolithography (SLA), which was followed by subsequent developments such as powder bed fusion, fused deposition modelling (FDM), inkjet printing and contour crafting (CC). 3D-printing, which involves various methods, materials and equipment, has evolved over the years and has the ability to transform manufacturing and logistics processes. Additive manufacturing has been widely applied in different industries, including net shaping, component repair, intricate geometry prototyping and component customization (see Figure 1). The uptake of 3D printing in the construction industry, in particular, was very slow and limited despite the advantages e.g. less waste, freedom of design.

The non-equilibrium microstructures obtained in the AM process, especially, provides additional opportunities to design the material itself to meet the specific demands of the application. Indeed, alloy spaces that are not suitable for conventional processing due to, for example, strong solute partitioning in the liquid phase (e.g., generation of β-fleck in Ti-based alloys [2] from depressed freezing temperatures [3]) or the potential precipitation of undesirable phases, may be alternatively explored using

additive manufacturing, as the overall undercooling decreases the freezing range and influences the kinetics of both solute segregation in the liquid phase and unwanted solid-state phase transformations. This gives a chance to design new classes of alloys that are not “casting alloys”, but rather are alloys designed to take advantage of the processing attributes associated with additive manufacturing.

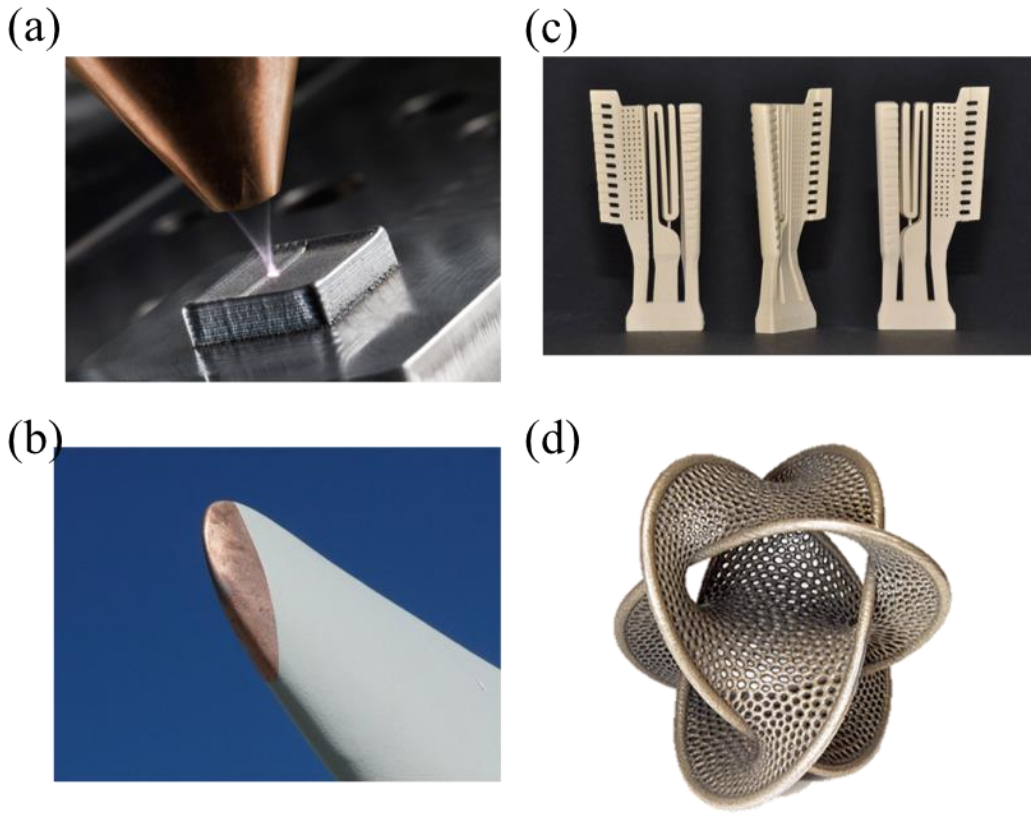

Figure 1 – Illustration of the application of additive manufacturing (AM). (a) – (d) represents AM capability of near net shaping, component repair, intricate geometry prototyping and component customization[1], respectively.

1.2 Materials Space of AM and Challenges

The process of additive manufacturing usually consists of many interconnected controlling parts (see Figure 2), including substrate treatment, powder delivery, energy delivery, nozzle movement and post build treatment. As noted in Figure 2, each of these

[1] Images are reproduced from online sources:
http:// www.fabricatingandmetalworking.com/2016/07/additive-manufacturing-making-sense-laser-metal-deposition-3d-printing/;
https://qph.ec.quoracdn.net/main-qimg-468e59ecd98905385ec32e2994bacd20-c;
https://www.ceramicindustry.com/ext/resources/Issues/2017/May/CI0517-lithoz-slide3-900px.jpg;
https://i.pinimg.com/736x/3a/0f/59/3a0f59a373448fd6f317d40e1b0dc88f--d-prints-cartoon-characters.jpg

parts comprise multiple processing parameters that could potentially significantly influence the thermal history (subsequently the microstructure and final properties) of the component. All together, these parameters create an enormous number of possible process combinations which form an immensely large materials process space. The large space of materials process space combined with non-equilibrium microstructures obtained in AM presents a significant challenge for a systematic exploration and optimization of the final properties exhibited by AM parts when using the existing knowledge databases established for conventionally processed materials.

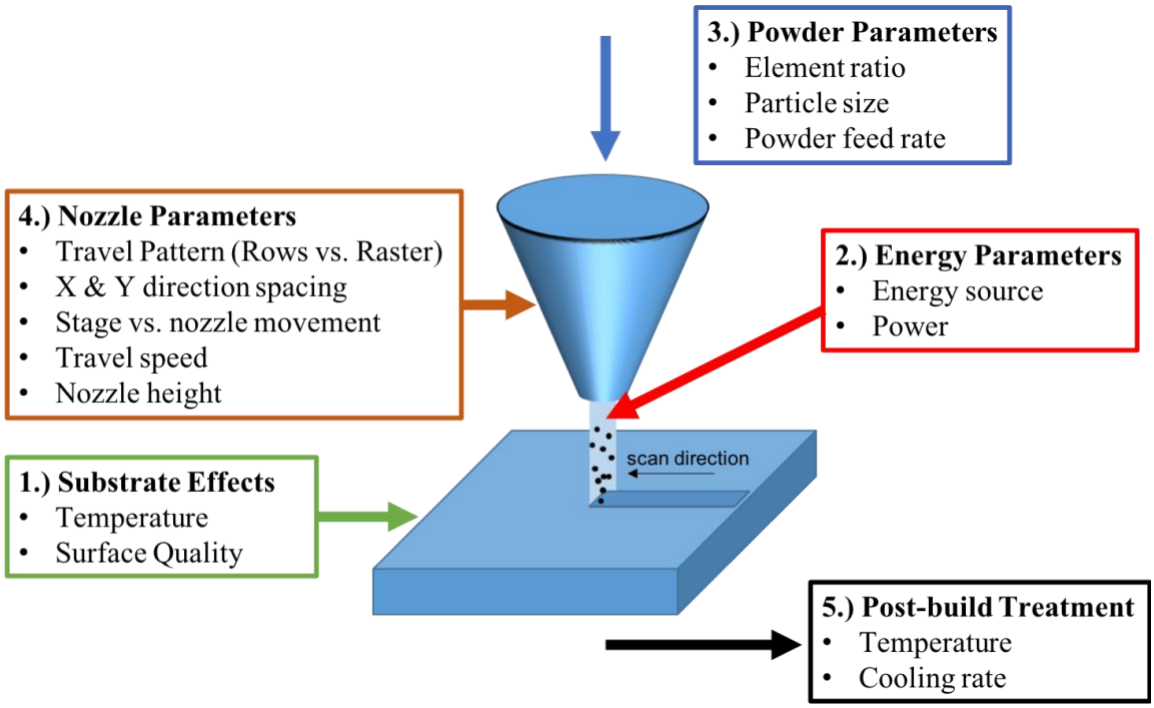

Figure 2 – Schematic of a typical AM process. Box 1) – 5) illustrates possible parameters involved in producing AM components.

CHAPTER 2. BACKGROUND

2.1 Exploring Materials Space for AM

When it comes to the AM of metallic parts, the direct energy deposition (DED) and powder bed fusion (PBF) processes are the most proven and feasible methods. Both processes involve the deposition of powder metal (or less common preforms such as wire) and their simultaneous or subsequent melting via a focused thermal energy source. Unlike plastic or polymeric-based AM processes, PBF and DED require an electron beam or laser beam (or any thermal energy source) to accomplish layer-to-layer metallurgical bonding – to overcome the relatively high enthalpy of fusion and melting temperature of metals.

2.1.1 Composition

Because the rapid cooling feature of AM, it's possible to obtain properties that can't be achieved by conventional methods. However, to date, there have been only a limited number of commercial alloys used in AM. Some of these are presented in **Error! R eference source not found.**. As the AM field matures, it is clear that new alloys, especially alloys with wide range of compositions, will need to be developed in order to exploit the advantages of AM.

Table 1 – Selected alloys commercially used in AM processing [4].

Titanium	Aluminum	Tool steels	Super alloys	Stainless steel	Refractory
Ti-6Al-4V	Al-Si-Mg	H13	IN625	316 & 316L	MoRe
ELI Ti	6061	Cermets	IN718	420	Ta-W
CP Ti			Stellite	347	CoCr
γ-TiAl				PH 17-4	Alumina

2.1.2 Post Build Heat Treatment

In most cases of AM it is desirable to produce parts without internal stress. Currently, AM parts employ a post build heat treatment to reduce internal stress. A close investigation of the mechanical behavior of Ti6Al4V and an evaluation on the influence of heat treatment of PBF Ti64 products is performed previously [5]. Due to changes of microstructures, different cases of treatment were identified (see Figure 3). In most cases the AM parts as built possess internal stresses and have very small grains. In the case that a heat-treatment is used in the reduction of internal stress, a detectable change regarding to the mechanical behavior e.g. the increase of elongation at break was observed. The purpose of changing the microstructure is to enlarge the grain size or the laminar structure (e.g. Ti64) and to change the constellation of microstructure, e.g. from a α'-constellation to a αβ-constellation of Ti6Al4V.

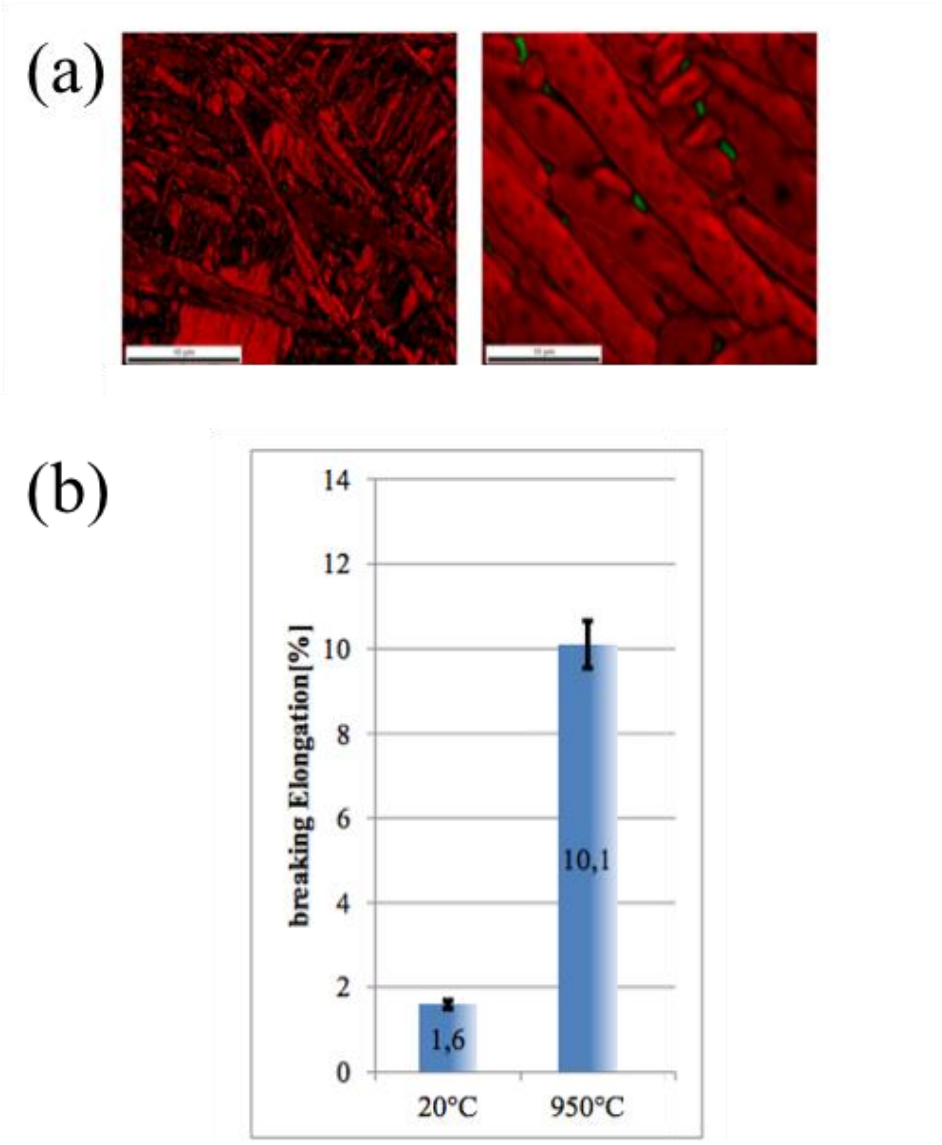

Figure 3 – (a) Comparison of EBSD scans (30µm x 30µm) between non-heated (left) and after the 950°C heat treated specimens (right). (b) Comparison of breaking elongation between non-heated (left) and after the 950°C heat treated specimens (right) [5].

However, few cases have been studied under DED which has higher residual stress and almost always requires a post build heat treatment. Thus, models that link post

build heat treatment, subsequent microstructures and corresponding mechanical properties need to be systematically studied.

2.1.3 Thermal History

For the process of AM, even if one manages to maintain the controllable processing parameters to be stable, distinct microstructure regions with fairly different mechanical properties have been reported for various AM alloys, including DLD AISI P20 tool steel [6], AISI H13 tool steel [7-9], AISI 420 tool steel [7], AISI 4140 steel [10], AISI 410 stainless steel (SS) [11], AISI 316L stainless steel [12], Inconel 625 [13], and Ti-6Al-4V [14] components..

As seen in Figure 4, it has been reported that for steels, the micro-hardness values of subsequent deposited layers decreases from the first deposited layer and then increases toward top layers [10, 12, 14]. This inhomogeneity can be attributed to the time-variable cooling rate of the melt pool and a relatively slower velocity of solidification in the middle region. The middle region is also exposed to cyclic reheating (related to subsequent layer deposition) and experiences a substantial heat affected zone (HAZ) for a longer period of time. As a result, higher micro-hardness has generally been measured at the top and bot- tom of DLD parts which undergo higher cooling rates during the DLD process as compared to the middle region. For instance, in laser-deposited Ti-6Al-4V parts, the sizes of the laths (e.g. a thin and narrow strip of crystalline structure) vary with location [15, 16]. The microstructure in both the top and bottom of the deposited Ti-6Al-4V part consists of the Widmanstätten structure; however, the morphology is different in

each region. The top region primarily displays colonies of parallel, very fine lamellae, and larger laths, as presented in Figure 4(a), whereas the bottom region has thicker lamellae, as shown in Figure 4(b) [16]. These differences in Ti-6Al-4V microstructure can be attributed to the temperature gradients, cooling rates and repeated heat treatments during subsequent laser-deposition steps.

Such variance within build needs to be studied in EBM system (which often needs no post heat treatment). Also, an efficient way of studying the linkage between microstructure and mechanical property needs to be built for this feature.

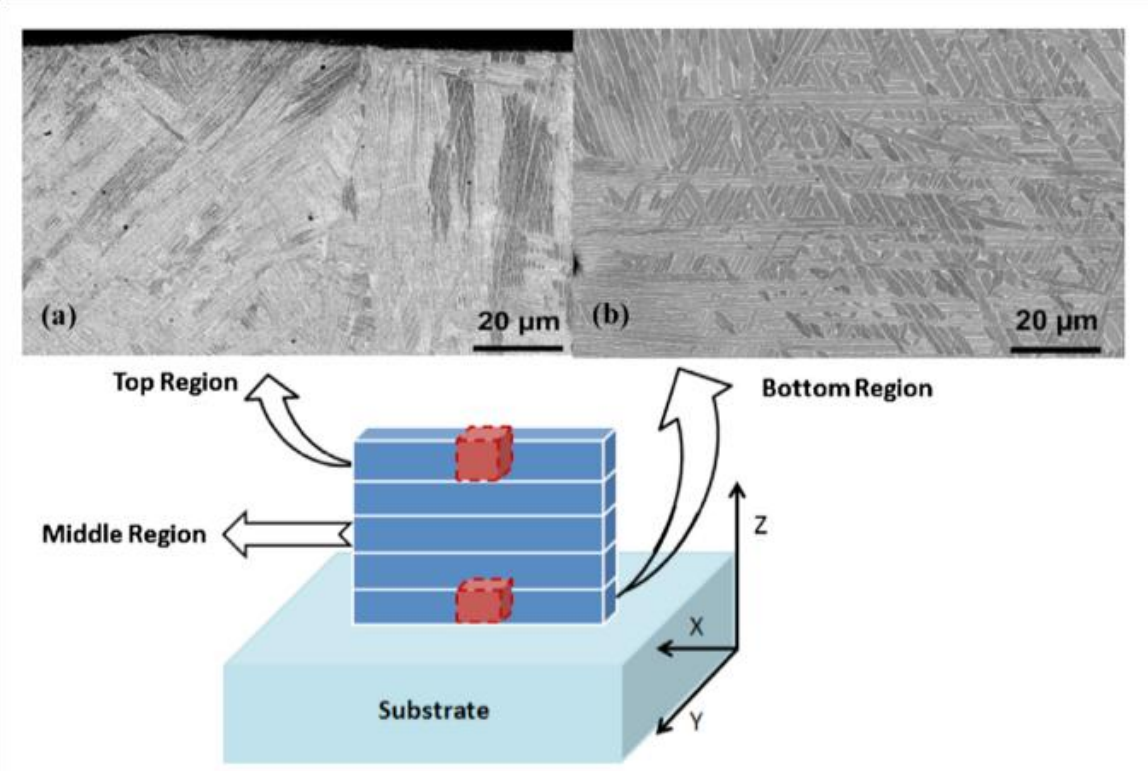

Figure 4 - Microstructure of a direct laser-deposited Ti-6Al-4V part in Y–Z plane at (a) the top region and (b) the bottom region [17].

2.2 Current Assays

When new alloys are designed, it is necessary to develop a high degree of confidence in the performance of the alloy during service. Traditionally, at the most basic level, this is accomplished by developing "design allowables" where the statistical distributions of properties are well understood. Invariably, static properties such as those obtained from tensile coupons (e.g., yield strength, elastic modulus, ultimate strength, % elongation, % reduction in area) form the basics of a "design allowable" data package. However, the space of potential material chemistries combined with non-equilibrium

microstructures is enormously large [18]. To obtain the desired data covering the large materials space of interest in AM, it will be necessary to produce and test a large number (i.e., in the hundreds) of standardized bulk tension coupons extracted from material characterized by a good control of processing history and chemistry in the entire sample volume. It thus poses a significant challenge to find the right processing recipes and parameters that fully exploit the unusual characteristics of AM and seems to hinder the potential to design new alloys. Saltzbrenner et al. [19] have recently developed and demonstrated high-throughput prototyping and tensile testing protocols that are capable of addressing some of the issues described above, including reliable assessment of the variance in the measured properties. These methods continue to employ tensile test specimen, which may not be practical for many AM processes.

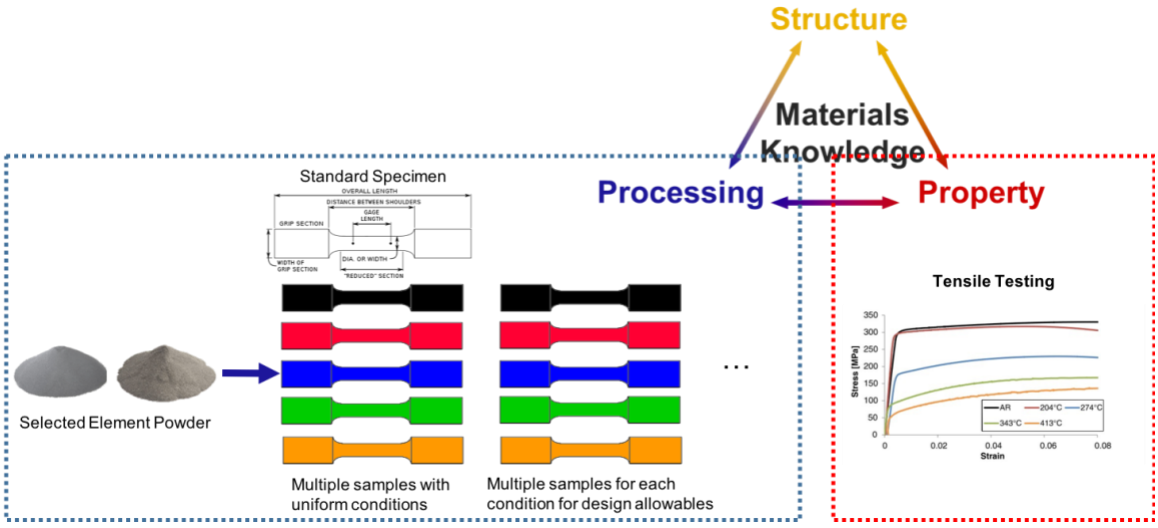

Figure 5 – Schematic of materials knowledge and conventional assays needed for building P-S-P linkages.

One has to note that in order to produce meaningful datasets, the requirement for manufacturing such specimens is fairly high. 1) The variance between different dumb bells under the same condition needs to be small enough so that the following results can represent the designed composition (or other process parameters). It poses significant challenges on the controllability and reproducibility for additive manufacturing which requires huge investment in machinery and research efforts. 2) The variance within each dumb bell (at least within the region of stress field) needs to be small enough so that the results from this specimen can represent the designed composition (or other process parameters). As you will see in Chapter 6, the inherent thermal history variance during specimen creation in additive manufacturing is a major road block for manufacturing parts of near homogenous conditions. In fact, study has shown that surface quality of the specimen is crucial in determining the mechanical properties in similar testing gauges. Thus, it is reasonable to seek a new strategy for experimental assays that fits AM.

CHAPTER 3. DEVELOPMENT OF HIGH THROUGHPUT EXPERIMENTAL ASSAYS FOR EXPLORING AM MATERIALS

With the credible potential of AM and challenges mentioned in previous chapters, it is clear that designing a set of protocols which performs high throughput experimental assays is much needed. One promising strategy to tackle the large space of potential material chemistries and process parameters is to develop and employ high throughput assays that only require very small material quantities. This is ideally suited for AM processes that can vary material chemistries and process conditions from location to location in the same sample. In essence, this strategy allows one to build a large library of material chemistries using different processing histories, and then performing structure and mechanical characterization at small scales to assemble the desired knowledge databases needed for design of AM parts. Indeed, one can plan and design cost-effective studies that are exclusively aimed at establishing the salient process-structure-property linkages of interest in material systems explored by AM.

A significant current impediment in the implementation of the vision described above comes from the lack of a reliable methodology and protocols for the mechanical characterization of samples in very small volumes. In this regard, recent advances in spherical indentation stress-strain protocols [20-27] offer many advantages. The conventional practices in indentation testing rely on sharp indenters and analyze the unloading segments after imposing substantial amounts of indentation loads (or depths) to arrive at estimates of modulus and hardness [28-30]. One of the consequences of adopting these traditional indentation protocols is that they significantly alter the material

in the indentation zone (due to the imposed plastic deformation) before extracting the mechanical properties of interest. In contrast, the recently developed spherical indentation stress-strain protocols analyze the very short initial loading segments and recover a meaningful indentation stress-strain curve that reflects the intrinsic elastic-plastic properties of the virgin material in the indentation zone. Since the size of the indentation zone can be systematically varied in the modern instrumented indenters with the use of different indenter radii, this new capability promises to offer a high throughput strategy for multiscale mechanical characterization of AM processed materials. An important inherent advantage of employing indentation techniques is that it allows one to conduct a multitude of tests on a single sample and extract statistically meaningful information on the variability in the location-specific properties exhibited by the produced part in a cost-effective manner.

This work describes our efforts and initial successes in developing high throughput assays for AM processed materials that incorporates sample prototyping with characterization of relevant microstructure and properties. Specifically, the additive manufacturing techniques known as Laser Engineered Net Shaping (LENS™) and Electron Beam Melting (EBM) will be employed in this study. Ti-Ni, Ti-Mn and Ti64 alloys, were selected. The objective of this work is to create HT experimental assays that provide both microstructure and mechanical properties information and build linkages.

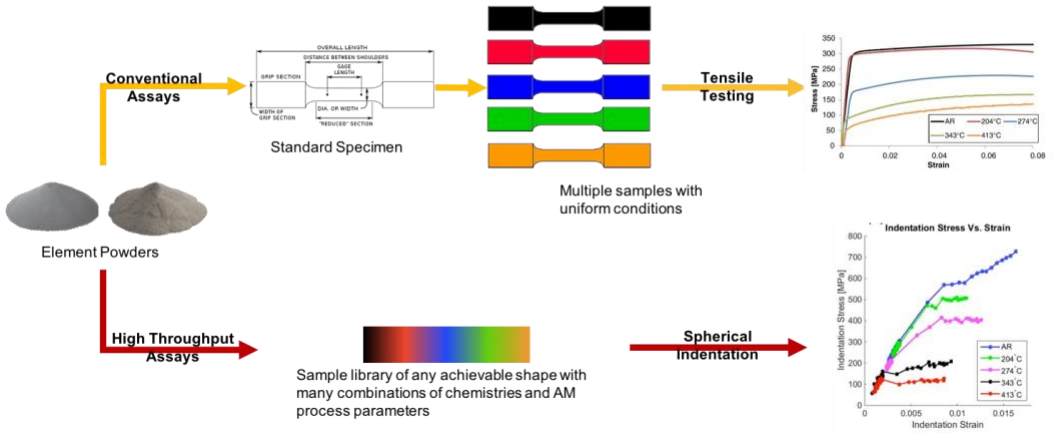

Figure 6 - Schematic of the conventional approach (top row), and how this can be augmented with a high throughput (HT) approach (bottom row) to explore materials with different combinations of compositional and/or process conditions. Both tensile and indentation stress-strain curves are from previous work [21].

CHAPTER 4. APPROACHES

4.1 Mechanical Characterization for Small Volumes

As noted earlier, we envision using the recently developed spherical indentation stress-strain protocols for evaluating local mechanical properties. In doing so, we will pay careful attention to quantifying the effects of the macroscale gradients in material chemistry introduced in the samples as well as the inherent microscale heterogeneity in the AM processed samples. While the macroscale chemistry gradients were purposefully introduced in the samples, the microscale heterogeneity is unavoidable and likely to be more severe in the AM processed samples compared to the conventionally processed samples. The indentation methods, because of their very small probe volumes and high throughput nature, are capable of quantifying the variances in the measured mechanical properties at both these scales. The potential benefits of these indentation techniques in extracting reliable process-structure-property linkages have been demonstrated in a few recent studies [21, 31]. Other currently available approaches suitable for mechanical characterization in small material volumes include microscale tension/bending tests [32, 33] and micropillar deformation tests (produced by focused ion beam (FIB) milling) [34, 35]. Both techniques require time-consuming and expensive sample preparation [36], and thus are not amenable to HT approaches aimed at exploring large design spaces in materials development. Instrumented spherical indentation is indeed the only practical technique of choice for our purpose. In this regard, it should be noted that the recently developed spherical indentation protocols [22, 25] are capable of extracting indentation stress-strain (ISS) curves from very small volumes (indentation zone radii ranging from

~50 nm to ~500 μm). Significant progress is being made in correlating the properties measured in indentation with the properties measured in conventional testing such as simple compression [20, 21, 37, 38], which will aid tremendously in increasing the interpretability of the indentation results.

The protocols used in the study to produce the indentation stress-strain curves [20, 22, 23] are briefly summarized next (see Figure 7). They are based on the Hertz's theory [39, 40] for frictionless and elastic contact between two homogenous, isotropic, bodies with parabolic surfaces, expressed as

$$P = \frac{4}{3} E_{eff} {R_{eff}}^{1/2} {h_e}^{3/2} \tag{1}$$

$$a = \sqrt{R_{eff} h_e} = \frac{S}{2E_{eff}} \tag{2}$$

$$\frac{1}{E_{eff}} = \frac{1 - v_i^2}{E_i} + \frac{1 - v_s^2}{E_s} \tag{3}$$

$$\frac{1}{R_{eff}} = \frac{1}{R_i} + \frac{1}{R_s} \tag{4}$$

where the indentation load and the elastic indentation displacement are denoted by P and h_e, respectively. The effective modulus and the radius of the indenter-sample system are denoted as E_{eff} and R_{eff}, respectively. The subscripts i and s correspond to the indenter and the sample, and E and ν denote the Young's modulus and Poisson's ratio, respectively. S (=dP/dh_e) denotes the elastic stiffness (i.e., the slope of the

unloading curve, also known as harmonic stiffness in continuous stiffness measurement (CSM) protocols [28, 41]).

Indentation stress, σ_{ind}, and indentation strain, ε_{ind}, need to be defined to be consistent with Hertz's theory, while exhibiting a linear relationship in the elastic indentation regime. They should also allow generalization for the elastic-plastic indentation and produce meaningful indentation stress-strain curves with an initial elastic regime followed by transition into an elastic-plastic regime. In recent work [20, 21, 24, 38], it was demonstrated that the following definitions meet these criteria

$$\sigma_{ind} = \frac{P}{\pi a^2} \tag{5}$$

$$\varepsilon_{ind} = \frac{4}{3\pi}\frac{h_s}{a} \tag{6}$$

$$h_s = h - h_i \tag{7}$$

$$h_i = \frac{3(1-\nu_i^2)P}{4E_i a} \tag{8}$$

where h_s is the corrected sample displacement (subtracting displacement in the indenter, h_i, from the total displacement, h). The slope of the indentation stress-strain curve in the elastic regime obtained with these protocols is referred as the indentation modulus, E_{ind}. Consistent with Hertz's theory, for isotropic samples, one obtains

$$E_{ind} = \frac{E_s}{1-\nu_s^2} \tag{9}$$

The indentation yield strength, Y_{ind}, is defined using a 0.2% offset plastic strain on the indentation stress-strain curve. The indentation work hardening rate, H_{ind}, is computed from the indentation stress-strain curve between 0.5% and 2% offset plastic strains using a linear regression fit [21, 25]. These properties can then be fed into the pipeline to create the structure property linkages.

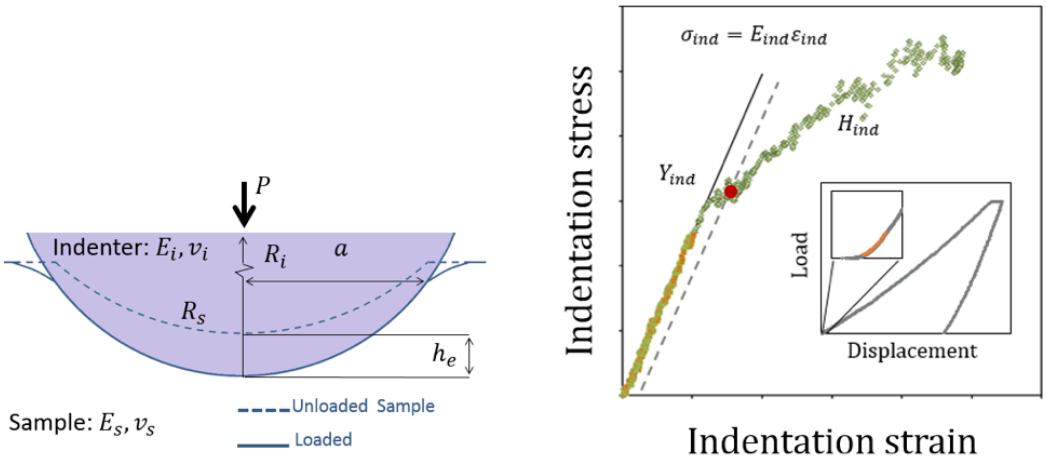

Figure 7 - (a) Schematic of spherical indentation, and (b) an example indentation stress-strain curve.

Recent works [42] show that spherical indentation protocols prove to be not only robust at capturing the local elastic-plastic response of polycrystalline metal samples at length scales much smaller than the grain size, but also reliable at length scales that include multiple grains to recover stress-strain curves. These new protocols are also applied to compare commercially pure titanium and titanium alloys such as Ti-6Al-4V [27].

Only recently, these protocols have been extended to microindentation, where the length scales correspond to several grains (about 10 - 1000) in the indentation zone [31,

43]. A significant challenge in extracting meaningful indentation stress-strain curves from the indentation experiments comes from the need to estimate reliably the evolving contact radius throughout the entire loading history. In modern nanoindenters (where the indentation zone sizes are typically much smaller than the grain size), this is accomplished through the CSM (continuous stiffness measurement) capability [109]. However, this capability does not yet exist for microindentation experiments. Consequently, the only way to estimate the contact radius reliably is to employ a multitude of unloading segments and analyze them using Hertz theory [57]. Therefore, custom protocols were designed and implemented to allow a multitude of loading-unloading (cor- responding to about 30 - 50% often peak force) cycles. Since each unloading segment produces one data point on the indentation stress-strain curve, the number and frequency of the unloading segments has to be suitably adjusted to produce a meaningful and practically useful indentation stress- strain curve.

The protocols for extracting indentation stress-strain curves from the raw load-displacement data from spherical indentation are based largely on Hertz theory (Eqs. (1) - (4)). For the initial elastic loading of a flat sample surface, the effective radius, R_{eff}, is equal to the indenter radius, R_i. Therefore, it would be possible to extract R_{eff} from the measured load-displacement using standard regression techniques; E_s can be recovered using Eq. (3). The main hurdle in this protocol comes from having to make "zero-point" corrections to both measured load and measured displacement signals. However, with larger indenter tips, the measurements are less sensitive to the surface quality of both sample and indenter. Consequently, for the microindentation testing, there was no need for a zero-point load correction. After the material in the indentation zone experiences

plastic deformation, Eq. (1) needs to be modified to introduce the permanent displacement or residual height, h_r:

$$h = \left[\frac{3}{4}\frac{1}{E_{eff}}\frac{1}{\sqrt{R_{eff}}}\right]p^{\frac{2}{3}} + h_r \tag{10}$$

Note that Eq. (10) can only be applied to unloading segments (these are assumed to be elastic). Applying standard regression techniques on the unloading segments to fit Eq. (10) produces reliable estimates of h_r and R_{eff}. In this analysis protocols, it is assumed that E_{eff} obtained from the initial elastic loading segment remains unchanged. This is a reasonable approximation for most materials, given the very small strains introduced in the indentation studies presented in this work. An unloading segment between 95% and 50% of the peak load (in each unloading) was employed in this work to estimate the evolving values of h_r and R_{eff}. After the initiation of plastic deformation in the sample, R_{eff} is no longer equal to R_i. Indentation stress, σ_{ind}, and indentation strain, ε_{ind}, corresponding to the start of each unloading segment are computed as

$$\sigma_{ind} = \frac{P_{max}}{\pi a^2} \tag{11}$$

$$\varepsilon_{ind} = \frac{4}{3\pi}\frac{h_{s,max}}{a} \tag{12}$$

$$a = \sqrt{R_{eff}\left(h_{s,max} - h_r\right)} \tag{13}$$

where P_{max} and $h_{s,max}$are load and displacement at the peak of each unload, and a is the contact radius. $h_{s,max}$ is used to compensate the elastic displacement of the indenter, h_i, and is computed as Eqs (7) – (8).

4.2 Microstructure Quantification and Dimensionality Reduction

To extract useful insights, one needs to correlate the measured indentation properties with salient descriptors of the microstructures in the indentation zone. If the indentation length scales are well below the typical grain size, relevant microstructure attributes would include the grain orientation and local dislocation density in the indented zone [21, 24, 44, 45]. If the indentation zone covers several grains, the relevant microstructure features might include grain size, shape, and orientation distributions in the indented zones [21]. In the present study on multiphase microstructures, we will focus mainly on the phase volume fraction, an averaged spacing between the intermetallic phase, chord length distribution with certain phases or grains and two-point spatial statistics of grain/phase boundaries in the microstructure as the main microstructure descriptors. This is because we anticipate these features to exhibit strong correlations with the properties measured in indentation. In order to obtain these microstructure measures, we will employ backscattered electron (BSE) microscopy (in the scanning electron microscope), energy dispersive spectroscopy (EDS) and electron backscattered diffraction (EBSD) to capture phase morphology, element/phase distribution and grain/phase morphology information. The tests will be carried out at locations of different conditions (i.e. chemical compositions, post-build heat treatment and build heights).

Once we have captured our structure images, we need a statistical representation which can be used to correlate the properties with structure. Although it is possible to select a number of different measures for the quantification of the microstructure in this work, besides volume fraction, the logical choice of low computationally intensive method here would be chord length distributions (CLDs). This is because the main microstructure feature of interest is the phase size and shape distributions and their anisotropy. Also, chord lengths connect directly to plastic properties of interest through established models such as the Hall-Petch models [46]. Furthermore, the computational cost of computing the CLDs is substantially low (order of the number of voxels in the microstructure); this is a significant criterion for this work as we intend to form a high throughput workflow. A chord is defined as a line segment within the microstructure contained within a single phase whose endpoints lie at phase boundaries. Relatedly, chord length is defined as the length of any such chord. CLD quantifies the probability of finding a chord of a specified length within a microstructure. CLDs can be resolved directionally [47] by treating chords exclusively in only one direction. Figure 8(a) illustrates the sampling of representative chords in X and Y directions in a pixelized microstructure, where the length of each chord is indicated by its color (shorter chords are blue and longer chords are yellow). In this plot (as well as the case study presented later), the microstructures are digitized, and the length of a chord is simply taken as the number of pixels composing each chord. Figure 8(b) shows corresponding CLDs resolved along X and Y directions of the micrograph. The broader CLD in the Y direction indicates that the grains are elongated in the Y direction compared to the X (see

also Figure 8(a)). An averaged chord length will be defined as the sum of all chords weighted by their probability of occurrence.

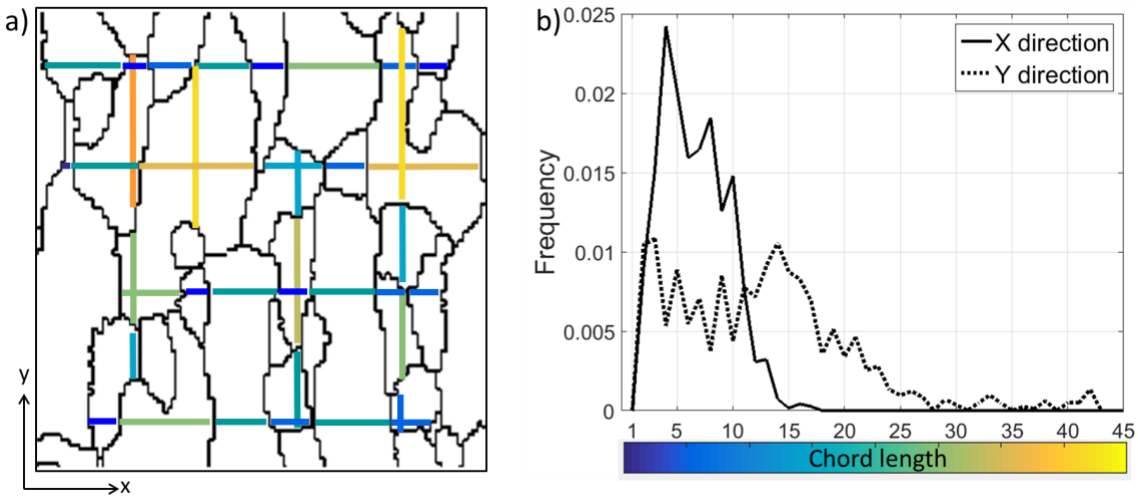

Figure 8 - Illustration of chord length distributions: a) micrograph with example chords drawn in X and Y directions; b) chord-length distributions in X and Y directions for the micrograph in (a).

A statistical representation that contains various information on volume fractions, sizing and spacing and other microstructure measures and that allows for a framework for comparison of microstructures is also very important. For this purpose, two-point statistics was chosen. Two-point statistics are calculated as the likelihood that the head and tail of each vector that can be placed in the microstructure are on the assigned phases [41]. For example, a simple checkerboard microstructure in Figure 9 demonstrates this concept. Part A shows the original image and part B the autocorrelation of black state. The arrows represent the (1,1) vector in the two-point statistics. This point is determined

by taking all possible vectors in the microstructure (6 shown here) and determining how many of them have both head and tail on black. The vectors as shown with the orange arrows have both head and tail on black counting as trials of success, while the red arrows count as trials of failure. These statistics retain all of the information contained in the segmented microstructure which can be shown by the fact that the original microstructure can be recovered from them. Two-point statistics also have the advantage of having a natural origin which allows the comparison of microstructures. In the two-point statistics the origin is created from the (0,0) vector placed on the microstructure. This point in the autocorrelation corresponds to the volume fraction because it is the likelihood that a spot will be of the chosen phase. This and every other point in the two-point statistics is created by the same set of vectors no matter the microstructure. Therefore, each pixel can be compared with its corresponding pixel in another 2-point statistics map. Similar microstructures will have similar two-point statistics even if a pixel-by-pixel comparison of the two microstructures would make them appear to be dissimilar.

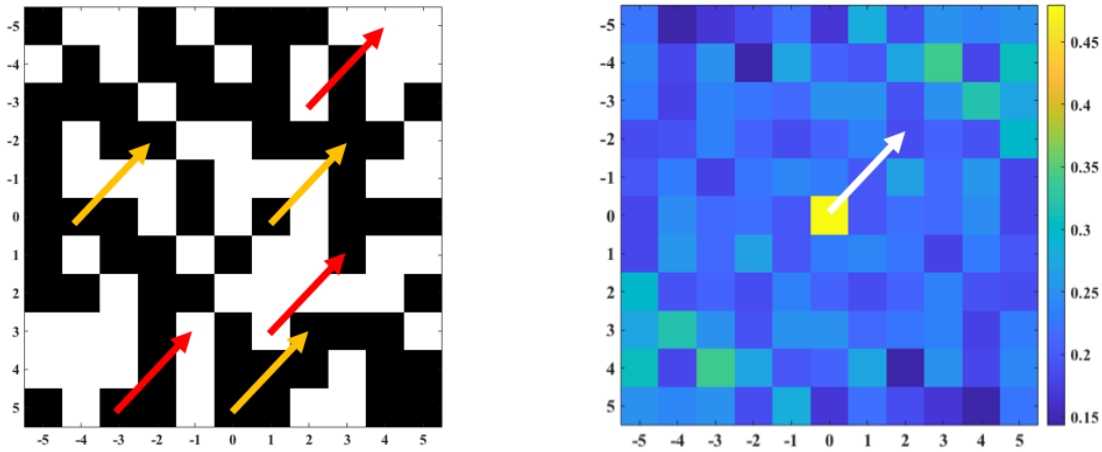

Figure 9 - Checkerboard microstructure and corresponding two-point statistics of black state auto correlation. Arrows show the (2,2) vector in the two point statistics and a few of the corresponding vectors in the microstructure. Orange arrows represent successful trials while red arrows represent fail trials.

However, the two-point statistics are still of the dimensionality of the original structures which for a single sample can be millions of voxels. In order to reduce the dimensions to a reasonable number for use in correlations with the properties, we have chosen to use principle component analysis (PCA). Principal component analyses (PCA) has been shown to be remarkably effective in arriving at objective (data-driven) low dimensional representations [48-55] of the microstructure. Mathematically, this can be expressed as

$$f_r^{(k)} = \sum_{i=1}^{P-1} a_i^{(k)} \varphi_{ir} + \tilde{f}_r \tag{24}$$

Where $f_r^{(k)}$ denotes a contracted representation (i.e., as a single vector) of all the spatial correlations of a microstructure indexed by k, $\tilde{f}_r$ denotes the ensemble average of

all microstructures included in the analyses, φ_{ir} denote the directions of the new linearly transformed reference frame (identified by PCA) and $a_i^{(k)}$ are the coordinates (also called PC scores) in the new reference frame. A salient feature of PCA is that it transforms the data into a new orthogonal frame where the axes are ordered by the maximum variance seen in the data.

PCA recasts the data onto axis which correspond to the largest amount of variation in the data. Figure 10 gives an illustration of this process in a two-dimensional frame. The first principle component, here labeled as p1, is chosen as the direction of the most variability in the data. The second principle component (p2) is determined as the direction orthogonal to the first principle component which encompasses the next highest amount of variation. This can continue until you have as many principle components as you have original dimensions as pictured in the middle image. However, we can quantify the amount of variation captured in each PC. The number of PC that are used for the regression can then be determined by the desired minimum amount of variation that needs to be included. The third section of this figure shows our two-dimensional data reduced to a single dimension. By this means we can reduce our many dimensional data to a workable number of dimensions and a measure of how much of the original information is retained.

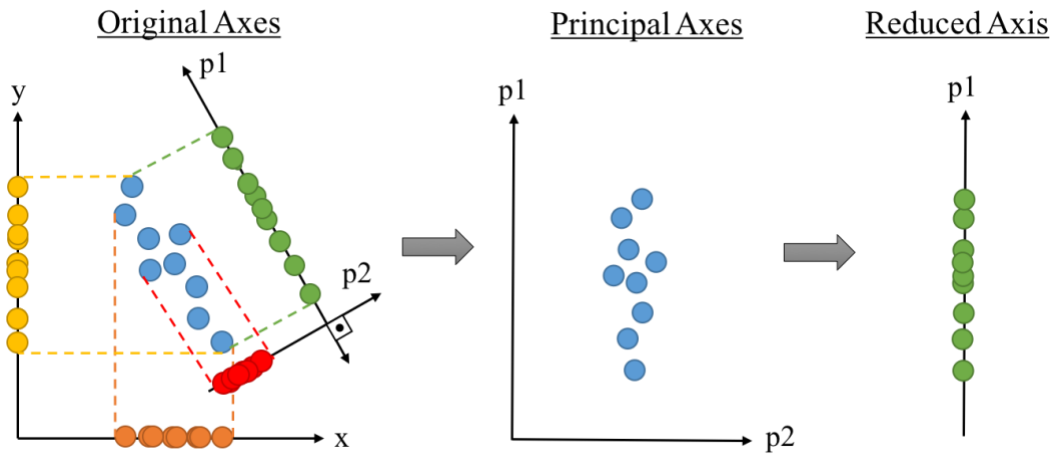

Figure 10 - Illustration of principle component analysis. The original data found on the first portion of the image can be converted to the principle component axes as seen in the middle portion of the image. The dimensions of the data are reduced to a single axis with a quantifiable amount of variance lost as seen in the third section of this image.

CHAPTER 5. EXPLORATION OF TITANIUM ALLOYS FOR LASER ENGINEERED NET SHAPING

Laser Engineered Net Shaping (known as LENS) is a typical direct energy deposition technique in additive manufacturing. It often incorporates computer-controlled lasers as power sources that, in hours, weld air-blown streams of metallic powders into custom parts and manufacturing molds. A schematic (Figure 11) shows the basic elements in LENS. This technique produces shapes close enough to the final product to eliminate the need for rough machining which promotes its popularity in the industry. Due to its great liability and low porosity of the final products, LENS is vastly employed in customization and repair of intricate mechanical parts including turbine blades. The capability of powder flow control also makes LENS possible for creating chemically graded components. Its reliability and flexibility make LENS a perfect candidate for generating combinatory sample libraries which bear designed variances in materials chemistry and thermal history within relatively small volumes. At the same time, its popularity may hopefully increase the potentially impact of such studies.

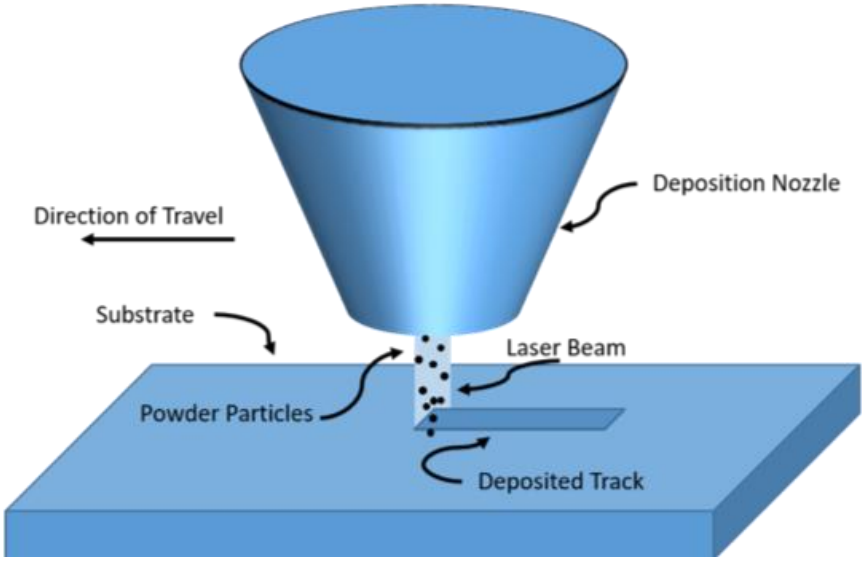

Figure 11 – Schematic of laser engineered net shaping (LENS) [56]. It comprises a deposition nozzle head which delivers powder particles onto certain substrates, a laser operating system which subsequently melts the powder particles and a spatial control system which moves the head for deposition in certain tracks and layers.

The promotion of additive manufacturing is extremely challenging at current stage because of cost sensitivity. Potential parts have been identified, for example multi-channel turbine blades, intricate valves, springs and connecting rods. But for an application in a family like automobile, the problem of producing low-cost parts has to be solved. It is thus only logical to first develop the materials and fields/products that have low sensitivity to cost. From this perspective, titanium alloys are chosen for this study because it has been widely studied and adopted in airframes, aero engines and highly customized bio-compatible appliances – both less sensitive to costs (practical for actual applications) and in need of intricate/customized geometries (suitable for additive manufacturing).

Two case studies following in this chapter will be investigating on the influence of material chemistry and post build aging temperature on titanium-nickel alloys and titanium-manganese alloys respectively. Protocols of high throughput characterization methods will be formulated and employed, followed by rapid screening of material chemistry space and process space. The results of microstructure quantification and mechanical response acquisition will be presented, analyzed and discussed. Finally statistical process-structure-property linkages were extracted through linear regression and Gaussian Process (GP) regression demonstrating the practicality of this high throughput experimental assays.

5.1 Compositional Gradient on Titanium-Nickel Alloys

The first case study in this chapter will be focusing on the compositional effects on Ti-Ni alloys. The change of composition is recognized as one of the most obvious and influential factors that could results in significant shift in microstructure and subsequent mechanical properties. Ti-Ni alloys, whose Ni composition ranges between 0-11%wt (Figure 12), were deliberately selected. And the sample stripe was carefully manufactured with gradient over the vertical direction (Figure 13).

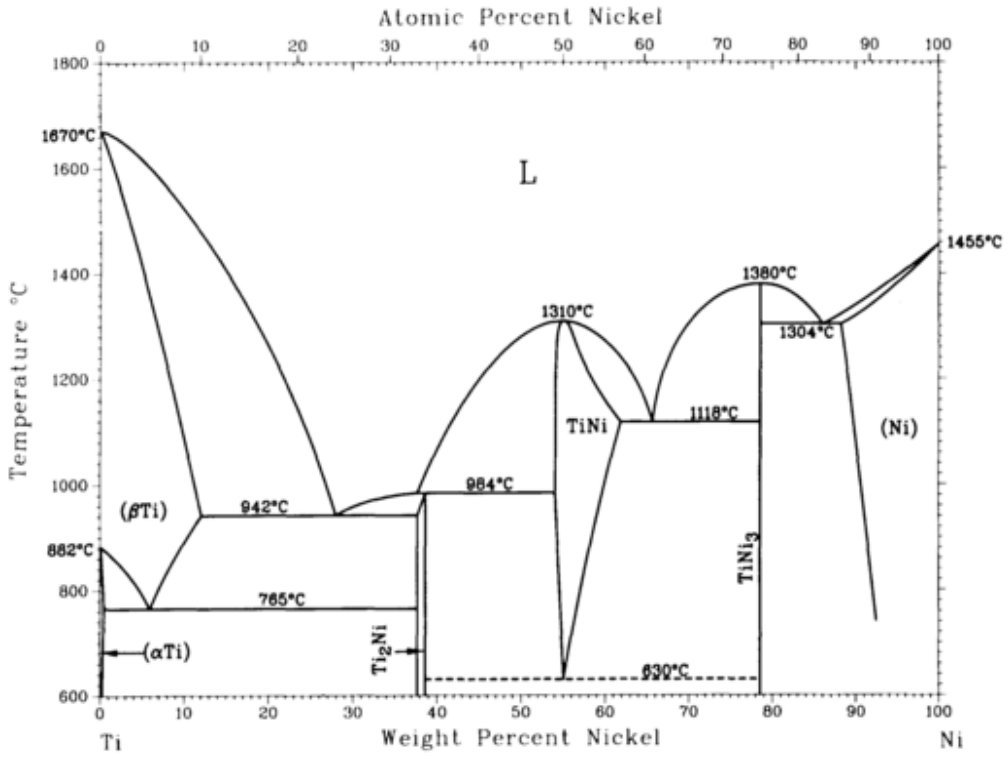

Figure 12 - The Ni-Ti phase diagram (adapted from Massalski *et al.*, 1990 [57]). The region of interest in this study lies at the temperature of 550 °C and the nickel composition range of 0 – 12 wt%

This system was selected because it is a model eutectoid β-stabilized system, which is traditionally susceptible to problems such as β-fleck and hence is not considered for conventional cast/wrought titanium alloys. Due to the β-fleck, the composition regime is traditionally limited, as most industrially relevant titanium alloys are relatively solute lean in elements that promote β-fleck, such as Fe and Ni. However, if the β-fleck can be avoided, which is the case under AM process conditions, this system may exhibit enhanced strength properties due to the mismatch in the shear moduli and atomic radii of

the two elements (these will influence the ease with which dislocations move and the potency for precipitates which will act as barriers for dislocations).

5.1.1 Materials and Process

This section will introduce the materials and the specifics on the process of sample stripes. Because the specimen is manufactured by our collaborators from Professor Collins group in ISU, most of the details in this section is provided by Professor Collins [58].

Owing to the very small molten pool relative to the specimen size, it is possible to independently control and feed multiple material sources with heat sources in additive manufactured specimens. Taking advantage of this idea in conjunction with the LENS™ technique, we executed high throughput (HT) processing to produce samples for this study. Previously, this technique has been used to study composition-microstructure relationships and composition-property correlations for hydrogen storage, oxidation resistance and magnetic properties [59-63]. Use of elemental powder blends [64, 65] avoids pre-alloyed powders. It substantially benefits this type of AM in that a library of materials with a tunable range of chemistries and process parameters can be produced within a small volume sample with relatively low cost, which potentially promotes a high throughput approach. It should be noted that the LENS™ generated materials can exhibit strong variations from one sample location to another in the distributions of grain orientations, phases, composition and residual stress states, which can have a pronounced effect on the mechanical properties specific to the location in the sample [66]. Indeed,

one can turn this into an advantage, especially in the context of high throughput assays discussed in this work, by treating the material volumes at different locations associated with distinctly different combinations of local chemistry and local (thermo-mechanical) processing history as distinct samples.

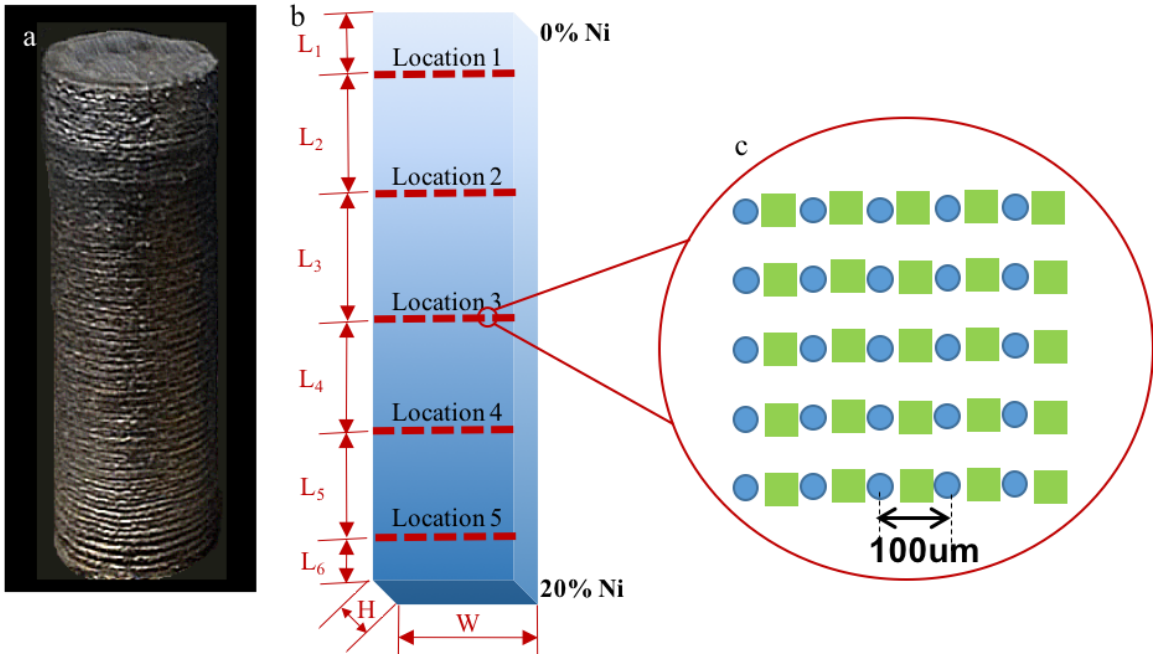

Figure 13 - (a) Layered Ti-Ni sample produced by the LENS process for this study. (b) Schematic showing the indentation locations on the sectioned sample, the dimensions are listed in millimeter: Width, W = 5 mm, Height, H = 3 mm, Length, L_1 = 3 mm, L_2 = 9.5 mm, L_3 = 8.5 mm, L_4 = 7.3 mm, L_5 = 7.2 mm, L_6 = 2.5 mm. (c) Grids of back-scattered electron images (green boxes) and indentation tests (blue dots) at each of the five locations.

An Optomec LENS™ 750 system (see Figure 11), equipped with two powder feeders, was used to deposit compositionally graded Ti-Ni specimens for the present study. This system incorporates an Nd:YAG laser operating at a wavelength of 1064 nm.

The power of the laser was ~350W. Cylindrical specimens were made with a diameter of ~10 mm, and a height of ~38 mm (see Figure 13(a)). The motion control file was modified to change the powder flow rates at certain layers to pre-determined powder flow rate set points. This made the control of sample composition gradient possible. For this work, the material fed into the LENS™ system were blends of 99.9% pure titanium powder (> 150 μm) from Alfa Aesar and 99.9% pure nickel powder (-170/+325 mesh) from Atlantic Equipment Engineers. During the deposition, the layer height was ~0.25mm, the layer spacing was ~0.38mm and the composition range was from pure Ti to Ti-12 wt%Ni**.** In titanium alloys, LENS™ deposition results in initial microstructures that are often martensitic in nature, and should therefore be considered non-equilibrium microstructures. However, these martensitic phases do decompose upon the deposition of the subsequent layers. Further, most industrial applications require subsequent heat-treatments to the deposition [67], resulting in close-to-equilibrium microstructures. Therefore, following deposition, the as-deposited Ti-Ni cylinder was subjected to a heat treatment by sectioning into pieces, wrapping the pieces in titanium foil, and encapsulating in a quartz tube with a titanium sponge to act as an oxygen getter. These samples were β-solutionized below the eutectic temperature (< 942°C) for 4 hours to ensure local chemical homogeneity and reduction/elimination of any residual stress created during deposition so that residual stress is not a variable in this study. The sample was then step-quenched down to aging temperature (T_{age} = 550°C) and held at that temperature for four hours. The heat treatment was chosen to lie in a two-phase field defined by alpha and Ti_2Ni. Since the objective of the study was for a "rapid" assessment, this heat-treatment was based upon a time-temperature pairing for other

titanium alloys which have been shown to produce close-to-equilibrium microstructures. While a variety of other time/temperatures were also selected initially in our study (e.g., 650°C for 2 hours), the 550°C sample exhibited a microstructure with the desired feature sizes. A representative microstructure of the aged sample is shown in Fig. 4, which shows nominally equiaxed grains. These equiaxed grains are an atypical observation, given that the typical grain structure in many additively manufactured samples are columnar, arising from an 'epitaxial' growth of grains [24]. In alloys such as Ti-6Al-4V, which has a very narrow freezing range, such epitaxial growth is quite common. In other alloys where it is possible to further undercool the liquid or promote nucleation, it is possible to develop equiaxed grain structures [68, 69]. These results suggest that Ni may also be suitable for promoting equiaxed grains, although the precise solidification details (e.g., Marangoni convection, undercooling, growth restriction [70]) have not been established. Nominally, this should result in phases that are at or near equilibrium composition. This aging condition is in line with standard aging conditions for other Ti-based alloys, including the AMS 4999A specification [71, 72]. The specimens were then air-cooled down to room temperature.

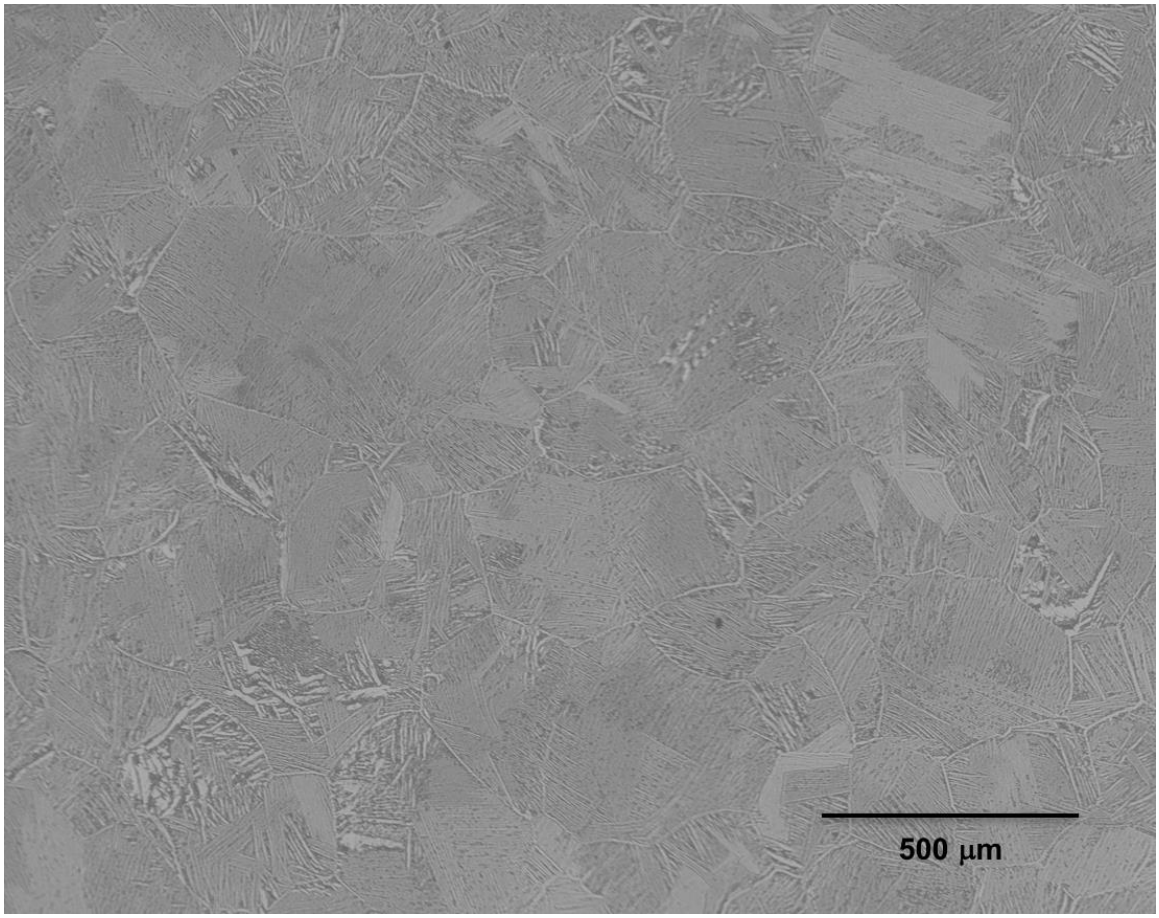

Figure 14 - Optical micrograph from Location 2 (~4.4wt% Ni) following deposition, solutionization, and aging. The build direction is from bottom to top in this micrograph.

After aging, the sample was further sectioned longitudinally (see Figure 13(b)), prepared for metallography and indentation tests. The sample preparation involved a specific sequence of steps that proceed through grinding (P240, P1200 SiC paper) and then finished with polishing steps with decreasing abrasive particle size (9μm, 3μm, 1μm diamond suspension), with each step ensuring that the surface deformation introduced is removed in the next step. The importance, particularly in indentation, of removing the damaged layer from mechanical polishing without introducing further mechanical

deformation has already been expounded [23]. This is mainly because of the very small indentation volumes involved in the indentation protocols employed in this work. We opted for a final polishing step using solution mixing 5 parts of 0.06 μm colloidal silica suspension with 1 part of hydrogen peroxide. Similar sample preparation protocols were successfully employed in prior nanoindentation work on titanium alloys [21].

5.1.2 High Throughput Characterization

Our focus in this case study is to explore the correlations between chemical composition induced salient microstructure descriptors such as phase volume fractions and spacing of intermetallic phase (same as the length scale of the matrix phase) and their associated mechanical properties measured by indentation (i.e., indentation modulus, indentation yield strength, and indentation hardening rate). For this purpose, five locations were chosen longitudinally for microstructure characterization and indentation tests (see Figure 13 (b) and (c)). Since the longitudinal direction was controlled to have maximum compositional gradient and the horizontal direction should have no compositional gradient, the locations are intentionally picked to maximize the differences in local nickel compositions.

In addition, we are also interested in quantifying and correlating the variabilities in both the microscopy and the indentation measurements. With this goal in mind, multiple measurements were performed at each of the five selected locations. More specifically, they were performed on a 5 X 5 grid with a uniform spacing of 100 μm in both directions between the grid points (see Figure 13(c)). The selected spacing was

designed to be large enough to avoid interactions between neighboring indented zones (i.e., it is substantially larger than the estimated indentation zone size for each indentation). At the same time, it was designed to be small enough to ensure that the measurements on a single grid represent the microstructure and the property for a single chemistry. In other words, the compositional gradient within each grid is maintained to be very small and negligible for the present study.

In comparison with the conventional assays (tensile testing), the HT assays not only consume dramatically less volume, but also cost significantly less time and effort. Specifically, in this case study, five locations (corresponding to five distinct compositions which is the process variance of interest) are selected. Under the condition of tensile testing, five sets of standard tensile testing specimen (dumb bell samples) need to be made with each set having a unique composition. As mentioned in Chapter 2, manufacturing samples which reach certain level of reproducibility and homogeneity is itself a challenging task. Assuming the criteria discussed previously can be met, in order to form meaningful sample library, one still has to make at lease 25 sample bars in order to match the sampling rate applied in this study. A comparison between conventional and high throughput assays is shown schematically in Figure 15.

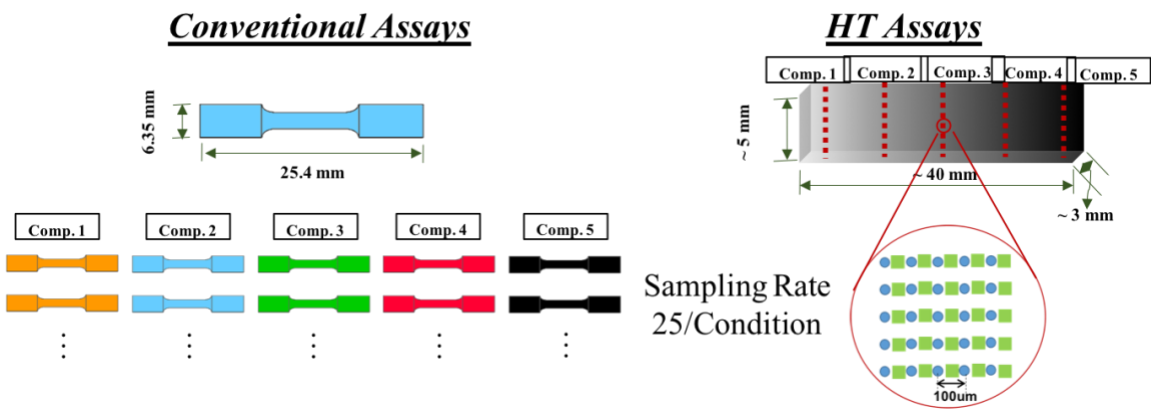

Figure 15 – Schematic of conventional assays and high throughput assays. Conventionally, homogeneous specimen of standard geometry needs to be manufactured in large quantities and with fair consistency. HT assays work with most geometries and only require small quantities.

Based on previous experimental studies at GT research labs, a rough estimation of the sample volume and time consumption for standard tensile testing is made. It is further compared to the high throughput assays in Figure 16 and Figure 17. The volume consumption for testing under high throughput assays is about 167 times less than testing under conventional assays. It should be emphasized that the selection of 5 compositions (conditions) and 25 tests per composition (condition) is rather arbitrary. Under current HT sample stripes, there is no reason to limit the number of compositions (conditions) to 5 and the sampling rate can be easily increased to several hundred per condition. Because the volume required in conventionally assays is proportional to the number of compositions (conditions) and the sampling rate, while the volume required in the high throughput assays is fixed. The reduction of volume consumption could reach to over 1000 times when the test number scales up. One the other hand, the time cost of HT assays is about 25 times faster than conventional assays. Generally, the testing process

can be separated into four stages – sample preparation, testing preparation, testing and post-test analysis. Although the testing time and post-test analysis time are proportional to the test number, HT assays have fixed preparation time which is a significant portion of total time cost. Similar to the volume consumption, the time cost in conventional assays could easily scale up as every stage of testing is proportional to the test number. It follows that the difference in time cost could reach to over 100 times as the test number increases.

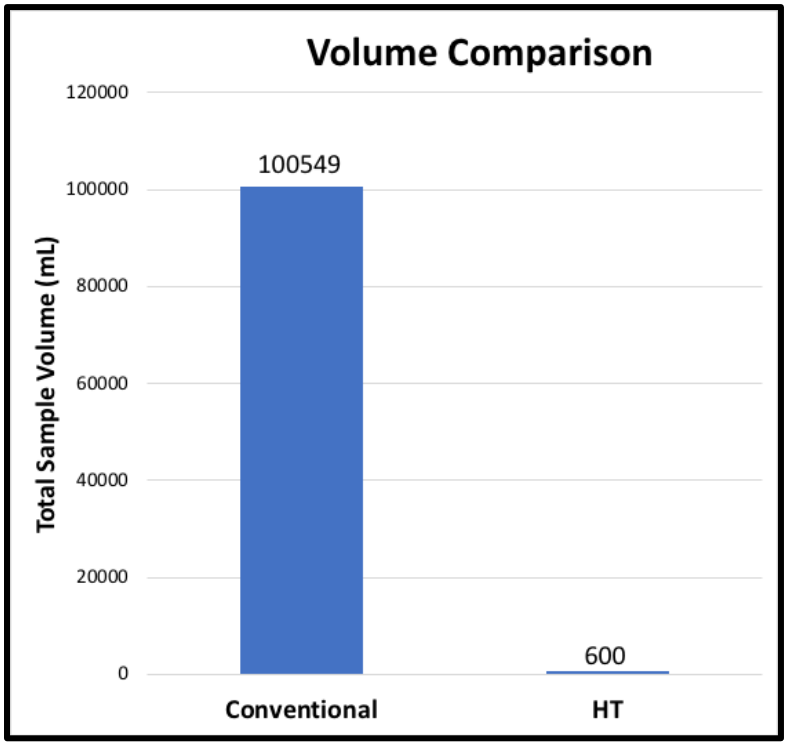

Figure 16 – Volume comparison between conventional assays and high throughput assays. The estimation is based on ASTM E-8 standard, assuming sampling 5 conditions at the sampling rate of 25 per condition.

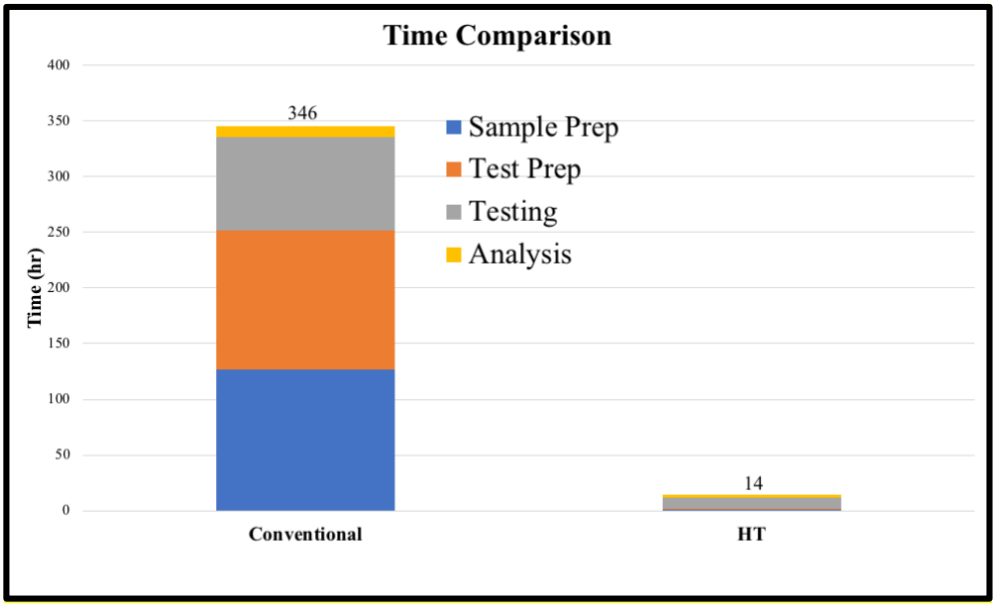

Figure 17 – Time consumption comparison between conventional assays and high throughput assays. The estimation is based on previous study [42].

5.1.3 Results

5.1.3.1 Microstructure Characterization

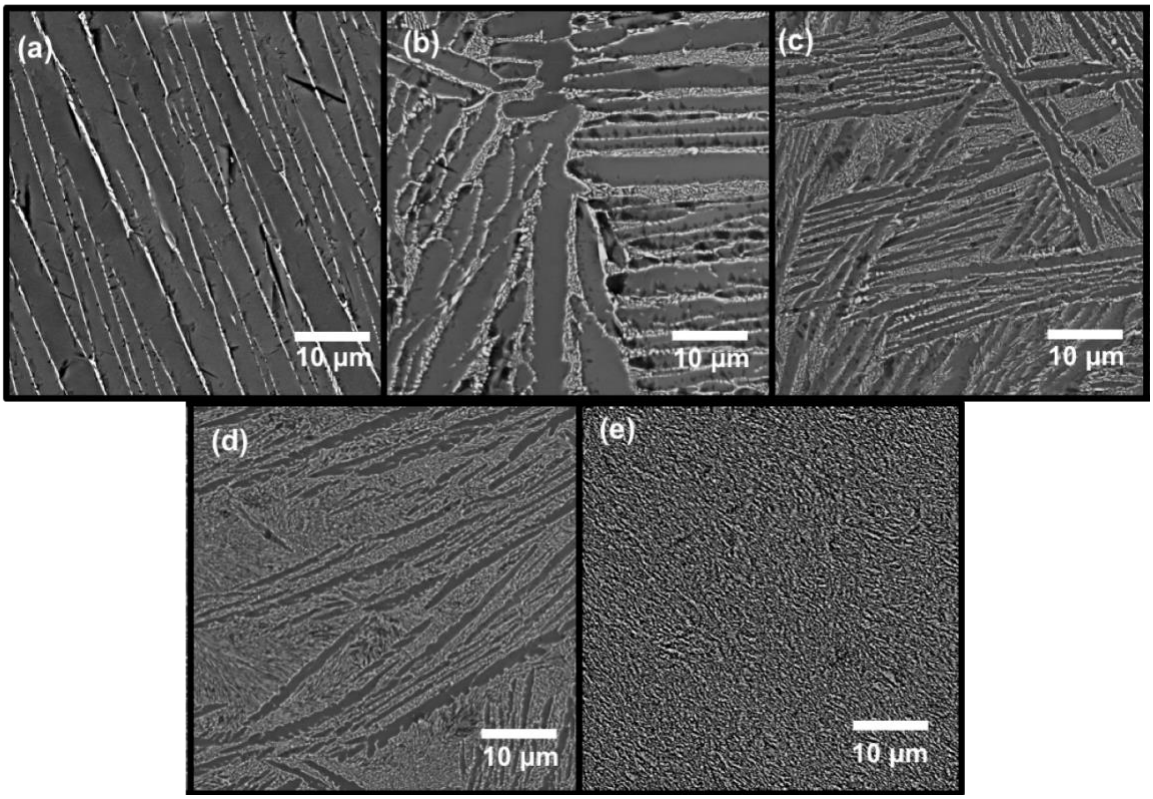

Figure 18 - (a) – (e) SEM Backscattered electron (BSE) images corresponding to locations 1 – 5 shown in Fig. 3(b), respectively, depicting the different Ni compositions and microstructures. The darker phase in the figures is α-Ti, while the brighter phase is the Ti_2Ni intermetallic. Composition for each location is provided in Error! Reference source not found.**.**

Back-scattered electron (BSE) images were captured using a Tescan Mira XMH field emission scanning electron microscope (SEM) with 20kV accelerating voltage. Figure 18(a-e) show typical BSE micrographs from the five different locations identified in Figure 13(b) on the graded sample. In these micrographs, the hcp α-phase and the decomposed β-eutectoid product (Ti_2Ni+β) are visible as the darker and the brighter components, respectively. The observed differences in the microstructures from each location are attributed largely to the difference in nickel composition, controlled by the

powder mixture in the AM process. The Ti_2Ni FCC intermetallic results from a rapid decomposition of the prior bcc β-Ti phase. Given its very rapid transformation, it tends to appear as very fine precipitates that decorate the prior α/β boundaries. In locations 1 and 2, the intermetallic appears as lamella, which is a consequence of the previously present α-laths. The decomposed β region is thicker in location 2 when compared with location 1, consistent with the increase in the Ni content and an increase in β-stability prior to the decomposition to the hcp α-Ti and fcc Ti_2Ni product. The intermetallic phase at locations 3, 4, 5 are more dispersed, resulting from the difference in the starting microstructure and the probable co-evolution of the hcp α-Ti and fcc Ti_2Ni intermetallic phases. Energy dispersive spectroscopy (EDS) analysis was done using Hitachi SU8230 SEM with Oxford EDAX and Aztec analysis software. Beam calibrations were done using 100% copper plate for EDS quantification. The operating conditions were kept at 20 kV accelerating voltage, 20 μA beam intensity. A map sum spectrum was measured to obtain average nickel content for each location shown in **Error! Reference source not found.**, a nd the dwell time was kept at 10 s.

5.1.3.2 High Throughput Mechanical Characterization

Spherical nanoindentation tests were performed at twenty-five grid locations for each of the five sample locations identified in Figure 13. These were performed on an Agilent G200 with a continuous stiffness measurement (CSM), which performs many small unloads with a superimposed harmonic signal on the prescribed monotonic loading.

The CSM allows a reliable estimation of the radius of the contact boundary at all indentation loads throughout the entire indentation. A spherical diamond tip with a nominal radius of 100 μm was used for all tests. An indenter tip radius of 100 μm produced a contact radius of about 7 microns at yield (contact area of roughly 150 sq. μm), and was hence able to capture the mechanical response of a region containing both the matrix and the Ti_2Ni intermetallic phases. We performed tests under a constant strain rate (loading rate over load) of 0.05/s and indented up to 800 nm in depth. CSM was set at an oscillation of 45 Hz and displacement amplitude of 2 nm. Figure 19 shows representative indentation stress strain (ISS) curves generated using the protocols described earlier. **Error! Reference source not found.** lists the elastic modulus, i ndentation yield strength and hardening parameters averaged over the 25 indents for each location.

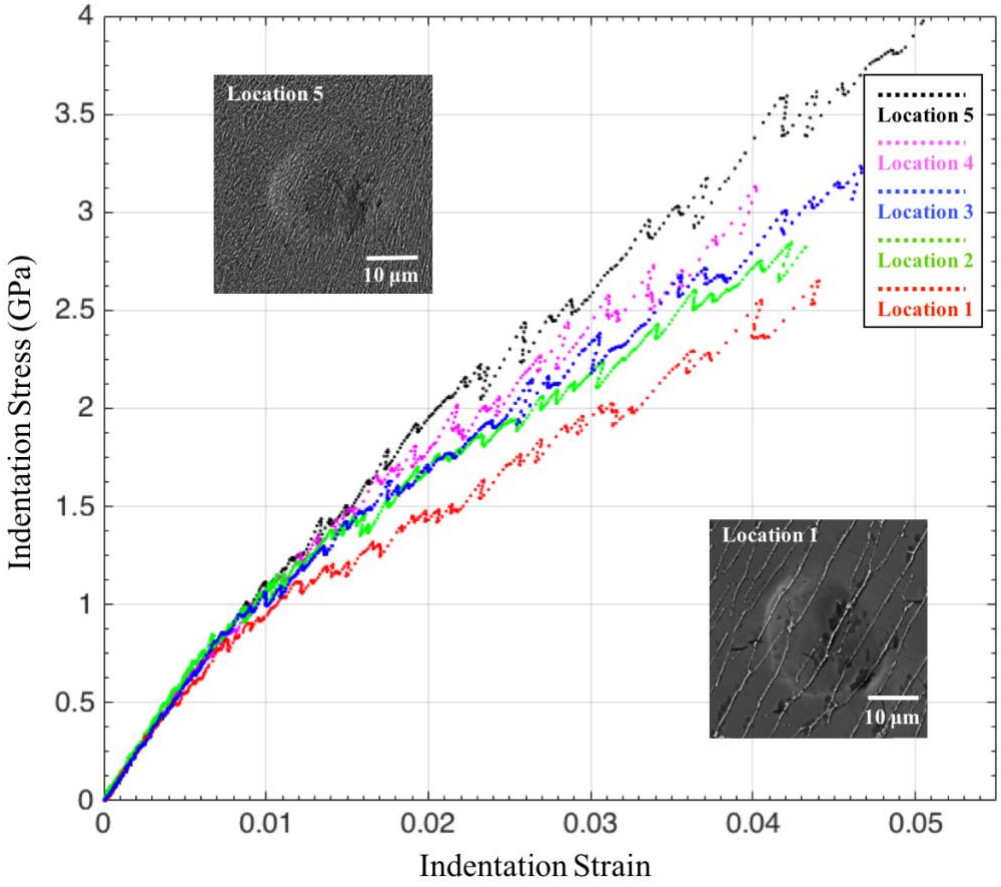

Figure 19 - The representative mechanical response and SE-BSE micrographs from spherical indentation tests.

5.1.3.3 Structure-Property Correlation

Given the type and amount of information aggregated in the study, several idealizations and simplifications had to be made in seeking the structure-property correlations of interest that could guide future efforts. First, it was decided that SEM imaging for microstructure analysis would be done adjacent to the actual indented zones (see Figure 13). Since it is currently very difficult to document the material structure in

the indented zone in a non-destructive but high throughput manner, this approximation is unavoidable as well as reasonable since microstructure heterogeneity would be low at the length scales at which structure is being quantified. Next, it was decided that each microstructure scan would cover a region of 50 μm X 50 μm. This scan size is designed to be somewhat larger than the indented zone size, but not too large that the gradient in the composition would have any significant effect. It was also decided that the microstructure would be characterized using BSE in the SEM, as this is a sufficiently fast technique and provides reliable contrast to allow measurements of phase volume fractions and averaged lengths. The lattice orientations of the grains in the indented zones were not measured in this work. Although the grain orientation is expected to play an important role in the indentation properties of hcp metals [73-77], these dependencies are most clearly seen in indentations performed with smaller indenter tips where the indented zones are fully embedded in a single grain. In fact, most of the prior work on the use of spherical indentation stress-strain curves was focused on single-phase coarse-grained polycrystalline samples [24, 45]. Only recently, these protocols have begun to be applied to multiphase polycrystalline samples [21]. Some anisotropy was observed in the residual indents at the indentation sites with low volume fractions of intermetallic precipitates (see the elongated residual indent shapes at location 1 micrograph in Figure 19). The anisotropy was significantly lower at indentation sites with higher volume fractions of the intermetallic precipitates, as seen in the more circular residual indent shapes (see location 5 micrograph in Figure 19). Additionally, the measured values of the indentation moduli and yield strengths (**Error! Reference source not found.**) at each sample location s howed only a modest variance (less than 10% in all cases). This variance is significantly

lower compared to the variation observed in the indentation yield strengths with the increase in the volume fraction of the intermetallic precipitates. As a result of these observations, we are fairly confident that the mean values reported in **Error! Reference s ource not found.** are not strongly influenced by the differences in the local microstructure in the multiple indentation volumes probed at each sample location. It also appears that the local mechanical anisotropy in the indentation probe volumes is largely mitigated by the presence of the intermetallic precipitates in our samples.

Several different approaches were explored in this study to quantify the microstructure information. First, BSE micrographs were segmented by Otsu's method [78, 79] which separates two classes of pixels in images, in accordance with the two-phase nature of this sample. Then, the segmented binary images were used to calculate volume fraction of the intermetallic phase. The averaged value of the volume fraction estimated at each of the five locations is reported as V_{int} in **Error! Reference source not f ound.**. Chord length distributions (CLD) [80] from the segmented images were also collected. CLD effectively captures the shape and size distribution of phases in any given microstructure. It is closely related to the lineal-path function [81], and is likely relevant to the prediction of the effective plastic properties [80, 82]. For the CLD computation performed in this study, horizontal chords that are fully in the α-Ti matrix with ends abutting a phase boundary are identified and analyzed. The averaged value from each CLD was reported as the feature length scale for the matrix phase, L in **Error! Reference s ource not found.**. The direction of chords for CLD computation was chosen arbitrarily because the feature length scale would be measured and calculated from multiple images of multiple grains. **Error! Reference source not found.** summarizes the measured v

alues of the volume fractions of intermetallic phase and the averaged feature length of the titanium matrix, along with the corresponding indentation properties measured in this study.

Table 2 - Average measurements at each of the five locations studied in the high throughput (HT) sample produced for this study. Indentation modulus, E_{ind}, indentation yield strength, Y_{ind} and indentation hardening rate, H_{ind} are estimated from the analyses of indentation data. The averaged volume fraction of intermetallic phase, V_{int}, the averaged chord length in the matrix, L are calculated from image analyses. The weight percentage of nickel is measured using Energy Dispersive Spectroscopy (EDS).

	Location 1	Location 2	Location 3	Location 4	Location 5
E_{ind} [GPa]	120.2 ± 9.0	126.5 ± 4.8	120.5 ± 4.6	122.7 ± 4.9	122.3 ± 1.9
Y_{ind} [GPa]	1.06 ± 0.09	1.16 ± 0.10	1.15 ± 0.05	1.26 ± 0.06	1.37 ± 0.04
H_{ind} [GPa]	47.0 ± 3.0	53.0 ± 3.7	59.9 ± 4.0	52.5 ± 3.5	70.5 ± 3.5
V_{int} [%]	5.5 ± 0.7	15.98 ± 1.44	23.1 ± 0.9	27.85 ± 1.77	35.8 ± 1.6
L [μm]	4.07 ± 1.02	1.42 ± 0.31	0.73 ± 0.08	0.53 ± 0.04	0.33 ± 0.03
wt% of nickel	1.50	4.35	7.23	8.06	11.13

The volume fraction of the intermetallic phase and the feature length of the titanium matrix are used here to establish correlations with the mechanical properties measured locally with the spherical indentation protocols. These correlations were quantified using the Pearson product-moment correlation coefficient [83] in Table 2. This

coefficient measures the linear dependence between two variables in the range [83], where positive (negative) value indicates positive (negative) correlation. A larger absolute value implies that the relationship is more likely to be described by a linear equation.

Table 3 - Pearson product-moment coefficient between different structure and property measures obtained on the HT sample.

	V_{int}	$L^{-0.5}$
E_{ind}	0.0857	0.0289
Y_{ind}	0.9481	0.9533
H_{ind}	0.8426	0.8519

5.1.4 Discussion

Quantitative correlations of the local mechanical properties measured in indentation to the bulk mechanical properties typically measured in standardized testing (e.g., simple compression) are still under development [37]. The main issues in this

correlation are indeed related to the differences in the probe volumes and the inherent anisotropy of material response at the probed length scales. At this time, these correlations are most mature at the two ends of the spectrum of applications: (i) the indented volume is very large compared to the representative volume element of the material microstructure, and allows idealization of the material response in the indentation zone as a homogeneous isotropic medium [27, 42], and (ii) the indented volume is a single phase crystalline region (e.g., a region within a grain in a single-phase polycrystalline sample) [21, 27, 38, 84]. Clearly, the indentations in the sample studied here do not fall into either of these idealized conditions.

As mentioned earlier, the microscale features of interest in interpreting the indentation measurements are the spatial distributions of grain orientations and precipitates in the indentation volumes. In most of the indentations conducted here, the indentation zones are significantly smaller than the grain sizes (200 ~ 300 μm), but are larger than the precipitate sizes. As noted earlier, the presence of the precipitates has mitigated some of the grain orientation-induced anisotropy associated with the indentation measurements reported here. Consequently, our indentations in multiple grains at the same location in the sample have not revealed a strong variation, especially when compared to prior work on α-Ti [27]. We therefore believe that the averaged values from the multiple indentations presented in **Error! Reference source not found.** could s erve as good surrogate measures of the bulk properties that might be measured in standardized testing. However, it should be noted that the averaged indentation values do not capture any Hall-Petch effects [46] from the grain boundaries (note that these were

not present in any of the indentations reported in this study). If grain size effects are significant (compared to the effects of the precipitate size and volume fraction) then one needs to conduct larger indentations that sample a few grain boundaries in the probed volumes.

Because of its dependence on interatomic bonding [85], the elastic modulus is expected to be impacted by the alloy composition, distribution of grain orientations [21, 86] and the phase volume fraction. Using the shear and bulk modulus values estimated previously by Toprek et al. [87], one might expect the elastic modulus of Ti_2Ni to be approximately 149 GPa. This value is significantly higher than the value of 105 GPa reported in literature for CP Ti [88]. The indentation moduli measured in this study did not show significant variations between the different locations on the HT sample, and fell in the range of 120-126 GPa. The corresponding values of Young's moduli would fall in the range of 109-115 GPa. This range of values is quite reasonable, keeping in mind the values of the Young's moduli mentioned earlier for the constituent phases. If one were to use the rule of mixture, based on the volume fraction of the intermetallic phase, the predicted values of Young's moduli for the five locations would be in the range of 107-121 GPa. It is therefore clear that the moduli measured by indentation protocols described in this work are quite reasonable and reliable. The very small location-to-location variation of the measured Young's modulus also explain the low values of the correlation coefficients between the indentation moduli and both the intermetallic volume fraction as well as the averaged matrix chord length (see **Error! Reference source not found.**).

As seen in **Error! Reference source not found.**, the indentation yield strengths i

ncreased systematically with the increase in Ni content. Furthermore, these are highly correlated with the microstructure measures (**Error! Reference source not found.**). As e xpected, there is a strong positive correlation between the indentation yield strength and the volume fraction of the intermetallic phase. Similarly, there is a strong positive correlation between the indentation yield strength and the averaged chord length raised to a power of -0.5 (following the well-known Hall-Petch relations [46]).

Several strengthening mechanisms including solid solution strengthening, strengthening due to secondary phase, and grain boundary strengthening are likely to contribute to the observed increase in indentation strength with the increase in Ni content. In terms of solid solution strengthening in the matrix, the presence of Ni in pure Ti is expected to increase yield strength by 35MPa per wt% addition [89]. Presence of oxygen is also expected to make a significant contribution to increasing the matrix yield strength. For example, it has been reported in literature that the yield strength of titanium can increase from 100MPa (pure titanium) to 480MPa (grade 4 CP titanium), mainly due to increased oxygen content. Furthermore, we should also expect a contribution from phase strengthening due to the intermetallic phase [85].

The measured indentation yield strengths can be converted to simple compression yield strengths using a factor of 2.0 [37]. Furthermore, fitting the estimated simple compression yield strengths at the five locations to the self-consistent model of Stringfellow-Parks [90] (this model uses only the volume fraction and yield strengths of the constituent phases), we estimated that the yield strength of α–Ti would be in the range of 400-600 MPa and that of Ti_2Ni would be in the range of 1.1-1.2 GPa. These

ranges are quite reasonable based on the values reported in literature for grade 4 CP titanium mentioned above and the reported values of 0.9-1.6 GPa [88] for Ti_2Ni.

It should be noted that our measurements indicated a strong correlation (see **Error! Reference source not found.**) between the indentation yield strength and the a verage chord length in the matrix raised to a power of -0.5 (the simple model of Stringfellow-Parks [90] employed above does not explicitly account for this). Similar observations have also been reported in earlier work studying the effect of decreasing alpha lamellar colony size on strengthening of Ti alloys [91]. In order to capture the effect of both volume fraction of the intermetallic phase (V_{int}) and the averaged chord length (L) in the matrix, we explored in this study a simple linear model of the form (inspired by the well-known Hall-Petch laws [46])

$$Y_{ind} = a_0 + (a_1 + a_2 V_{int})/L^{0.5} \tag{15}$$

where a_0, a_1, and a_2 are the fit (material) constants. The multivariate linear regression estimated the values of a_0, a_1, a_2 as $1.0747\ GPa$, $0.0335\ MPa \cdot m^{0.5}$, $0.5665\ MPa \cdot m^{0.5}$, respectively. The goodness of the fit is shown in Fig. 7, and the mean absolute error was calculated to be 0.0209 GPa or 1.74 %.

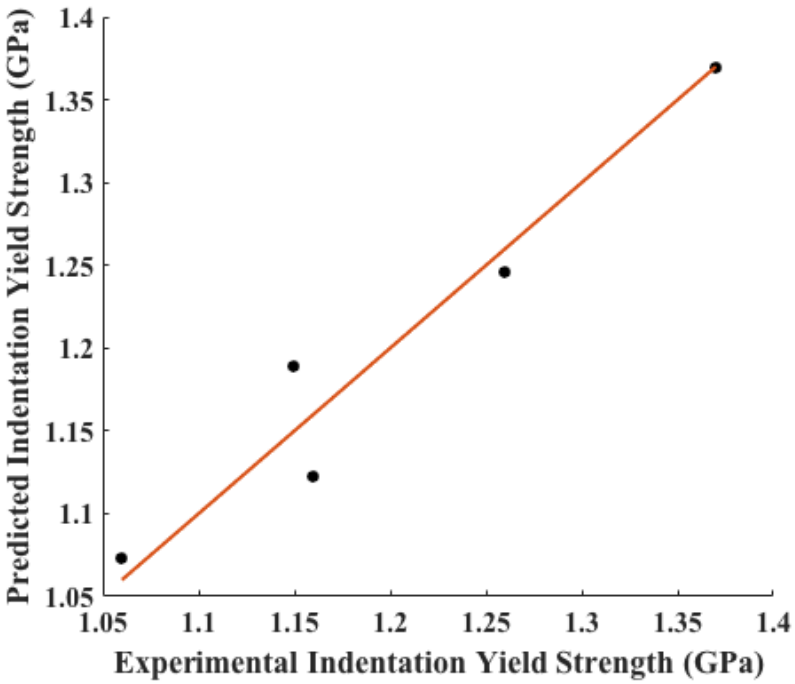

Figure 20 - Goodness of the fit for the model predicting indentation yield strength based on the volume fraction of intermetallic phase and the averaged chord length in the matrix (see Eq. 1)

The hardening values extracted from the indentation stress-strain protocols employed here are much higher than the values measured typically in conventional simple compression tests. This observation has been made consistently in all prior work with the indentation stress-strain protocols [21, 27] and does not yet have a clear explanation. At this time, the increased hardening rates in the indentation stress-strain curves are generally attributed to the fact that the elastic-plastic transition in these tests occurs over a much larger strain range compared to conventional simple compression stress-strain curves [37]. Nevertheless, these values can be used as relative measures to compare the hardening rates at the different location on the HT sample. A 50% increase

is observed in the hardening rates from location 1 to 5. Location 2 shows a small increase (12.7%) over location 1. Locations 2, 3 and 4 seem to show similar hardening rates. A sharp increase is seen in the hardening rate is noted for location 5 (approximately 34%). It should be generally expected that hardening rates would increase with an increase in the interface area per unit volume. For the present study, this is captured indirectly by the averaged chord length of the matrix. Clearly, this variable has a significant effect on the hardening rates exhibited by the sample, especially as the chord lengths decrease to very low values.

A high throughput approach to explore mechanical properties of AM alloys with different material chemistries has been presented and demonstrated on Ti-Ni alloy systems. The LENS process has been shown to successfully produce controlled variations in material chemistry and microstructures (Figure 18) along the length of the manufactured sample. We were able to achieve reasonable variation in terms of phase distribution and volume fraction of the Ni-rich second phase (Ti_2Ni) within a 38 mm sample. Similarly, spherical indentation protocols have effectively generated. Finally, the meaningful trends for structure-property relations were build, as depicted in Figure 19, Table 1 and 2.

5.2 Compositional Gradient and PBHT Effects on Titanium-Manganese Alloys

In the second case study of this chapter, not only compositional effects, but also thermal history (specifically, post build heat treatment (PBHT)) effects will be included in our scope of investigation. Similar to the first case study, Ti-Mn alloys was selected

because it is a model eutectoid β-stabilized system, which is traditionally susceptible to problems such as β-fleck and hence is not considered for conventional cast/wrought titanium alloys. In hopes of avoiding β-fleck and increasing strength properties, this system was chosen to be manufactured under additive manufacturing.

As a clear and influential factor determining characteristics of alloys, composition was naturally chosen to be the subject of the study. Subsequently, Ti-Mn alloys, whose Mn composition ranges between 0-12%wt (Figure 21), were selected. All the sample stripes were carefully manufactured with gradient over the vertical direction (similar to Figure 13(a)).

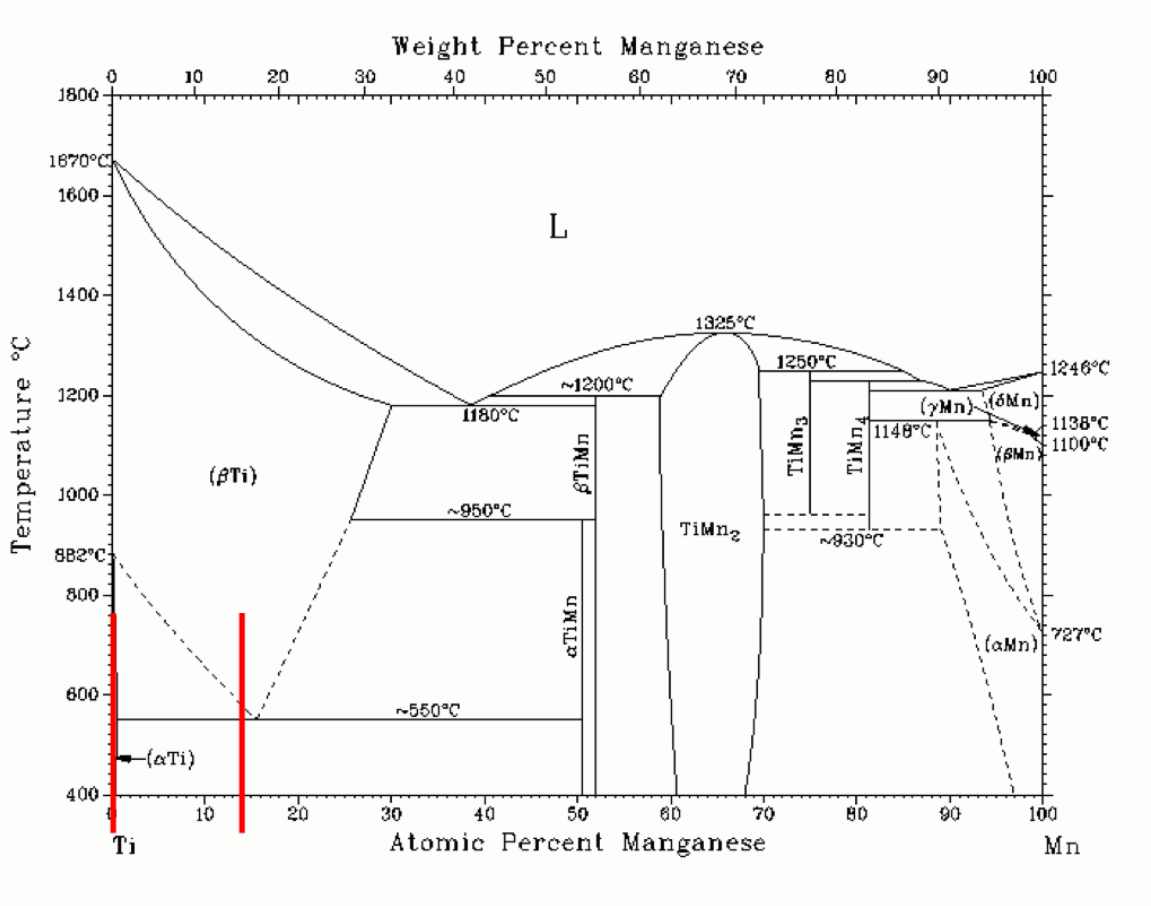

Figure 21 - The Mn-Ti phase diagram (adapted from Massalski *et al.*, 1990[57]). The region of interest in this study is labeled with two red lines (manganese composition range of 0 – 12 wt%).

Combined with compositional differences, variances in thermal histories are also deliberately introduced in the system to explore the materials space of Ti-Mn alloys. Specifically, the thermal parameter of interest is the aging temperature in post build heat treatment. Due the high power of energy source, the subsequent high temperature of melting pool, the fast cooling process and the high build rate involved in LENS technique, the as-manufactured part often bears relatively high residual stress, which, in many practical applications, is not desired. The post build heat treatment process, especially

aging becomes an essential step before the final product. In this case study, each sample stripe mentioned above went throughput a different aging temperature (nominally, 500 °C, 600 °C and 700 °C, respectively) and were held at that temperature for four hours.

The objective of this case study is to provide both microstructure and mechanical properties information and build linkages with uncertainties in HT fashion on a library of AM TiMn alloys which contains thermal history and chemistry combinations.

5.2.1 Materials and Process

This section will introduce the materials and the specifics on the process of all three sample stripes. Most of the details in this section is provided by team from Professor Collins group at ISU.

Owing to the very small molten pool relative to the specimen size, it is possible to independently control and feed multiple material sources with heat sources in additive manufactured specimens. Taking advantage of this idea in conjunction with the LENS™ technique, we executed high throughput (HT) processing to produce samples for this study. Previously, this technique has been used to study composition-microstructure relationships and composition-property correlations for hydrogen storage, oxidation resistance and magnetic properties [59-63]. Use of elemental powder blends [64, 65] avoids pre-alloyed powders. It substantially benefits this type of AM in that a library of materials with a tunable range of chemistries and process parameters can be produced within a small volume sample with relatively low cost, which potentially promotes a high throughput approach. It should be noted that the LENS™ generated materials can exhibit

strong variations from one sample location to another in the distributions of grain orientations, phases, composition and residual stress states, which can have a pronounced effect on the mechanical properties specific to the location in the sample [66]. Indeed, this study turns this into an advantage, especially in the context of high throughput assays, by treating the material volumes at different locations associated with distinctly different combinations of local chemistry and local (thermo-mechanical) processing history (in this case study post build aging temperature) as distinct samples.

An Optomec LENS™ 750 system (see Figure 11), equipped with two powder feeders, was used to deposit compositionally graded Ti-Mn specimens for the present study. This system incorporates an Nd:YAG laser operating at a wavelength of 1064 nm. The power of the laser was ~350W. Cylindrical specimens were made with a diameter of ~10 mm, and a height of ~38 mm (similar to Figure 13(a)). The motion control file was modified to change the powder flow rates at certain layers to pre-determined powder flow rate set points. This made the control of sample composition gradient possible. For this work, the material fed into the LENS™ system were blends of 99.9% pure titanium powder (> 150 μm) from Alfa Aesar and the composition range was from pure Ti to Ti-12 wt%Mn**.** In titanium alloys, LENS™ deposition results in non-equilibrium microstructures. Further, most industrial applications require subsequent heat-treatments to the deposition [67], resulting in close-to-equilibrium microstructures. Therefore, following deposition, the as-deposited Ti-Mn cylinder was subjected to a heat treatment by sectioning into pieces, wrapping the pieces in titanium foil, and encapsulating in a quartz tube with a titanium sponge to act as an oxygen getter. These samples were β-solutionized below the eutectic temperature (< 942°C) for 4 hours to ensure local

chemical homogeneity and reduction/elimination of any residual stress created during deposition so that residual stress is not a variable in this study. The sample was then step-quenched down to three distinct aging temperatures (T_{age} = 500 °C / 600 °C / 700 °C) and held at that temperature for four hours. Since the objective of the study was for a "rapid" assessment, this heat-treatment was based upon a time-temperature pairing for other titanium alloys which have been shown to produce close-to-equilibrium microstructures. Previous study results [68, 69] suggest that Mn may also be suitable for promoting equiaxed grains, although the precise solidification details (e.g., Marangoni convection, undercooling, growth restriction [70]) have not been established. Nominally, this should result in phases that are at or near equilibrium composition. This aging condition is in line with standard aging conditions for other Ti-based alloys, including the AMS 4999A specification [71, 72]. The specimens were then air-cooled down to room temperature.

After aging, the sample was further sectioned longitudinally (same as shown in Figure 13(b)), prepared for metallography and indentation tests. The sample preparation involved a specific sequence of steps that proceed through grinding (P240, P1200 SiC paper) and then finished with polishing steps with decreasing abrasive particle size (9μm, 3μm, 1μm diamond suspension), with each step ensuring that the surface deformation introduced is removed in the next step. The importance, particularly in indentation, of removing the damaged layer from mechanical polishing without introducing further mechanical deformation has already been expounded [23]. This is mainly because of the very small indentation volumes involved in the indentation protocols employed in this work. We opted for a final polishing step using solution mixing 5 parts of 0.06 μm colloidal silica suspension with 1 part of hydrogen peroxide. Similar sample preparation

protocols were successfully employed in prior nanoindentation work on titanium alloys [21].

5.2.2 High Throughput Characterization Methods

In this case study I will be focusing on exploring how chemical composition and post build aging temperature would alter microstructures and how the salient microstructure descriptors such as phase volume fractions and chord length distribution of each component phase would change their associated mechanical properties measured by indentation (i.e., indentation modulus, indentation yield strength, and indentation initial hardening rate). For this purpose, similar to the first study, five locations were chosen longitudinally at each sample stripe for microstructure characterization and indentation tests (see Figure 13(c)). Since the longitudinal direction was controlled to have maximum compositional gradient and the horizontal direction should have no compositional gradient, the locations are intentionally picked to maximize the differences in local nickel compositions. With the same protocol as the first case study, multiple measurements were performed at each of the five selected locations. More specifically, they were performed on a 5 X 5 grid with a uniform spacing of 100 μm in both directions between the grid points (see Figure 13(c)). The selected spacing was designed to be large enough to avoid interactions between neighboring indented zones and the compositional gradient within each grid is maintained to be very small and negligible for the study. This testing protocol then applied to all stripes with 3 different post build aging temperatures.

Similar to the first case study, a comparison between conventional and high throughput assays is shown schematically in Figure 22. In this case study, due to the increase of sample conditions from a second source – post build aging temperature, one has to make at lease 375 standard sample bars in order to form comparable amount of dataset acquired from this case study.

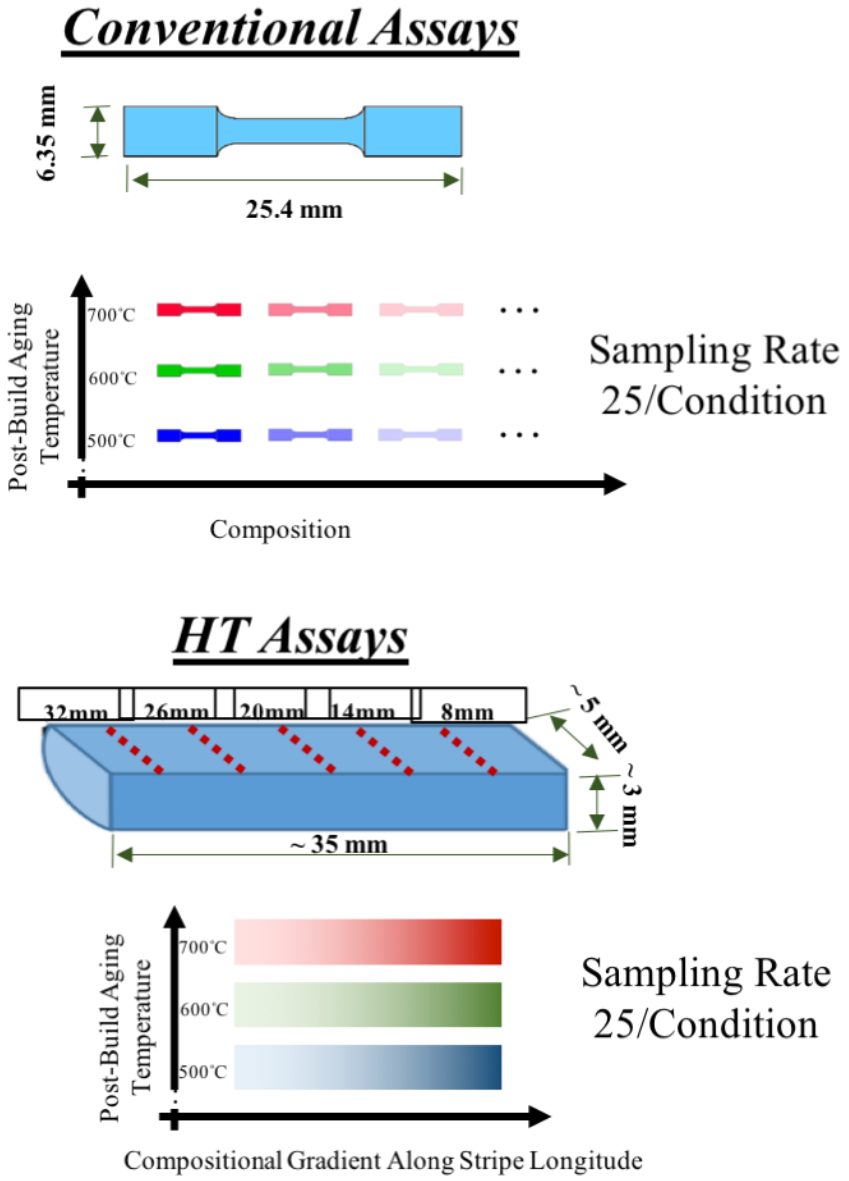

Figure 22 - Schematic of conventional assays and high throughput assays. Under conventional scheme (top part), standard specimen needs to be made in large quantities (at least 125 in this case study) and with fair consistency within sample volumes. Under HT scheme (bottom part), samples with irregular geometries and small sample volumes can be employed.

Based on previous experimental studies at GT research labs, a rough estimation of the sample volume and time consumption for standard tensile testing is also made in this case. It is further compared to the high throughput assays in Figure 16 and Figure 17. The volume consumption for testing under high throughput assays is about 244 times less than testing under conventional assays. It should be emphasized that the selection of 3 aging temperatures combined with 5 compositions (15 conditions) and 25 tests per condition is rather arbitrary. Under current HT sample stripes, there is no reason to limit the number of conditions to 15 and the sampling rate can be easily increased to several hundred per condition. Because the volume required in conventionally assays is proportional to the number of compositions (conditions) and the sampling rate, while the volume required in the high throughput assays is fixed. The reduction of volume consumption could reach to over 1000 times when the test number scales up. One the other hand, the time cost of HT assays is about 27 times faster than conventional assays. Generally, the testing process can be separated into four stages – sample preparation, testing preparation, testing and post-test analysis. Although the testing time and post-test analysis time are proportional to the test number, HT assays have fixed preparation time which is a significant portion of total time cost. Similar to the volume consumption, the time cost in conventional assays could easily scale up as every stage of testing is proportional to the test number. It follows that the difference in time cost could reach to over 100 times as the test number increases.

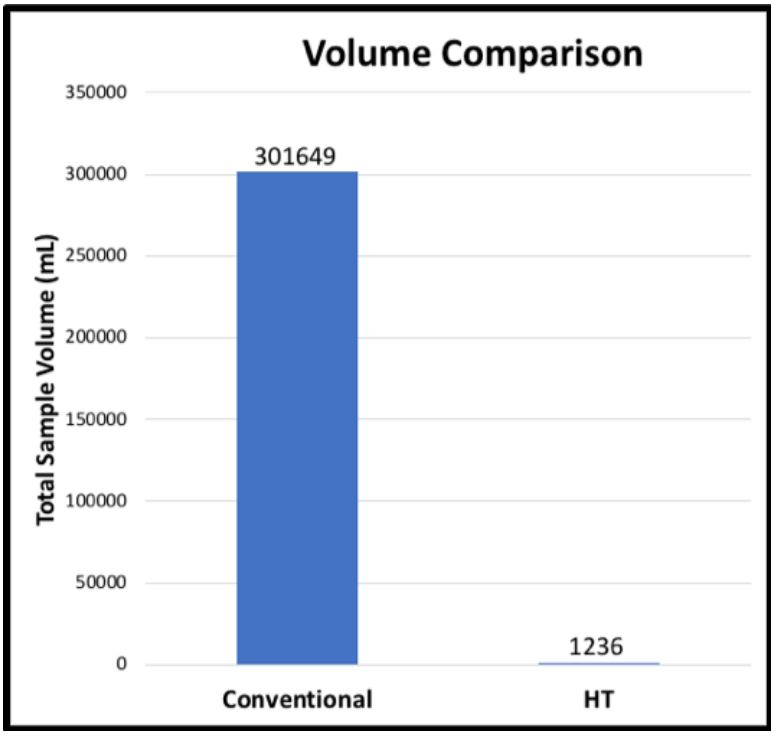

Figure 23 - Volume comparison between conventional assays and high throughput assays. The estimation is based on ASTM E-8 standard, assuming sampling 3 temperature conditions and 5 composition conditions (15 combinatorial conditions in total) at the sampling rate of 25 per condition.

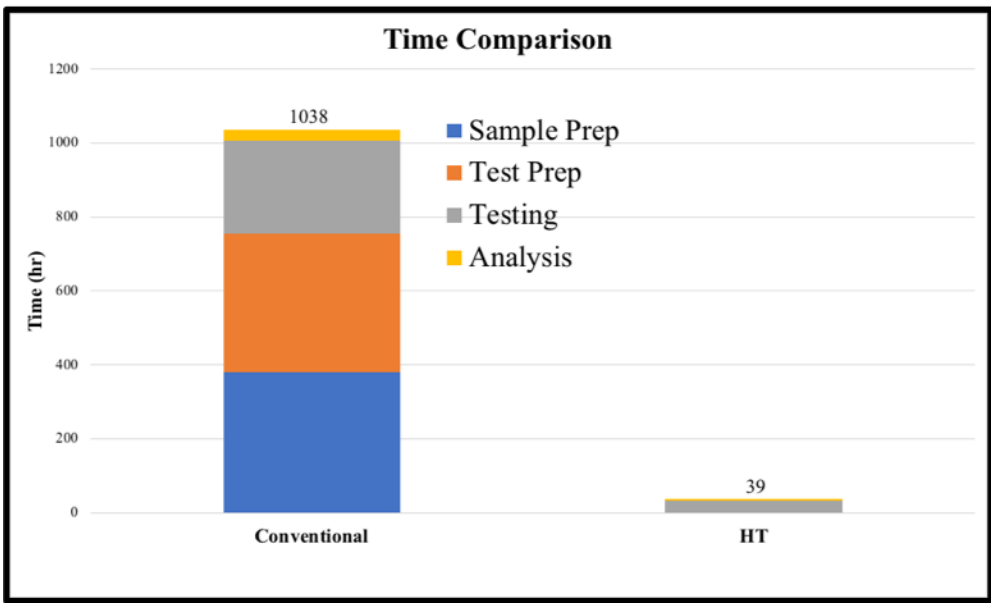

Figure 24 - Time consumption comparison between conventional assays and high throughput assays. The estimation on conventional assays is based on previous study [42].

5.2.3 Results

5.2.3.1 Microstructure Characterization

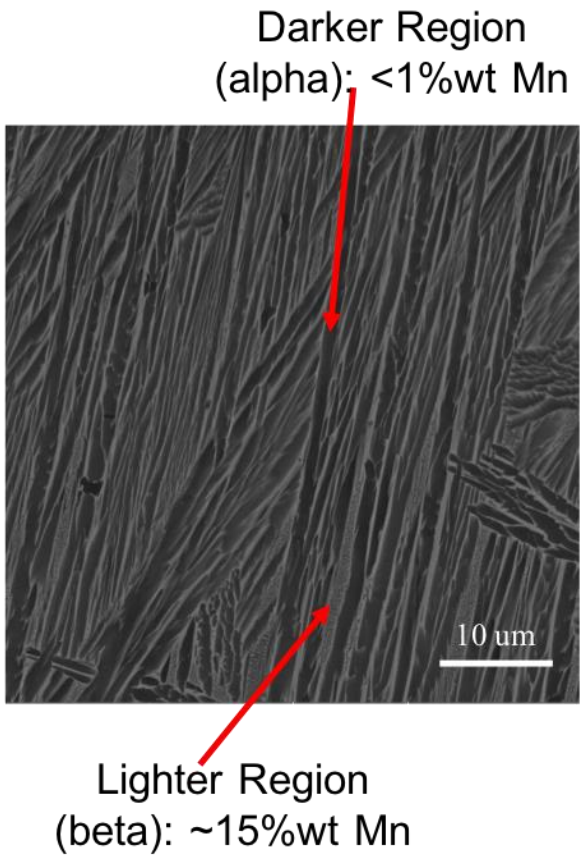

Figure 25 – SEM backscattered electron (BSE) images corresponding to the sample stripe which was aged at 500 ℃ for four hours and at the location where manganese composition is ~ 5.8 %wt. It depicts the dual phase microstructure of the sample. The darker phase in the figure is α-Ti, while the brighter phase is β-Ti.

Back-scattered electron (BSE) images were captured using a Tescan Mira XMH field emission scanning electron microscope (SEM) with 20kV accelerating voltage. Figure 25 shows a typical BSE micrograph from the sample stripes. In this micrograph, two distinct phases are visible as the brighter and darker components. Energy dispersive spectroscopy (EDS) analysis was done using Hitachi SU8230 SEM with Oxford EDAX and Aztec analysis software. Beam calibrations were done using 100% copper plate for

EDS quantification. The operating conditions were kept at 20 kV accelerating voltage, 20 μA beam intensity. Point spectrum was measured at both phases, detecting manganese content at less than 1%wt and about 15 %wt for the darker and brighter phases, respectively. Taken the phase diagram (see Figure 21) into consideration, the darker phase is identified as hcp α-Ti and the brighter phase bcc β-Ti.

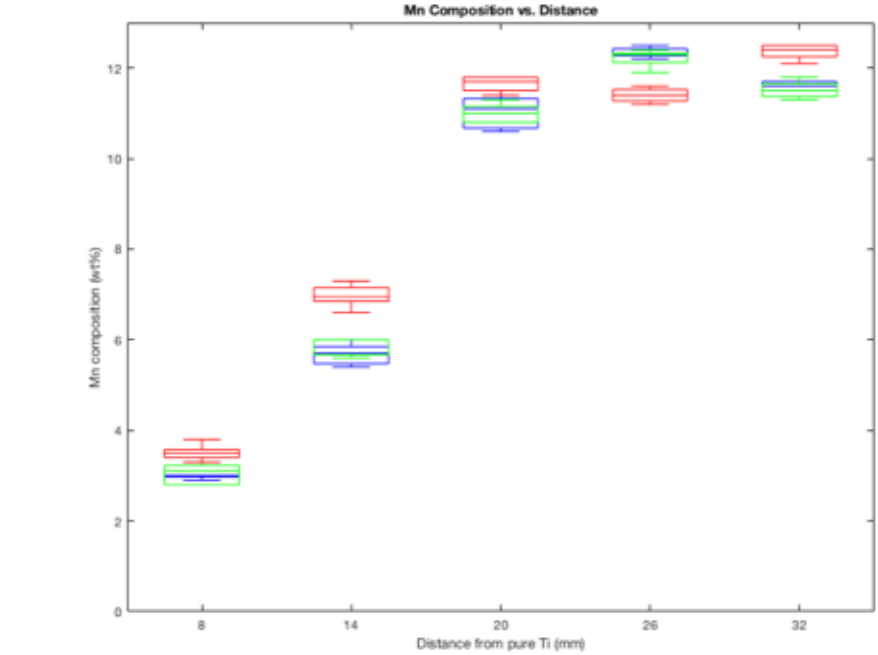

Figure 26 – Measurements of manganese weight percentage at each of the five locations of all three high throughput (HT) sample stripes. The results is measured using energy dispersive spectrum (EDS). The blue, green and read boxes corresponds to 500 °C, 600 °C and 700 °C stripe, respectively. Each box gives information of the median (middle line), highest 25 % (upper boundary of the rectangular), lowest 25 % (lower boundary of the rectangular), the highest (upper bar) and the lowest (bottom bar) measure.

A map sum spectrum was also measured to obtain average manganese content for each location of every sample stripes shown in Figure 26, and the dwell time was kept at 10 s. Each location (composition-temperature combinatory condition) was measured multiple time at multiple sites (shown as the bars in Figure 26). The manganese content peaks at ~ 20 mm from the pure titanium end of the stripes and stays at ~ 12 %wt for the rest of the sample.

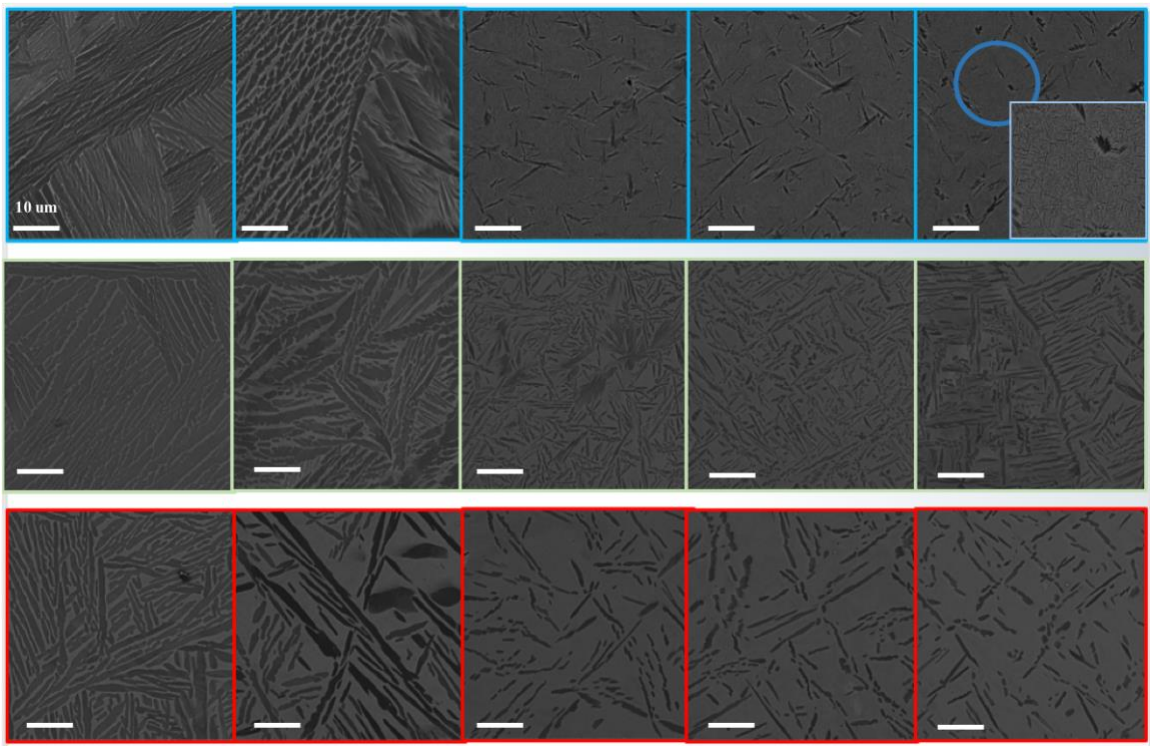

Figure 27 - SEM backscattered electron (BSE) images. The top row (blue edge) corresponds to 500 °C stripe, middle (green edge) 600 °C and bottom (red edge) 700 °C. Five columns from left to right correspond to five locations (8 mm, 14 mm, 20 mm, 26 mm, 32 mm) shown in Figure 22. The darker phase in the figures is α-Ti, while the brighter phase is β-Ti. Composition for each location is provided in Figure 26.

The observed difference in the microstructures from each location are attributed to the difference both in manganese composition and in post build aging temperature, controlled by the powder mixture in the AM process and heat treatment process after build. In location 1 and 2, particularly for the case of 500 ℃ and 600 ℃, α phase is dominant compared to lamella β phase. The inverse relation of the volume fraction between α and β in 700 ℃ stripe can be explained by the different tie lines in phase diagram (see Figure 21) as the post build aging process pushes the microstructure to a close to equilibrium state. As more manganese contained in the alloys (location 3, 4, 5), β phase increases, connecting each other and forming the dominant component of the microstructure, while α phase becomes small needle-like laths and more dispersed. Note that in location 3, 4, 5 of 500 ℃ stripes, significantly small (10 nm - 100 nm) secondary α phase [92] was found along with bigger (~2 um) α laths. Due to the lower aging temperature and the relatively slow diffusion rate of elements in Ti-Mn system, it is very likely the secondary α phase results from insufficient diffusion of titanium from β phase.

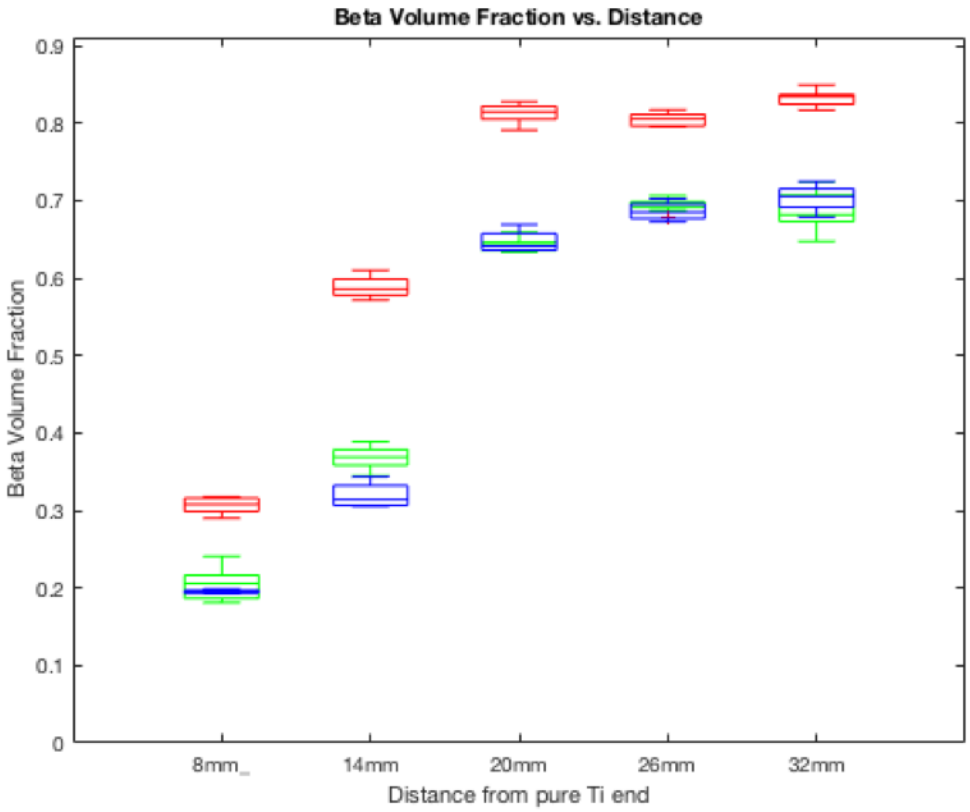

Figure 28 – β phase volume fraction corresponding to location 1 – 5 shown in Figure 22. The blue, green and read boxes corresponds to 500 °C, 600 °C and 700 °C stripe, respectively.

Several different approaches were explored in this study to quantify the microstructure information.

First, BSE micrographs were segmented by Otsu's method [78, 79] which separates two classes of pixels in images, in accordance with the two-phase nature of this sample. Then, the segmented binary images were used to calculate volume fraction of the β phase. The value of the volume fractions estimated at each of the five locations are

reported in Figure 28. More manganese generally promotes more β phase. And with the same Mn composition, higher temperature promotes higher beta volume fraction.

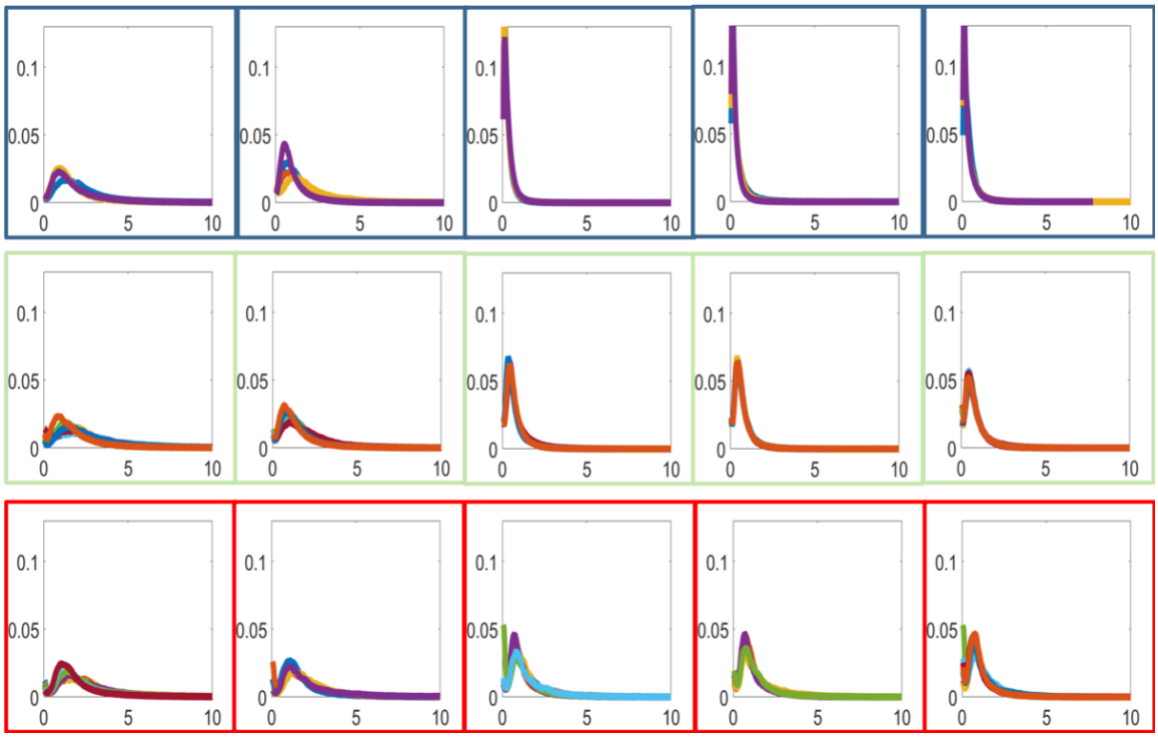

Figure 29 – Chord length distributions of α-Ti phase. The top row (blue edge) corresponds to 500 °C stripe, middle (green edge) 600 °C and bottom (red edge) 700 °C. Five columns from left to right correspond to five locations (8 mm, 14 mm, 20 mm, 26 mm, 32 mm) shown in Figure 22. X axis illustrate the length of the chord in micros and Y axis illustrate the probability density of the chords.

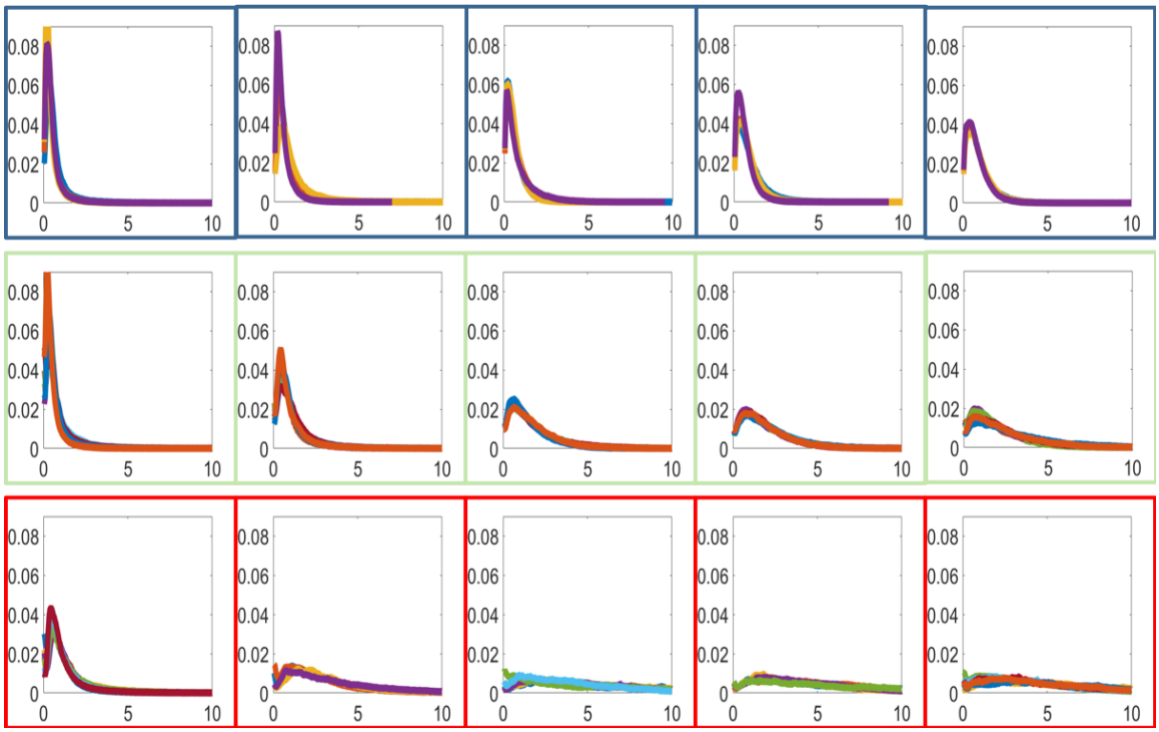

Figure 30 - Chord length distributions of β-Ti phase. The axis of each plot and the arrangement of the plots are identical as Figure 29.

Chord length distributions (CLD) [80] from the segmented images were also collected. CLD effectively captures the shape and size distribution of phases in any given microstructure. It is closely related to the lineal-path function [81], and is likely relevant to the prediction of the effective plastic properties [80, 82]. For the CLD computation performed in this study, chords that are fully in the α-Ti / β-Ti with ends abutting a phase boundary are identified and analyzed. The chords are collected angularly to avoid imaging orientation bias from manual selection. The CLD of each image is calculated from averaging all angles (72 angles are taken) of the image orientation. The averaged value from each CLD was reported as the feature length scale for each phase in Figure 31. Note that, different from the first case study where only averaged values of CLD from

each condition were considered, this case study will use the full spectrum of CLD to create correlations in section 5.2.3.3.

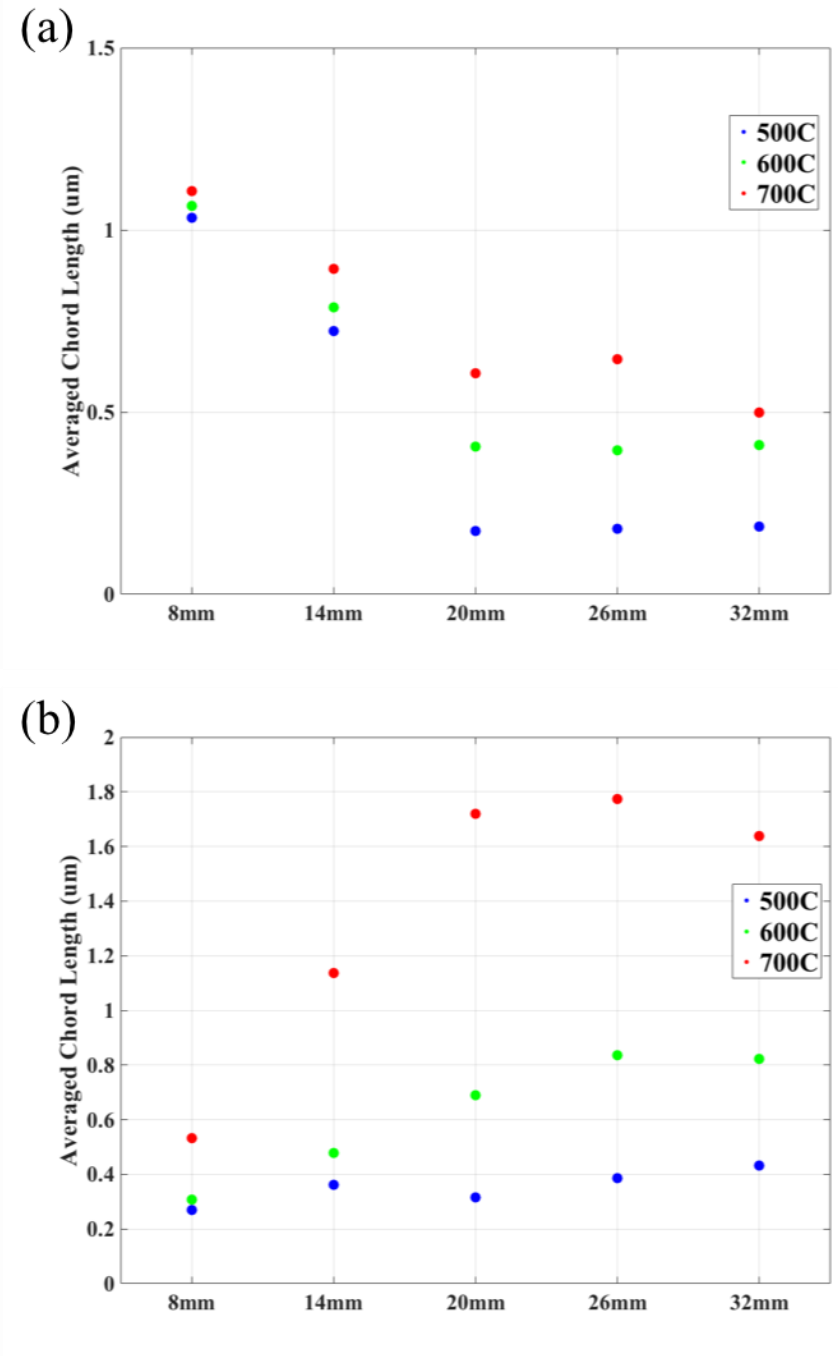

Figure 31 – (a) and (b) correspond to the averaged chord lengths of α-Ti phase and β-Ti phase. The five locations (8 mm, 14 mm, 20 mm, 26 mm, 32 mm) in the plot are consistent with the locations shown in Figure 22.

5.2.3.2 High Throughput Mechanical Characterization

Spherical indentation tests were performed at twenty-five grid locations for each of the five sample locations identified in Figure 22 for all three HT sample stripes. These were performed on an Agilent G200 with a continuous stiffness measurement (CSM). A spherical diamond tip with a nominal radius of 100 μm was used for all tests. An indenter tip radius of 100 μm produced a contact radius of about 7 microns at yield (contact area of roughly 150 sq. μm), and was hence able to capture the mechanical response of a region containing both phases. Tests are performed under a constant strain rate (loading rate over load) of 0.05/s and indented up to 800 nm in depth. CSM was set at an oscillation of 45 Hz and displacement amplitude of 2 nm. Figure 32 shows the elastic modulus, indentation yield strength and hardening parameters acquired for each location from all stripes.

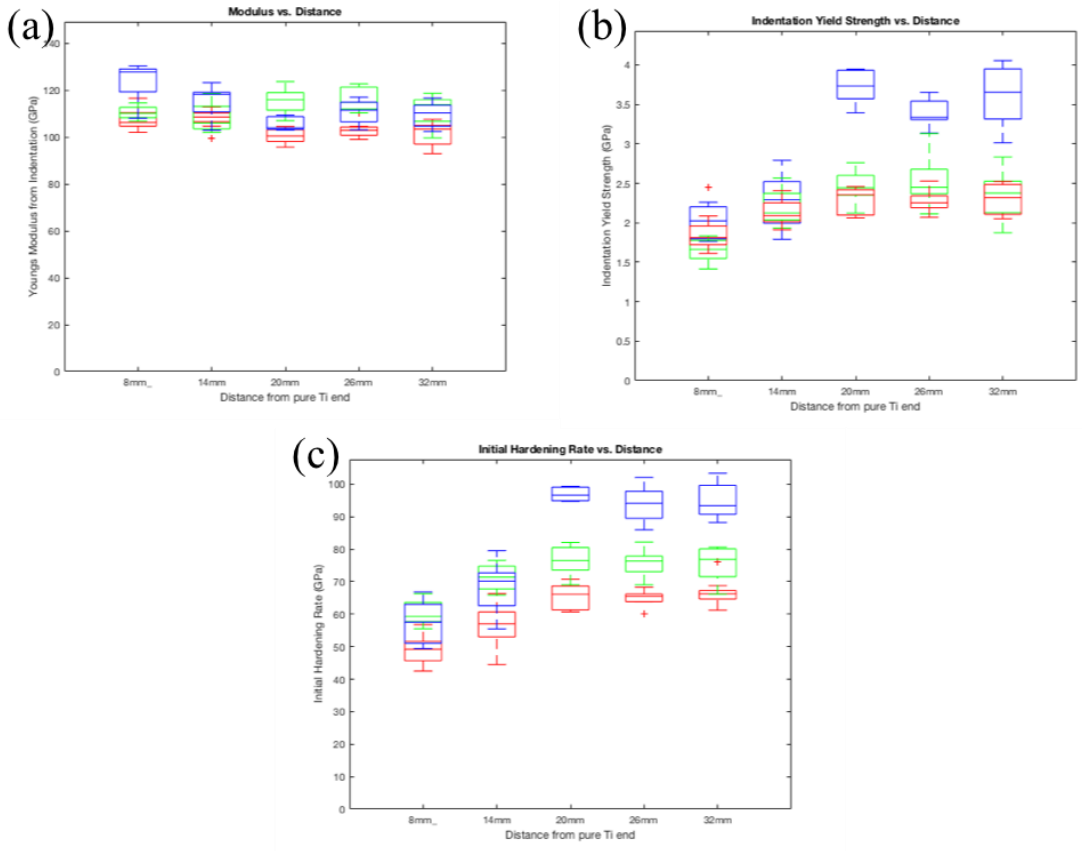

Figure 32 – Mechanical properties acquired from spherical indentation. (a) – (c) correspond to elastic modulus, indentation yield strength and indentation initial hardening rate. The blue, green and read boxes corresponds to 500 °C, 600 °C and 700 °C stripe, respectively. The five locations (8 mm, 14 mm, 20 mm, 26 mm, 32 mm) in the plot are consistent with the locations shown in Figure 22.

5.2.3.3 Process-Structure-Property Correlation

The idealizations and simplifications made in the first case study (see section 5.1.3.3) still hold. In the first case study, the volume fraction and feature length are chosen to serve as microstructure descriptor to establish further correlations. This empirical choice is made for the sake of their strong relevant with mechanical properties measured as well as their simplicity in calculation and physical explanation. However, in

this case study, as we introduced more variables from process space, the microstructure space gets more complicated. Simple descriptors like volume fraction and averaged chord length is no longer sophisticated enough to fulfil the tasks of building practically useful P-S-P linkages. Instead, entire spectrum of CLD from both α and β phases is used to quantify the microstructure. This descriptor, compared to previous ones, is believed to be more inclusive for microstructure representation, containing information from the size and shape of both phases and implicitly including the value of volume fraction and averaged feature length. In addition, CLDs acquired from each image are accounted separately in order to capture the variances in microstructure of each composition-temperature combinatory condition.

The quantification of microstructures using CLD produces a long vector (the magnitude of the pixel number of the longest chord) of descriptors for the microstructure. Principal component analyses (PCA) has been shown to be remarkably effective in arriving at objective (data-driven) low dimensional representations [48-51, 53-55, 93] of the microstructure (see mathematical description in section 4.2). For the present case study, PCA was performed on a total of 96 BSE scans from 15 unique composition-temperature combinatory conditions. The following analyses indicated that only two PC scores (see Figure 33) are adequate to capture over 80% of the variance between the different microstructures in this ensemble (i.e., all 96 scans included in the study). In other words, only two numbers (i.e., the first two PC scores denoted as PC1 and PC2) are adequate to distinguish each of the microstructures produced in this study. This is indeed a remarkable dimensionality reduction, and to the best of our knowledge, un- matched by any other existing framework for microstructure quantification.

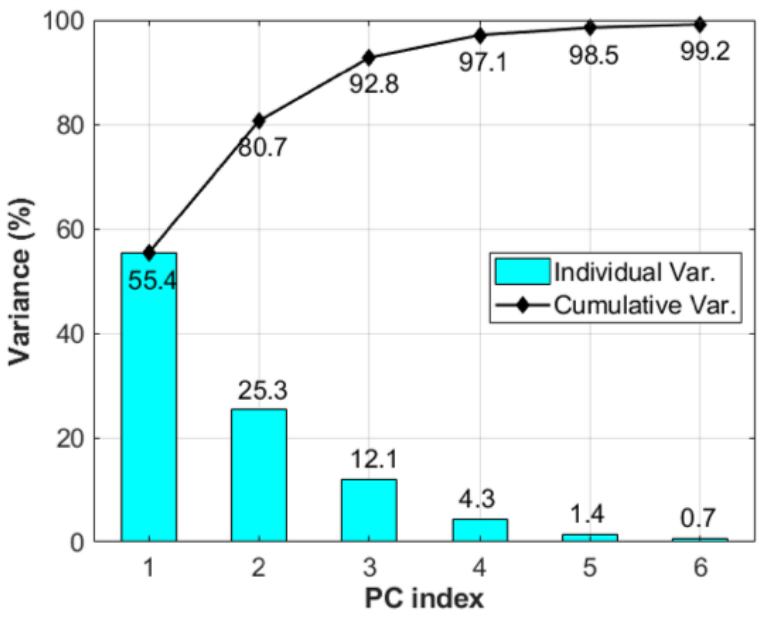

Figure 33 - The individual and cumulative variances from the PCA for the first 6 principal components shows that PC1 and PC2 carry 80.7% of the total variance in the dataset

Building on the low dimensional structure representation obtained (i.e., PC1 and PC2), we are now in a position to establish PSP linkages of interest. Considering the limited number of process conditions in this case study, in order to validate the robustness of the linkages built, we introduced the data splitting method in which the ensemble dataset is generally split into calibration and test subsets. In this case study, 19 scans from 3 sample stripes were separated as test dataset while the rest as training dataset.

For the present case study, the process parameters are taken as the composition of Mn (C), and the post build aging temperature (T). The desired process-structure linkages

are then established using Gaussian process regression (with squared exponential kernel) and cross-validation techniques [49]. There is no explicit function expression from GP models. The accuracy of these models is displayed in Figure 34, where each point corresponds to one combinatory processing condition (i.e., the average and calculated variance of all scans from each sample).

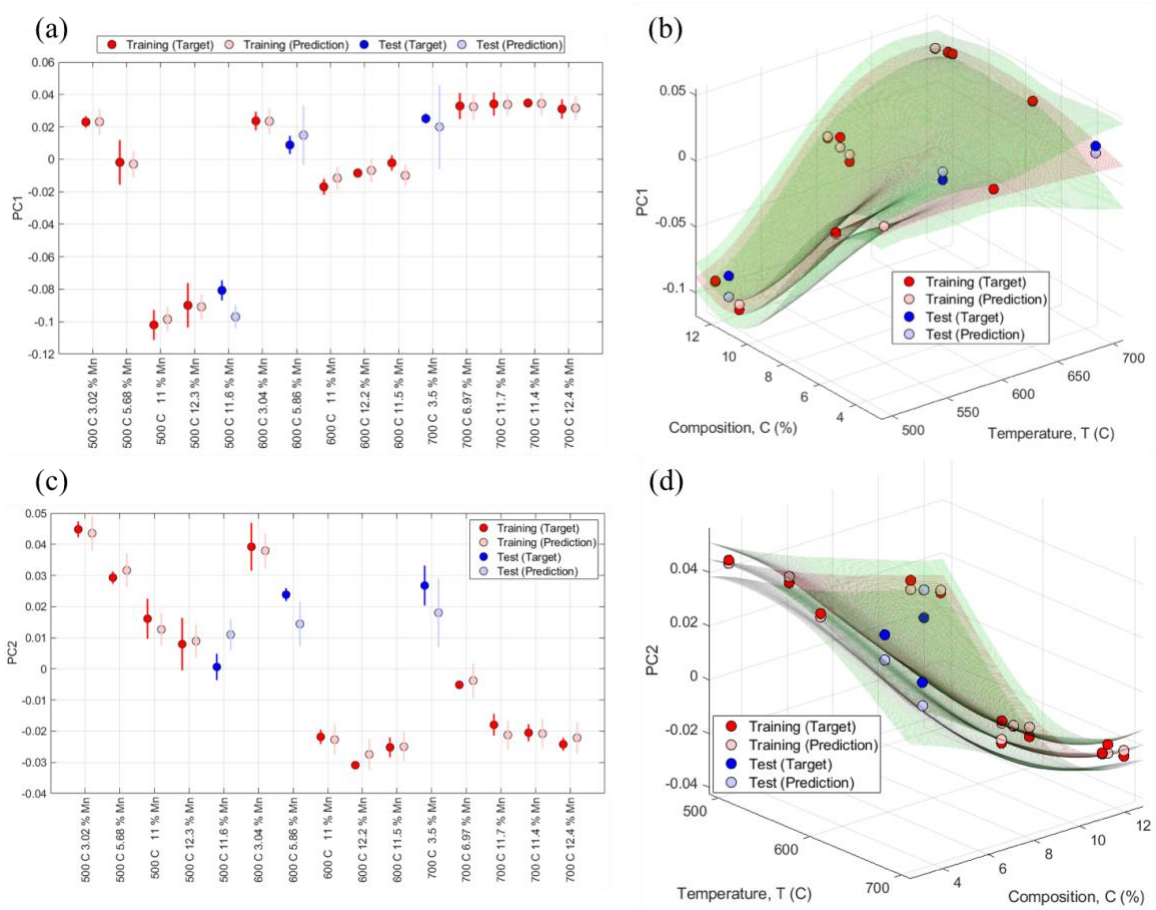

Figure 34 - The accuracy of process-structure linkages established in this work using data science approaches. The process variables included the Mn composition (C) and post build aging temperature (T). (a) and (b) illustrate the linkage for PC1, while (c) and (d) for PC2. (a) and (c) shows the comparison between targets (experimental data) and predictions for both training dataset and test dataset. (c) and (d) shows the prediction for the entire space with green surfaces indicating 1

sigma variance range and red surface indicating mean predications. In (a) - (d), each point is an ensemble average of CLD of all scans from one combinatory processing condition.

The approach described above can also be applied to establish a structure-property linkage. For the present case study, the recovered structure-property linkage is expressed as a model inputs PC1 and PC2 scores from microstructure and outputs indentation yield strength values. Again, with GP models, there is no explicit function expression. The accuracy of these models is displayed in Figure 35, where each point corresponds to one combinatory processing condition (i.e., the average and calculated variance of all scans from each sample).

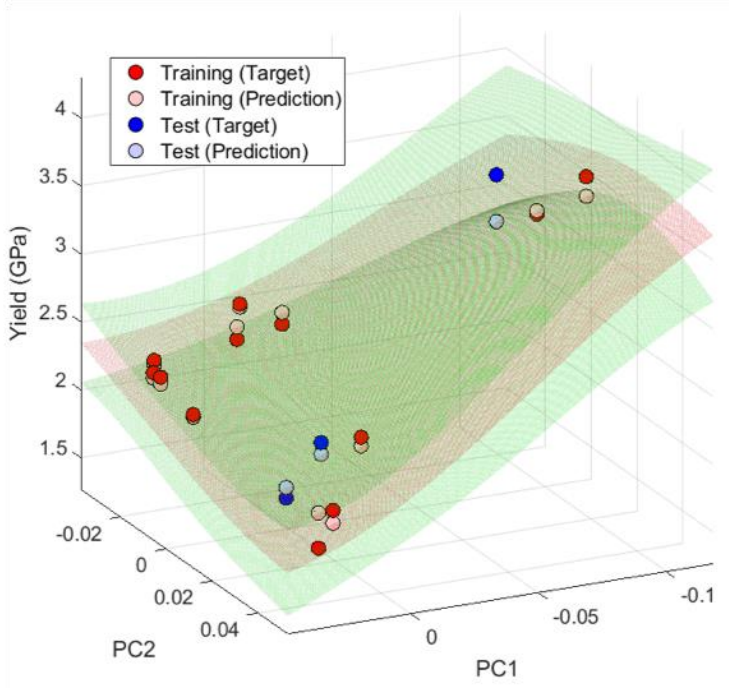

Figure 35 - The accuracy of structure-property linkages established in this work using data science approaches. It shows the comparison between targets (experimental data) and predictions for both training dataset and test dataset. The prediction for the entire space is illustrated with green surfaces indicating 1 sigma variance range and red surface indicating mean predications.

With the models built from process-structure linkages and structure-property linkage, one can eventually create a full P-S-P linkage (i.e., given certain process parameters (a combination of C and T), predicting property (indentation yield strength)). Indeed, starting from the processing conditions (both training set and test set) provided by experiment, we predicted the subsequent microstructure features in the form of PC scores. Then from the predicted PC scores, utilizing the model we acquired from Figure 35, we further give quantitative prediction on property of the materials (i.e., indentation yield strength of the alloys). The accuracy of such a P-S-P linkage is illustrated in Figure 36.

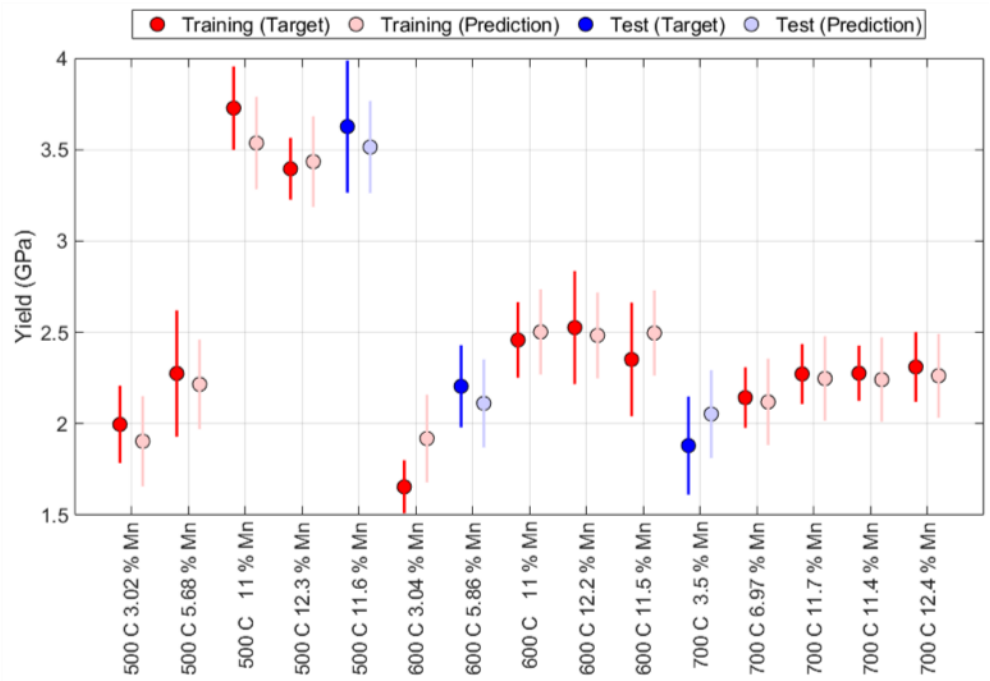

Figure 36 - The accuracy of process-structure-property linkages established in this work using data science approaches. It shows the comparison between targets (experimental data) and predictions for both training dataset and test dataset. The process variables included the Mn composition (C) and post build aging temperature (T).

The reader is reminded that the linkages developed here are data-driven. One of the implications is that the PSP linkages built here will change when new data is added. This is to be expected, especially since we used only 15 different processing conditions in this case study. When a substantial amount of data becomes available, we could expect the PSP linkages to become stable (i.e., there would be no need to change the PSP linkages with the addition of new data points). This indeed is one of the most attractive features of the protocols described here. They allow a coordinated effort by research

groups and/or investigators in ways that leverage all available data and minimize redundant effort in establishing such linkages. Furthermore, with the use of high throughput strategies, such as the indentation methods described in this paper, it is conceivable to aggregate PSP linkages of high value to the scientific community at dramatically accelerated pace compared to the conventional approaches used currently.

5.2.4 Discussion

As reasoned in the first case study, we believe the averaged values from the multiple indentations presented in Figure 32 could serve as good surrogate measures of the bulk properties that might be measured in standardized testing. However, it should be noted that the averaged indentation values do not capture any Hall-Petch effects [46] from the grain boundaries (note that these were not present in any of the indentations reported in this study). If grain size effects are significant (compared to the effects of the precipitate size and volume fraction) then one needs to conduct larger indentations that sample a few grain boundaries in the probed volumes.

Because of its dependence on interatomic bonding [85], the elastic modulus is expected to be impacted by the alloy composition, distribution of grain orientations [21, 86] and the phase volume fraction. The indentation moduli measured in this study did not show significant variations between the different locations on the HT sample, and fell in the range of 100-126 GPa. This range of values is quite reasonable, keeping in mind the values of the constituent phases (beta phase generally has a lower elastic modulus

compared to alpha phase in titanium alloys [94, 95]). If one were to use the rule of mixture, based on the volume fraction of the intermetallic phase, the predicted value of Young's moduli for the five locations would be exhibit a slight drop from lower to higher manganese end. It is indeed what has been observed in Figure 32. It is therefore clear that the moduli measured by indentation protocols described in this work are quite reasonable and reliable.

As seen in Figure 32, the indentation yield strengths increased systematically with the increase in Mn content. As expected, there is a strong positive correlation between the indentation yield strength and the volume fraction of the β phase (see Figure 28). Several strengthening mechanisms including solid solution strengthening, strengthening due to secondary phase, and grain boundary strengthening are likely to contribute to the observed increase in indentation strength with the increase in Mn content. In terms of solid solution strengthening in the matrix, the presence of Mn in pure Ti is expected to increase yield strength. Furthermore, we should also expect a contribution from phase strengthening due to the β phase.

It should be noted that our measurements (see Figure 31) indicated a strong negative correlation between the indentation yield strength and the averaged chord length of the α phase. This generally follows the well-known Hall-Petch relations [46] and I expected largely due to the dominance of α phase in location 1 and 2 and the drastic decrease of averaged chord length of α phase compared to the smoother increase of averaged chord length of β phase (note the steeper increase of averaged chord length of β

phase in 700 °C results in much less increase of yield strength and initial hardening rate). In addition, with similar Mn content, the indentation yield strengths increased as the aging temperature becomes lower. This can also be explained by the more dispersed and smaller β phase (see Figure 25) at lower aging temperature stripes. Such microstructure feature promotes more interfaces between α and β phases (especially in the 500 °C stripe) which serve as a major hinder for dislocation movement, and further strengthening the alloy.

A high throughput approach to explore mechanical properties of AM alloys with both different material chemistries and different post build aging temperatures has been presented and demonstrated on Ti-Mn alloy systems by LENS process. The spherical indentation along with various other characterization methods provides valuable microstructure and mechanical properties information of AM Ti-Mn alloys. The dataset generated was further successfully extracted and utilized to build low dimensional and practically useful data-driven P-S-P linkages. Hence, the combined approach of using AM processes and spherical indentation shows tremendous potential for high throughput alloy development of hierarchical materials for AM processes.

CHAPTER 6. EXPLORATION OF TI64 FOR ELECTRON BEAM MELTING

In this chapter, we will be focusing on another AM technique – electron beam melting (EBM) process. It is a typical powder bed fusion (PBF) technique in AM of metallic components (see Figure 37), in which successive layers of material powder are deposited onto a substrate plate from a powder reservoir (i.e., the powder hopper in Figure 37) via electron power source. As a symbolic characteristic, EBM builds components in layer-by-layer fashion, guided from certain CAD data. While many direct energy deposition processes are applicable to a wide range of materials including ceramics, polymers and metals, EBM can only work with metallic material systems because of the requirement of electrical conductivity. On the other hand, the vacuum condition of the build chamber, high environment temperature and the pre-heated substrate plate makes EBM preferable for high performance structural alloys [96]. While there are advantages to EBM, the problem choosing the appropriate processing parameters (beam power, beam velocity, pre-heating temperature, build geometry, scanning length and how the build is layout on the plate) in the huge and highly complicated processing space remains challenging in the field as processing conditions directly determine the part density, composition, microstructure and properties. Some of the processing effects on the AM titanium microstructure and mechanical behavior was discussed in Chapter 2.

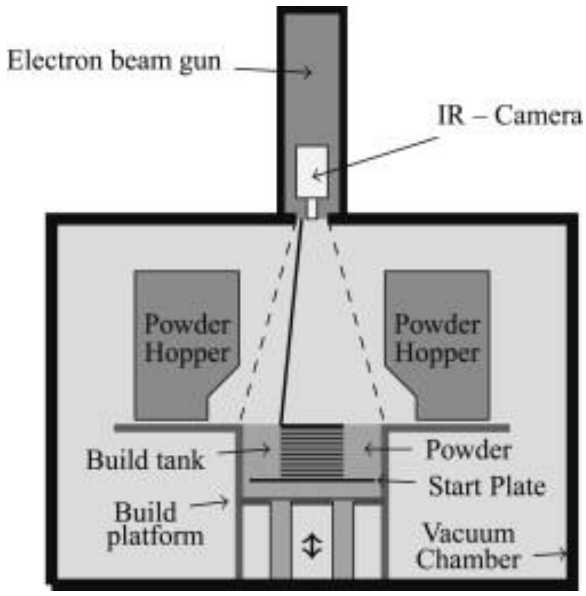

Figure 37 – Schematic of electron beam melting (EBM) process [97].

Ti-6Al-4V (referred as Ti64 in the following sections) has been chosen to be the subject of this case study owing to its wide commercial application and abundant previous studies. Indeed, by early 2000s, over 50 % of the titanium alloy market [98] in the USA is covered by Ti64 whereas all other types of $\alpha+\beta$ titanium alloys together sum up only to 14%. Specifically, because of the requirements for high strength and high fatigue resistance, the Ti-6Al-4V alloy is widely used in aerospace and drilling areas. As mentioned in the last chapter, these fields which are less sensitive to costs allow possible advancement of yet expensive AM techniques.

6.1 Inherent Thermal History Effect on AM Ti64 Components

The case study in this chapter will be investigating inherent thermal history induced heterogeneous characteristics in the Ti64 component manufactured by EBM process. In this manufacturing process, the thermal gradient accompanied directly affects the cooling rate of the melted powder, hence the resulting microstructure and the mechanical properties. Owing to the geometry (different positions) and the layer-by-layer (components often go through a series of heating and cooling cycles [17]) deposition of EBM, different build heights of the same component bear different thermal histories which lead to different microstructure and the mechanical properties. The objective of this case study is to capture such within build variance and further investigate the microstructure and mechanical property relations in the EBM Ti64 block part. Protocols of high throughput characterization methods will be formulated and employed. The mechanical property results will be compared with conventional tensile testing results using the same sample block. The results of microstructure quantification in relation with mechanical response will be presented, analyzed and discussed.

6.1.1 Materials and Process

This section will introduce the materials and the specifics on the process of sample stripes. Because the specimen is manufactured by our collaborators from Professor Rollett group in CMU, most of the details in this section is provided by Professor Rollett.

The EBM Ti-6Al-4V materials of this study were built on an Arcam S12 machine at Carnegie Mellon University, using a virgin batch of standard pre-alloyed Arcam AB

Ti-6Al-4V (Grade 5) powder, with supplier reported typical chemical composition of 6 % Al, 4 % V, 0.03 % C, 0.1 % Fe, 0.15 % O, 0.01 % N, 0.003 % H and Ti to balance, and with nominal powder size distribution of 45 - 100 microns. It should be noted that these feedstock specifications are given by the supplier, and no additional chemical composition measurements are performed on the powder or the printed parts. Arcam beam speed function of 36 is chosen, which should result in a nominal melt pool area of 0.04-0.06 mm^2 [99]. Speed function is a standard build theme for Arcam, for which the beam parameters of power and velocity are controlled according to a manufacturer developed algorithm in order to fabricate fully dense parts with microstructural consistency, which makes the specific values of beam speed and beam current unknown throughout the build as the build theme varies them constantly. The built part is a block (see Figure 38) of size 150 mm x 65 mm x 60 mm for 60 mm is the build height, which is fabricated with the nominal hatch spacing, layer thickness and build plate temperature of 200 μm, 70 μm, and 750 ◦C respectively. The layout took total of 38 hours to build.

After the layout design, machine setup, building and part extraction steps, the front block was cut with electrical discharge machine (EDM) to extract horizontal tensile specimens of ASTM E8/E8M subsize specimen standard. The rest of the block was then sent to GT for HT characterization. EDM was chosen to eliminate the surface effects on properties. As the first few milimeters of the build are not yet leveled with proper powder spreading, the end part was only 56 mm tall.

The sample sent to GT was further sectioned (EDM) longitudinally forming a much smaller cuboid sample with reveals the center part of the original build block. This position is deliberately chosen in order to making meaningful comparison between HT

mechanical testing and conventional tensile testing, as most the mechanical response of the tensile bars will be located around the center of the specimen. The sectioned sample stripe was then prepared for metallography and indentation tests. The sample preparation involved a specific sequence of steps that proceed through grinding (P240, P1200 SiC paper) and then finished with polishing steps with decreasing abrasive particle size (9μm, 3μm, 1μm diamond suspension), with each step ensuring that the surface deformation introduced is removed in the next step. As mentioned previously, the surface quality is crucial for the spherical indentation we perform. However, owing to the probing size of this case study (which is 60 times larger in radius compared to previous case studies), the requirement for the surface quality is much relaxed. We thus opted for a final polishing step using vibro-mechanical polishing in solution mixing 5 parts of 0.06 μm colloidal silica suspension with 1 part of hydrogen peroxide.

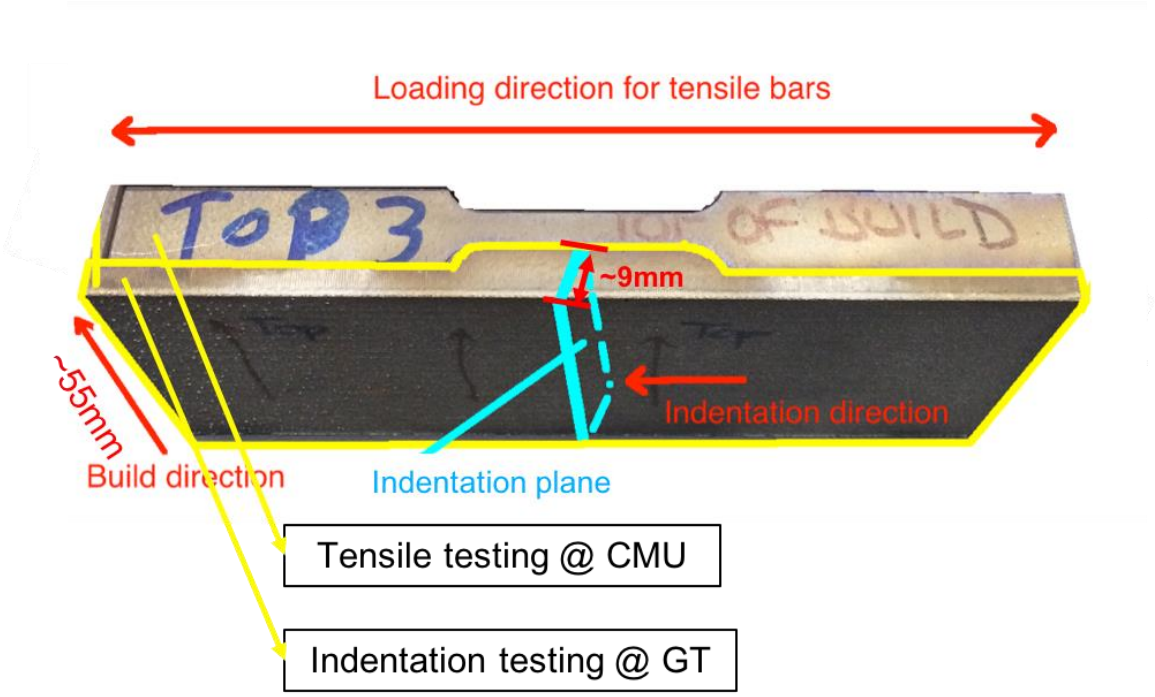

Figure 38 – Ti64 sample block produced by the EBM process for this study. The build direction, loading direction for tensile testing and indentation direction are illustrated. Note that 5 build heights are selected for testing – 2 mm, 14 mm, 26 mm, 38 mm, 50 mm from top of the block, respectively.

6.1.2 High Throughput Characterization Methods

From our collaborator in CMU, an MTS 880 machine was used to perform the room temperature uniaxial tensile tests, and the elongation was measured with an MTS dynamic extensometer of 1 inch length. The displacement speed was chosen as 0.004 mm/s, so that the strain rate at the reduced section of the tensile specimen would roughly be 0.0001 s−1.

Our focus in this case study is to acquire effective mechanical properties and salient microstructure features at different build heights of the same component build in order to capture the within build variance. Comparing to the previous case studies, in

order to capture effective bulk mechanical properties, the indentation performed in this case study should cover large enough area that contains multiple grains. Bear this in mind, indentation tip whose radius is 6.35 mm was chosen for the task, resulting the contact area to be around 400 um in radius which contains enough several α grains (shown in Figure 42). Five locations were chosen along the build direction for microstructure characterization and indentation tests. Since our scope of this case study is on how inherent thermal history effects properties at different build heights, the locations are intentionally picked to maximize the differences in possible thermal histories. In addition, we are also interested in quantifying and correlating the variabilities in both the microscopy and the indentation measurements. With this goal in mind, multiple measurements were performed at each of the five selected locations. More specifically, a series of 5 – 9 indentation tests were performed in lines range over 7 - 10 mm at all build heights. It was designed to represent properties from each heights while collect enough data to show the variance from each height. In comparison with the conventional assays (tensile testing), the HT assays, again, not only consume dramatically (88 times) less volume, but also cost significantly less time (26 times faster) and effort.

6.1.3 Results

6.1.3.1 High Throughput Mechanical Characterization

As mentioned previously, previous case studies working on indentation stress-strain curves has been focused on evaluating the plastic response at length scales that were significantly smaller than the grain size. Only recently, these protocols have been

extended to microindentation, where the length scales correspond to several grains (about 10 - 1000) in the indentation zone. For microindentations conducted in the present study, we utilized a customized Zwick-Roell Z2.5 hardness tester with a 6.35 mm radius tungsten-carbide spherical tip. A constant cross- head speed of 0.1 mm/min was utilized in all the tests reported here.

An example indentation stress-strain curve produced in this work is plotted in Figure 39 right, which corresponds to 2 mm, 38 mm and 50 mm location from top of the build. In this test, there were 20 unloading segments. The sample elastic modulus, Es, is estimated from the initial elastic loading segment. The indentation yield strength defined based on 0.2% offset on the indentation stress-strain curve using an indentation modulus. Indentation results from the multiple tests conducted in this work are summarized in Figure 39 and **Error! Reference source not found.**. The moduli of all the heights fall in t he range of 120 – 126 GPa. This range of values is quite reasonable, keeping in mind the values of the Young's moduli mentioned earlier studies. As seen in **Error! Reference s ource not found.**, the indentation yield strengths decreased systematically from top to bottom of the build. It should be emphasized that the results from tensile testing with either modulus or yield strength, are in great agreement with those from indentation. As mentioned previously, the indentation-to-tensile yield strength ratio value in this table is very typical for Ti alloys [38].

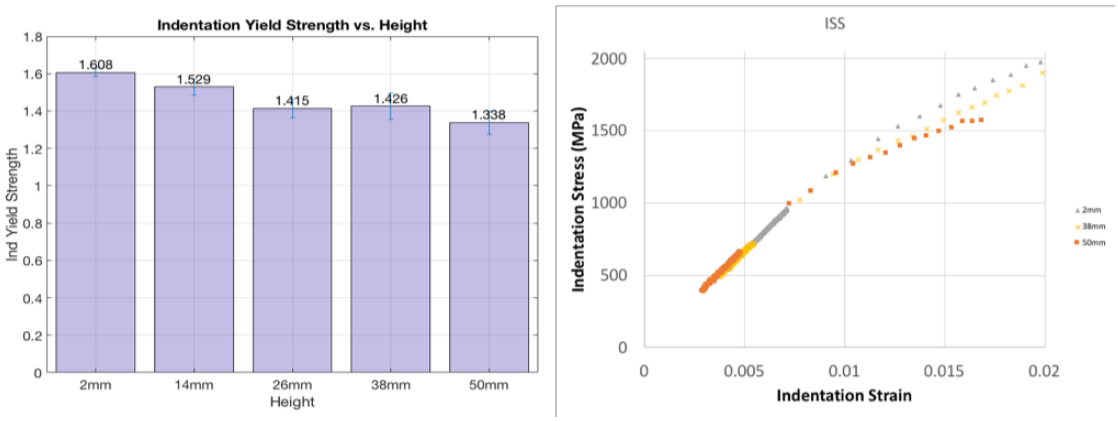

Figure 39 - Mechanical properties acquired from spherical indentation. Left illustrate the mean and variance values of indentation yield strength at different build heights. Right illustrate the example indentation stress strain (ISS) curves from 2 mm, 38 mm and 50 mm location shown in Figure 38.

Table 4 – Average measurements of mechanical properties from indentation and tensile testing at the five build heights in the Ti64 sample block.

Distance From Build Top	2mm	14mm	26mm	38mm	50mm
Young's Modulus from Indentation(GPa)	121.30	123.40	125.50	120.60	125.70
Young's Modulus from Tensile Tests (GPa)	119.06	113.75	114.85	115.38	111.40
Indentation Yield Strength (GPa)	1.61	1.53	1.42	1.43	1.34
Tensile Yield Strength	884	851	796	829	780
Indentation-To-Tensile Yield Strength Ratio	1.83	1.80	1.78	1.72	1.72

6.1.3.2 Microstructure Characterization and Structure-Property Correlation

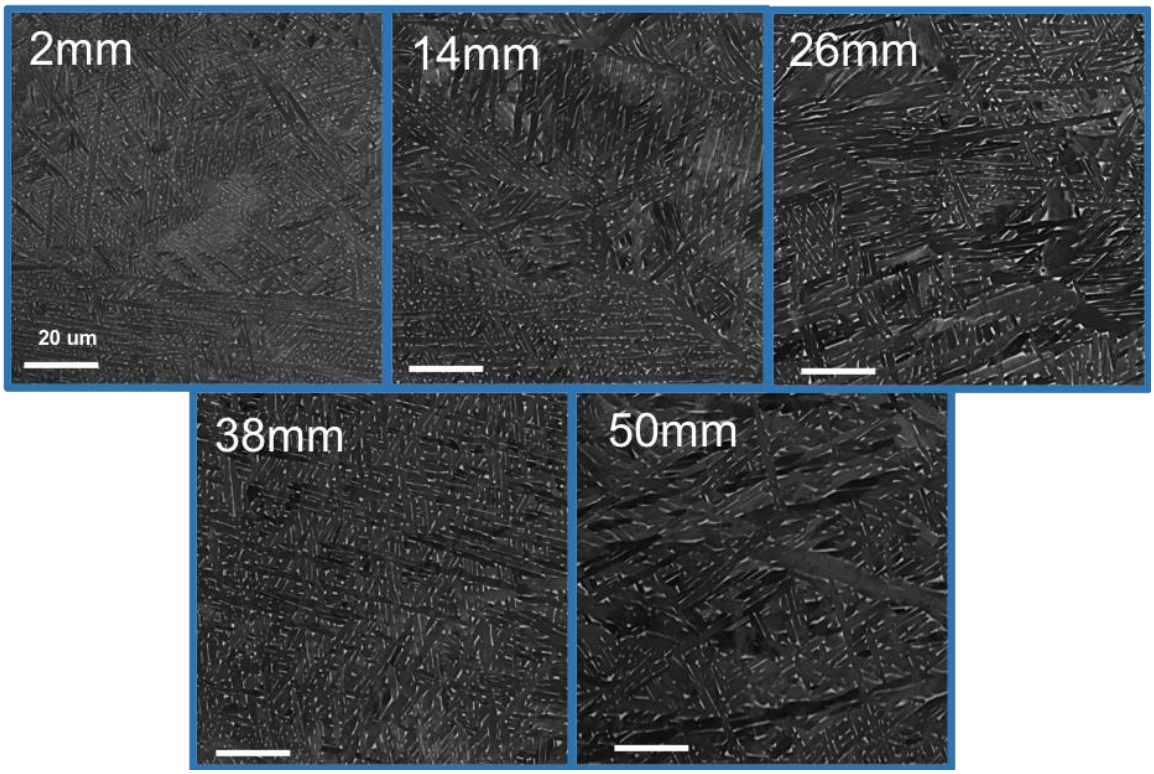

Figure 40 - SEM Backscattered electron (BSE) images corresponding to locations 2 mm – 50 mm from top build. The darker phase in the figures is α-Ti, while the brighter phase is the β-Ti.

With identical methods and settings as previous studies, multiple BSE images were captured for all five different heights. Examples of such images are shown in Figure 40. Similar to the last case study, in these micrograph, two distinct phases are visible as the brighter and darker components which correspond to α and β Ti phase. Because the subtle between-class (as between different build heights) variance nature of this study. Besides the lower amount of β shown in 2 mm height, the between-class differences of the secondary phase in size, shape and volume fraction are very hard for qualitative evaluation. Thus, image segmentation mentioned previously is introduced to calculate the

volume fractions of β-Ti over all heights. The results can be seen in Figure 41 where, the β phase volume fractions systematically drops from top to bottom build. This strong correlation with yield strength acquired in the last section were quantified using the Pearson product-moment correlation coefficient [83] in **Error! Reference source not found.**. This coefficient measures the linear dependence between two variables in the range [-1,1], where positive (negative) value indicates positive (negative) correlation. A larger absolute value implies that the relationship is more likely to be described by a linear equation – in this case between volume fraction of β and yield strength.

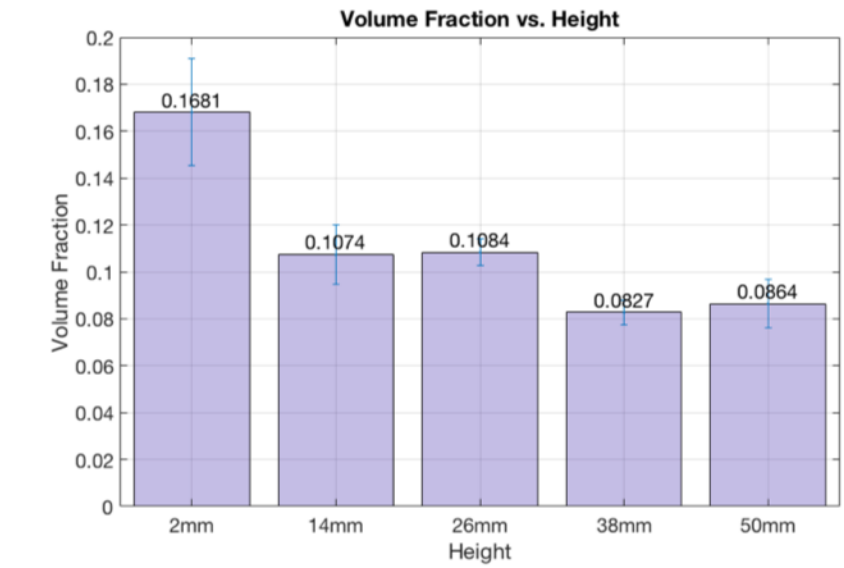

Figure 41 - β phase volume fraction corresponding to 5 heights.

Table 5 - Pearson product-moment coefficient between different property measures obtained on the sample block and volume fraction of β-Ti phase.

Pearson product moment correlation	Young's Modulus from Indentation	Indentation Yield Strength
Volume Fraction	-0.322	0.850

More effort was made on the microstructure quantification side in hopes of capturing meaningful correlation with mechanical properties. Besides acquiring phase morphology information using scanning election microscopy (SEM), electron back-scattered diffraction (EBSD) [100-104] was also used in this case study. Lattice orientations of both α and β titanium phases were carefully obtained and analyzed through inversed pole figures (IPF) in Figure 42. It shows, comparing to the size of β phase, α-Ti is dominant in the microstructure. Using such maps, at least two folds of information can be extracted - the grain morphology of the dominant phase (α-Ti) as well as its texture.

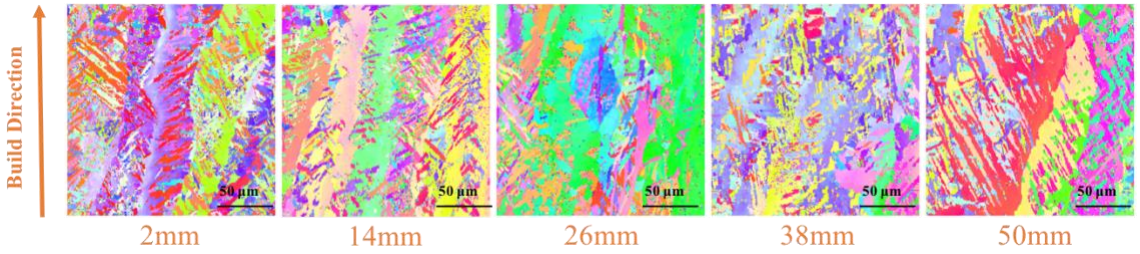

Figure 42 – An IPF map of AM Ti64 using EBSD. α phase size ranges from 50 – 120 um, while β phase size is few microns.

Utilizing the pipeline established in the last case study, angularly resolved chord length distribution (CLD) was introduce to collect feature length information of α phase from the EBSD maps. Note that at least 4 EBSD images were taken at each build height. For each scan, CLDs from 72 angles (evenly distributed within 360 degree) are collected and then averaged forming a singular distribution. The CLDs of all scans from the same build height were further combined to represent the distribution of the microstructure at each build height. The results are illustrated in Figure 43. A calculation of averaged chord length at all build heights (see **Error! Reference source not found.**) as well as PCA of t he CLD are also made. With the current dataset we acquired, it is very hard to see any meaningful correlation between the chord length of α phase and the mechanical properties.

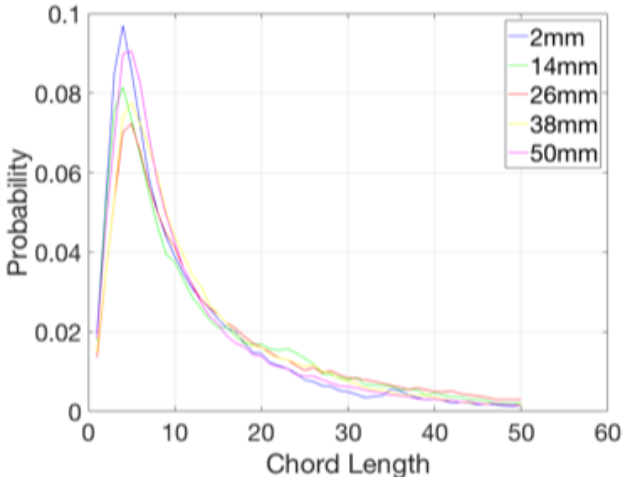

Figure 43 – Averaged chord length distribution (CLD) of α-Ti for all build heights from the sample block.

Table 6 – Averaged chord length of α-Ti for all build heights from the sample block.

Distance From Build Top	2mm	14mm	26mm	38mm	50mm
Average Chord Length (um)	5.81	6.29	7.18	6.81	6.01

In addition, since tests at each build height cover an area of 7 – 9 mm in one direction, if crystal orientation is a dominant factor to differentiate mechanical behavior at each build height, our indentation tests (contact radius ~200um at yield) should show comparable in-class (within each build height) variance and between-class (between build height) variance results. This is not the case in this project. So the texture information is not collected.

6.1.4 Summary

A high throughput approach to explore inherent thermal history influence on mechanical properties of AM Ti64 components has been presented and demonstrated by systematically investigating microstructure and mechanical properties at different heights of the build block. Phase, grain and orientation information was captured and analyzed to investigate the within build variance of AM Ti64 component, find the strong linear correlation between yield strength and volume fraction of β-Ti phase. The major element in this case study is the protocol of HT mechanical property characterization. In comparison with conventional tensile testing, spherical indentation renders mechanical properties which are equally reliable and avoids heavy sample and experiment preparation (i.e., making standard tensile specimen). This work provides a framework within which the investigation on heterogeneity of AM components becomes significantly more straightforward. Hence, the HT approach shows tremendous potential for accelerating alloy component development of hierarchical materials for AM processes.

CHAPTER 7. CONCLUSIONS AND FUTURE WORK

7.1 Conclusions

High throughput assays were established to explore materials space for additive manufacturing using combinatory sample libraries. With HT assays, rapid screening of material chemistry space and process space was performed building meaning links between microstructures and mechanical properties. Investigating inherent thermal history induced within build heterogeneity also becomes much more straightforward without heavy sample preparations. The versatility of the approach was demonstrated through case studies with different titanium alloys (Ti-Ni, Ti-Mn and Ti64) and different process parameters (composition, post build heat treatment and inherent thermal history). Unique datasets on LENS manufactured Ti-Ni, Ti-Mn systems as was as EBM manufacture Ti64 components were collected, which provideds enough data to extract practically useful S-P/P-S-P linkages use various modeling techniques.

7.2 Future Work

The modelling methods involved for building P-S-P linkages in this study are all data-driven. The recommended future work can be developing physics based models calibration using experimental data acquired through HT assays. Notice this study onely focuses on titanium alloy systems and on limited aspects of the process history. With the versatility of the HT framework, further work can be extending the HT assays to more types of complex materials systems and more process combinations. On the AM

processing side, due to the practicality of the HT assays, further development could include establishing a feedback loop in additive manufacturing provided necessary microstructure and mechanical property information to realized in-line control of the final product. This could promote a much needed high throughput protocol for collecting new materials knowledge in AM alloys .

REFERENCES

[1] P.C. Collins, C.V. Haden, I. Ghamarian, B.J. Hayes, T. Ales, G. Penso, V. Dixit, G. Harlow, Progress toward an integration of process-structure-property-performance models for "three-dimensional (3-D) printing" of titanium alloys, Jom 66 (2014) 1299-1309.

[2] D. Zagrebelnyy, M.J.M. Krane, Segregation Development in Multiple Melt Vacuum Arc Remelting, Metall Mater Trans B 40(3) (2009) 281-288.

[3] G. Lütjering, J. Williams, Titanium (Vol. 2), Berlin: Springer, 2003.

[4] W.E. Frazier, Metal Additive Manufacturing : A Review, 23 (2014) 1917-1928.

[5] M. Thöne, S. Leuders, A. Riemer, T. Tröster, H. Richard, Influence of heat-treatment on Selective Laser Melting products–eg Ti6Al4V, Solid freeform fabrication symposium SFF, Austin Texas, 2012.

[6] J. Chen, L. Xue, Microstructural characteristics of laser-clad AISI P20 tool steel, Proceedings of 1st international surface engineering congress and 13th IFHTSE congress. Materials Park (OH): ASM International, 2002, p. 198.

[7] G.R. Link, Layered manufacturing of laser-deposited carbon steels, 2000.

[8] M. Griffith, M. Schlienger, L. Harwell, Thermal behavior in the LENS process, Sandia National Labs., Albuquerque, NM (United States), 1998.

[9] J. Mazumder, J. Choi, K. Nagarathnam, J. Koch, D. Hetzner, The direct metal deposition of H13 tool steel for 3-D components, Jom 49(5) (1997) 55-60.

[10] H. El Kadiri, L. Wang, M.F. Horstemeyer, R.S. Yassar, J.T. Berry, S. Felicelli, P.T. Wang, Phase transformations in low-alloy steel laser deposits, Materials Science and Engineering: A 494(1-2) (2008) 10-20.

[11] L. Wang, S. Felicelli, Process modeling in laser deposition of multilayer SS410 steel, Journal of Manufacturing Science and Engineering 129(6) (2007) 1028-1034.

[12] B. Zheng, Y. Zhou, J. Smugeresky, J. Schoenung, E. Lavernia, Thermal behavior and microstructure evolution during laser deposition with laser-engineered net shaping: part II. Experimental investigation and discussion, Metallurgical and Materials Transactions A 39(9) (2008) 2237-2245.

[13] G. Dinda, A. Dasgupta, J. Mazumder, Laser aided direct metal deposition of Inconel 625 superalloy: Microstructural evolution and thermal stability, Materials Science and Engineering: A 509(1-2) (2009) 98-104.

[14] L. Costa, R. Vilar, T. Reti, A. Deus, Rapid tooling by laser powder deposition: process simulation using finite element analysis, Acta Materialia 53(14) (2005) 3987-3999.

[15] C. Selcuk, Laser metal deposition for powder metallurgy parts, Powder Metallurgy 54(2) (2011) 94-99.

[16] B. Baufeld, O. van der Biest, R. Gault, K. Ridgway, Manufacturing Ti-6Al-4V components by shaped metal deposition: microstructure and mechanical properties, IOP conference series: materials science and engineering, IOP Publishing, 2011, p. 012001.

[17] A. Saboori, D. Gallo, S. Biamino, P. Fino, M. Lombardi, An overview of additive manufacturing of titanium components by directed energy deposition: Microstructure and mechanical properties, Applied Sciences 7(9) (2017) 883.

[18] W.E. Frazier, Metal additive manufacturing: A review, Journal of Materials Engineering and Performance 23 (2014) 1917-1928.

[19] B. Salzbrenner, B. Boyce, B.H. Jared, J. Rodelas, J.R. Laing, Defect Characterization for Material Assurance in Metal Additive Manufacturing (FY15-0664), Sandia National Laboratories (SNL-NM), Albuquerque, NM (United States), 2016.

[20] S. Pathak, S.R. Kalidindi, Spherical nanoindentation stress–strain curves, Materials Science and Engineering: R: Reports 91 (2015) 1-36.

[21] J.S. Weaver, M.W. Priddy, D.L. McDowell, S.R. Kalidindi, On capturing the grain-scale elastic and plastic anisotropy of alpha-Ti with spherical nanoindentation and electron back-scattered diffraction, Acta Materialia 117 (2016) 23-34.

[22] S.R. Kalidindi, S. Pathak, Determination of the effective zero-point and the extraction of spherical nanoindentation stress-strain curves, Acta Materialia 56(14) (2008) 3523-3532.

[23] S. Pathak, D. Stojakovic, R. Doherty, S.R. Kalidindi, Importance of surface preparation on the nano-indentation stress-strain curves measured in metals, Journal of Materials Research 24 (2009) 1142-1155.

[24] S. Pathak, D. Stojakovic, S.R. Kalidindi, Measurement of the local mechanical properties in polycrystalline samples using spherical nanoindentation and orientation imaging microscopy, Acta Materialia 57(10) (2009) 3020-3028.

[25] S. Pathak, S.R. Kalidindi, N.A. Mara, Investigations of orientation and length scale effects on micromechanical responses in polycrystalline zirconium using spherical nanoindentation, SMM 113 (2015) 241-245.

[26] S.J. Vachhani, R.D. Doherty, S.R. Kalidindi, Effect of the continuous stiffness measurement on the mechanical properties extracted using spherical nanoindentation, Acta Materialia 61(10) (2013) 3744-3751.

[27] J.S. Weaver, Mechanical characterization of Ti-6Al-4V titanium alloy at multiple length scales using spherical indentation stress-strain measurements Authors: Jordan S. Weaver, 1-29.

[28] W.C. Oliver, G.M. Pharr, An Improved Technique for Determining Hardness and Elastic-Modulus Using Load and Displacement Sensing Indentation Experiments, Journal of Materials Research 7(6) (1992) 1564-1583.

[29] W.C. Oliver, G.M. Pharr, Measurement of hardness and elastic modulus by instrumented indentation: Advances in understanding and refinements to methodology, Journal of Materials Research 19(01) (2004) 3-20.

[30] G.M. Pharr, a. Bolshakov, Understanding nanoindentation unloading curves, Journal of Materials Research 17(10) (2002) 2660-2671.

[31] A. Khosravani, A. Cecen, S.R. Kalidindi, Development of high throughput assays for establishing process-structure-property linkages in multiphase polycrystalline metals: Application to dual-phase steels, Acta Materialia 123 (2017) 55-69.

[32] W.N. Sharpe, J. Bagdahn, K. Jackson, G. Coles, Tensile testing of MEMS materials - recent progress, J Mater Sci 38(20) (2003) 4075-4079.

[33] B. Wu, A. Heidelberg, J.J. Boland, Mechanical properties of ultrahigh-strength gold nanowires, Nature Materials 4(7) (2005) 525-529.

[34] C.P. Frick, B.G. Clark, S. Orso, A.S. Schneider, E. Arzt, Size effect on strength and strain hardening of small-scale [111] nickel compression pillars, Materials Science and Engineering a-Structural Materials Properties Microstructure and Processing 489(1-2) (2008) 319-329.

[35] Z.W. Shan, R.K. Mishra, S.A.S. Asif, O.L. Warren, A.M. Minor, Mechanical annealing and source-limited deformation in submicrometre-diameter Ni crystals, Nature Materials 7(2) (2008) 115-119.

[36] H. Bei, S. Shim, E.P. George, M.K. Miller, E.G. Herbert, G.M. Pharr, Compressive strengths of molybdenum alloy micro-pillars prepared using a new technique, Scripta Materialia 57(5) (2007) 397-400.

[37] D.K. Patel, S.R. Kalidindi, Correlation of spherical nanoindentation stress-strain curves to simple compression stress-strain curves for elastic-plastic isotropic materials using finite element models, Acta Materialia 112 (2016) 295-302.

[38] D.K. Patel, H.F. Al-Harbi, S.R. Kalidindi, Extracting single-crystal elastic constants from polycrystalline samples using spherical nanoindentation and orientation measurements, Acta Materialia 79 (2014) 108-116.

[39] K.L. Johnson, Contact Mechanics, P I Mech Eng J-J Eng 223(J3) (2009) 254-254.

[40] H. Hertz, Miscellaneous papers, Macmillan1896.

[41] X. Li, B. Bhushan, A review of nanoindentation continuous stiffness measurement technique and its applications, Materials Characterization 48(1) (2002) 11-36.

[42] J.S. Weaver, A. Khosravani, A. Castillo, S.R. Kalidindi, High throughput exploration of process- property linkages in Al-6061 using instrumented spherical microindentation and microstructurally graded samples, Integrating Materials and Manufacturing Innovation (2016) 1-20.

[43] J.S. Weaver, A. Khosravani, A. Castillo, S.R. Kalidindi, High throughput exploration of process-property linkages in Al-6061 using instrumented spherical microindentation and microstructurally graded samples, Integrating Materials and Manufacturing Innovation 5(1) (2016) 10.

[44] S. Pathak, S.R. Kalidindi, N.A. Mara, Investigations of orientation and length scale effects on micromechanical responses in polycrystalline zirconium using spherical nanoindentation, Scripta Materialia 113 (2016) 241-245.

[45] S.J. Vachhani, S.R. Kalidindi, Grain-scale measurement of slip resistances in aluminum polycrystals using spherical nanoindentation, Acta Materialia 90 (2015) 27-36.

[46] W.F. Smith, J. Hashemi, G.N. Cázares, P.A.G. Caver, L.C. Avilés, J.A.B. Velasco, Fundamentos de la ciencia e ingeniería de materiales, McGraw-Hill2006.

[47] D.M. Turner, S.R. Niezgoda, S.R. Kalidindi, Efficient computation of the angularly resolved chord length distributions and lineal path functions in large microstructure datasets, Modelling and Simulation in Materials Science and Engineering 24(7) (2016) 075002.

[48] S.R. Kalidindi, Hierarchical materials informatics: novel analytics for materials data, Elsevier2015.

[49] A. Gupta, A. Cecen, S. Goyal, A.K. Singh, S.R. Kalidindi, Structure–property linkages using a data science approach: Application to a non-metallic inclusion/steel composite system, Acta Materialia 91 (2015) 239-254.

[50] S.R. Niezgoda, Y.C. Yabansu, S.R. Kalidindi, Understanding and visualizing microstructure and microstructure variance as a stochastic process, Acta Materialia 59(16) (2011) 6387-6400.

[51] A. Choudhury, Y.C. Yabansu, S.R. Kalidindi, A. Dennstedt, Quantification and classification of microstructures in ternary eutectic alloys using 2-point spatial correlations and principal component analyses, Acta Materialia 110 (2016) 131-141.

[52] T. Fast, O. Wodo, B. Ganapathysubramanian, S.R. Kalidindi, G.W. Woodruff, Microstructure taxonomy based on spatial correlations: Application to microstructure coarsening, Acta Materialia 108 (2016) 176-185.

[53] A. Agrawal, P.D. Deshpande, A. Cecen, G.P. Basavarsu, A.N. Choudhary, S.R. Kalidindi, Exploration of data science techniques to predict fatigue strength of steel from composition and processing parameters, Integrating Materials and Manufacturing Innovation 3(1) (2014) 8.

[54] A. Çeçen, T. Fast, E. Kumbur, S. Kalidindi, A data-driven approach to establishing microstructure–property relationships in porous transport layers of polymer electrolyte fuel cells, J Power Sources 245 (2014) 144-153.

[55] S.R. Niezgoda, A.K. Kanjarla, S.R. Kalidindi, Novel microstructure quantification framework for databasing, visualization, and analysis of microstructure data, Integrating Materials and Manufacturing Innovation 2(1) (2013) 3.

[56] Z. Fan, F. Liou, Numerical modeling of the additive manufacturing (AM) processes of titanium alloy, Titanium alloys–towards achieving enhanced properties for diversified applications (2012) 3-28.

[57] T.B. Massalski, Binary alloy phase diagrams, ASM international 3 (1992) 2874.

[58] X. Gong, S. Mohan, M. Mendoza, A. Gray, P. Collins, S. Kalidindi, High Throughput Assays for Additively Manufactured Ti-Ni Alloys Based on Compositional Gradients and Spherical Indentation, Integrating Materials and Manufacturing Innovation 6(3) (2017) 218-228.

[59] R. Banerjee, P.C. Collins, D. Bhattacharyya, S. Banerjee, H.L. Fraser, Microstructural evolution in laser deposited compositionally graded alpha/beta titanium-vanadium alloys, Acta Materialia 51(11) (2003) 3277-3292.

[60] J. Geng, I.C. Nlebedim, M.F. Besser, E. Simsek, R.T. Ott, Bulk Combinatorial Synthesis and High Throughput Characterization for Rapid Assessment of Magnetic Materials: Application of Laser Engineered Net Shaping (LENS (TM)), Jom 68(7) (2016) 1972-1977.

[61] P. Samimi, Y. Liu, I. Ghamarian, P.C. Collins, A novel tool to assess the influence of alloy composition on the oxidation behavior and concurrent oxygen-induced phase transformations for binary Ti-xMo alloys at 650 degrees C, Corros Sci 89 (2014) 295-306.

[62] M. Polanski, M. Kwiatkowska, I. Kunce, J. Bystrzycki, Combinatorial synthesis of alloy libraries with a progressive composition gradient using laser engineered net shaping (LENS): Hydrogen storage alloys, Int J Hydrogen Energ 38(27) (2013) 12159-12171.

[63] P. Samimi, Y. Liu, I. Ghamarian, D.A. Brice, P.C. Collins, A new combinatorial approach to assess the influence of alloy composition on the oxidation behavior and concurrent oxygen-induced phase transformations for binary Ti-xCr alloys at 650 degrees C, Corros Sci 97 (2015) 150-160.

[64] K.I. Schwendner, R. Banerjee, P.C. Collins, C.A. Brice, H.L. Fraser, Direct laser deposition of alloys from elemental powder blends, Scripta Materialia 45(10) (2001) 1123-1129.

[65] P.C. Collins, R. Banerjee, H.L. Fraser, The influence of the enthalpy of mixing during the laser deposition of complex titanium alloys using elemental blends, Scripta Materialia 48(10) (2003) 1445-1450.

[66] P.C. Collins, D.A. Brice, P. Samimi, I. Ghamarian, H.L. Fraser, Microstructural Control of Additively Manufactured Metallic Materials, Annu Rev Mater Res 46 (2016) 63-91.

[67] A.H. Baker, P.C. Collins, J.C. Williams, New Nomenclatures for Heat Treatments of Additively Manufactured Titanium Alloys, JOM (2017) 1-7.

[68] M.Y. Mendoza, P. Samimi, D.A. Brice, B.W. Martin, M.R. Rolchigo, R. LeSar, P.C. Collins, Microstructures and Grain Refinement of Additive-Manufactured Ti-xW Alloys, Metallurgical and Materials Transactions A (2017) 1-12.

[69] S. Mantri, T. Alam, D. Choudhuri, C. Yannetta, C. Mikler, P. Collins, R. Banerjee, The effect of boron on the grain size and texture in additively manufactured β-Ti alloys, J Mater Sci 1-12.

[70] M.R. Rolchigo, M.Y. Mendoza, P. Samimi, D.A. Brice, B. Martin, P.C. Collins, R. LeSar, Modeling of Ti-W Solidification Microstructures Under Additive Manufacturing Conditions, Metallurgical and Materials Transactions A (2017) 1-17.

[71] B. Dutta, F.H.S. Froes, Additive manufacturing of titanium alloys, Butterworth-Heinemann Limited2016.

[72] Titanium Alloy Direct Deposited Products 6Al - 4V Annealed, SAE International, 2011.

[73] J. Williams, R. Baggerly, N. Paton, Deformation behavior of HCP Ti-Al alloy single crystals, Metallurgical and Materials Transactions A 33(13) (2002) 837-850.

[74] J. Kwon, M.C. Brandes, P. Sudharshan Phani, A.P. Pilchak, Y.F. Gao, E.P. George, G.M. Pharr, M.J. Mills, Characterization of deformation anisotropies in an α-Ti alloy by nanoindentation and electron microscopy, Acta Materialia 61(13) (2013) 4743-4756.

[75] M.F. Savage, J. Tatalovich, M. Zupan, K.J. Hemker, M.J. Mills, Deformation mechanisms and microtensile behavior of single colony Ti-6242Si, Materials Science and Engineering a-Structural Materials Properties Microstructure and Processing 319 (2001) 398-403.

[76] M.F. Savage, J. Tatalovich, M.J. Mills, Anisotropy in the room-temperature deformation of alpha-beta colonies in titanium alloys: role of the alpha-beta interface, Philosophical Magazine 84(11) (2004) 1127-1154.

[77] T. Neeraj, M.F. Savage, J. Tatalovich, L. Kovarik, R.W. Hayes, M.J. Mills, Observation of tension-compression asymmetry in alpha and alpha/beta titanium alloys, Philosophical Magazine 85(2-3) (2005) 279-295.

[78] A Threshold Selection Method from Gray-Level Histograms, IEEE Transactions on Systems, Man, and Cybernetics 9(1) (1979) 62-66.

[79] M. Sezgin, B. Sankur, Survey over image thresholding techniques and quantitative performance evaluation, J Electron Imaging 13(1) (2004) 146-168.

[80] S. Torquato, B. Lu, Chord-Length Distribution Function for 2-Phase Random-Media, Phys Rev E 47(4) (1993) 2950-2953.

[81] B.L. Lu, S. Torquato, Lineal-Path Function for Random Heterogeneous Materials, Phys Rev A 45(2) (1992) 922-929.

[82] S.R. Kalidindi, S.R. Niezgoda, A.A. Salem, Microstructure Informatics Using Higher-Order Statistics and Efficient Data-Mining Protocols, Jom 63(4) (2011) 34-41.

[83] K. Pearson, Note on regression and inheritance in the case of two parents, Proceedings of the Royal Society of London 58 (1895) 240-242.

[84] D.K. Patel, S.R. Kalidindi, Estimating the slip resistance from spherical nanoindentation and orientation measurements in polycrystalline samples of cubic metals, International Journal of Plasticity 92 (2017) 19-30.

[85] G.E. Dieter, Mechanical_Metallurgy.pdf.

[86] C. Fizanne-Michel, M. Cornen, P. Castany, I. Peron, T. Gloriant, Determination of hardness and elastic modulus inverse pole figures of a polycrystalline commercially pure titanium by coupling nanoindentation and EBSD techniques, Materials Science and Engineering a-Structural Materials Properties Microstructure and Processing 613 (2014) 159-162.

[87] D. Toprek, J. Belosevic-Cavor, V. Koteski, Ab initio studies of the structural, elastic, electronic and thermal properties of NiTi2 intermetallic, J Phys Chem Solids 85 (2015) 197-205.

[88] P.E. Rivera-Diaz-del-Castillo, W. Xu, Heat treatment and composition optimization of nanoprecipitation hardened alloys, Materials and Manufacturing Processes 26(3) (2011) 375-381.

[89] G. Welsch, R. Boyer, E. Collings, Materials properties handbook: titanium alloys, ASM international1993.

[90] R.G. Stringfellow, D.M. Parks, A self-consistent model of isotropic viscoplastic behavior in multiphase materials, International journal of plasticity 7(6) (1991) 529-547.

[91] D.D. Gu, W. Meiners, K. Wissenbach, R. Poprawe, Laser additive manufacturing of metallic components: materials, processes and mechanisms, International Materials Reviews 57 (2012) 133-164.

[92] P.C. Collins, R. Banerjee, S. Banerjee, H.L. Fraser, Laser deposition of compositionally graded titanium-vanadium and titanium-molybdenum alloys, Materials Science and Engineering A 352 (2003) 118-128.

[93] T. Fast, O. Wodo, B. Ganapathysubramanian, S.R. Kalidindi, Microstructure taxonomy based on spatial correlations: Application to microstructure coarsening, Acta Materialia 108 (2016) 176-185.

[94] M.T. Mohammed, Z.A. Khan, A.N. Siddiquee, Beta titanium alloys: the lowest elastic modulus for biomedical applications: a review, Int. J. Chem. Mol. Nucl. Mater. Metall. Eng 8(8) (2014).

[95] P. Laheurte, F. Prima, A. Eberhardt, T. Gloriant, M. Wary, E. Patoor, Mechanical properties of low modulus β titanium alloys designed from the electronic approach, Journal of the Mechanical Behavior of Biomedical Materials 3(8) (2010) 565-573.

[96] C. Körner, Additive manufacturing of metallic components by selective electron beam melting — a review, International Materials Reviews 61(5) (2016) 361-377.

[97] R. Ammer, M. Markl, U. Ljungblad, C. Körner, U. Rüde, Simulating fast electron beam melting with a parallel thermal free surface lattice Boltzmann method, Computers & Mathematics with Applications 67(2) (2014) 318-330.

[98] D. Eylon, S. Seagle, Titanium'99: Science and Technology, St. Petersburg (2000) 866-875.

[99] S. Narra, R. Cunningham, D. Christiansen, J. Beuth, A.D. Rollett, Toward Enabling Spatial Control of Ti-6Al-4V Solidification Microstructure in the Electron Beam Melting Process, Solid Free. Fabr. Symp., Austin, 2015, pp. 626-635.

[100] C.C. Tasan, J.P. Hoefnagels, M. Diehl, D. Yan, F. Roters, D. Raabe, Strain localization and damage in dual phase steels investigated by coupled in-situ deformation experiments and crystal plasticity simulations, International Journal of Plasticity 63 (2014) 198-210.

[101] F. Zhang, A. Ruimi, P.C. Wo, D.P. Field, Morphology and distribution of martensite in dual phase (DP980) steel and its relation to the multiscale mechanical behavior, Materials Science and Engineering: A 659 (2016) 93-103.

[102] B. Hutchinson, L. Ryde, E. Lindh, K. Tagashira, Texture in hot rolled austenite and resulting transformation products, Materials Science and Engineering: A 257(1) (1998) 9-17.

[103] T. Waterschoot, L. Kestens, B. De Cooman, Hot rolling texture development in CMnCrSi dual-phase steels, Metallurgical and Materials Transactions A 33(4) (2002) 1091.

[104] S. Zaefferer, J. Ohlert, W. Bleck, A study of microstructure, transformation mechanisms and correlation between microstructure and mechanical properties of a low alloyed TRIP steel, Acta Materialia 52(9) (2004) 2765-2778.